SANDIA REPORT

SAND2012-9145
Unlimited Release
1. Printed October 2012

Multiscale Models of Nuclear Waste Reprocessing: From the Mesoscale to the Plant-Scale

Rekha Rao, Chris Brotherton, Stefan Domino, Lindsay Erickson, Anne Grillet, Lindsey Hughes, Carlos Jove-Colon, Jeremy Lechman, Michael Loewenberg, Harry Moffat, Martin Nemer, David Noble, Tim O'Hern, Christine Roberts, Scott Roberts, Bion Shelden, Greg Wagner, Nick Wyatt

Prepared by
Sandia National Laboratories
Albuquerque, New Mexico 87185 and Livermore, California 94550

Sandia National Laboratories is a multi-program laboratory managed and operated by Sandia Corporation, a wholly owned subsidiary of Lockheed Martin Corporation, for the U.S. Department of Energy's National Nuclear Security Administration under contract DE-AC04-94AL85000.

Issued by Sandia National Laboratories, operated for the United States Department of Energy by Sandia Corporation.

Available to DOE and DOE contractors from
U.S. Department of Energy
Office of Scientific and Technical Information
P.O. Box 62
Oak Ridge, TN 37831

Telephone: (865) 576-8401
Facsimile: (865) 576-5728
E-Mail: reports@adonis.osti.gov
Online ordering: http://www.osti.gov/bridge

Available to the public from
U.S. Department of Commerce
National Technical Information Service
5285 Port Royal Rd.
Springfield, VA 22161

Telephone: (800) 553-6847
Facsimile: (703) 605-6900
E-Mail: orders@ntis.fedworld.gov
Online order: http://www.ntis.gov/help/ordermethods.asp?loc=7-4-0#online

SAND2012-9145
Unlimited Release
Printed October 2012

Multiscale Models of Nuclear Waste Reprocessing: From the Mesoscale to the Plant-Scale

Rekha Rao[1], Chris Brotherton[3], Stefan Domino[4], Lindsay Erickson[5], Anne Grillet[2], Lindsey Hughes[2], Carlos Jove-Colon[6], Jeremy Lechman[7], Michael Loewenberg[8], Harry Moffat[7], Martin Nemer[2], David Noble[1], Tim O'Hern[2], Christine Roberts[2], Scott Roberts[1], Bion Shelden[2], Greg Wagner[5], Nick Wyatt[2]

[1]Thermal and Fluid Processes, MS0836
[2]Thermal/Fluid Experimental Science, MS0346
[3]Contraband Detection, MS0782
[4]Computational Thermal and Fluid Mechanics, MS0836
[6]Radiation Risk and Consequence Analysis, MS0779
[7]Nanoscale and Reactive Processing, MS0836
Sandia National Laboratories
P.O. Box 5800
Albuquerque, New Mexico 87185

[5]Thermal/Fluid Science and Engineering, MS9409
Sandia National Laboratories, California
P.O. Box 969
Livermore, California 94551-0969

[8]Chemical Engineering Department
Yale University
New Haven, CT 06520-8286

Abstract

Nuclear waste reprocessing and nonproliferation models are needed to support the renaissance in nuclear energy. This report summarizes an LDRD project to develop predictive capabilities to aid the next-generation nuclear fuel reprocessing, in SIERRA Mechanics, Sandia's high performance computing multiphysics code suite and Cantera, an open source software product for thermodynamics and kinetic modeling.

Much of the focus of the project has been to develop a moving conformal decomposition finite element method (CDFEM) method applicable to mass transport at the water/oil droplet interface that occurs in the turbulent emulsion of droplets within the contactor. Contactor-scale models were developed using SIERRA Mechanics turbulence modeling capability. Unit operations occur at the column-scale where many contactors are connected in series. Population balance models

were developed to investigate placements and coupling of contactors at this scale. Thermodynamics models of the separation were developed in Cantera to allow for the prediction of distribution coefficients for various concentrations of surfactant and acid. Droplet-scale modeling was conducted in a microfluidic device and for verification of the algorithm. Extensive validation and discovery experiments were performed at the droplet and contactor-scales for both fluid dynamics and mass transport.

Acknowledgments

The authors would like to thank our mission specialist Veena Tikare for helping us develop the project, our reprocessing material balance expert Ben Cipiti for explaining the details of the reprocessing plant., Roger Pawlowski and Rich Schiek helped with the idea of a scalable network model, but were unable to continue with the project, though were very helpful in the first year of the work. We believe this type of work should be continued at Sandia. Paul Galambos and John Pflug supported our microfluidic experiments. Reviewers Randy Schunk and Lisa Mondy provided helpful feedback. Randy Schunk also helped with our droplet-scale modeling in a moving reference frame. The Aria Product Owners past and present, Amalia Black, Sheldon Tieszen, and Kim Mish, have been invaluable for keeping the project going despite the many other directions of Sierra Mechanics. We would like to thank the “Enabling Predictive Simulations” investment area of the LDRD program for funding this work. We would like to express our gratitude to the LDRD office for the extension given for receiving the final report due to the illness of the PI.

Contents

Figures

Tables

Nomenclature

DOE	Department of Energy
SNL	Sandia National Laboratories
Δt^n	Time step for the time during the time step n. (s).
$n_{k,s}^{A,n}$	Number of moles of species *k* in phase A at the time step *n* for the interfacial control volume, s. units (kmol).
$n_{k,s}^{B,n}$	Number of moles of species *k* in phase B at the time step *n* for the interfacial control volume, s. units (kmol).
$u_s^{S,n}$	Interfacial Velocity (units m s-1)
$u_s^{A,n}$	Velocity of Phase A at the interface at time step *n* (m s^{-1}).
$u_s^{B,n}$	Velocity of Phase B at the interface at time step *n* (m s^{-1}).
$u_*^{A,n}$	mass averaged velocity of Phase A at the A*, the edge of A's * control volume. (units m s-1)
$u_*^{B,n}$	mass averaged velocity of Phase B at the B*, the edge of B's * control volume. (units m s-1)
$u_{BULK}^{A,n}$	mass averaged velocity of Phase A at the bulk conditions of phase A, which is defined as the edge of the boundary layer at time step *n* (m s^{-1}).
$u_{BULK}^{B,n}$	mass averaged velocity of Phase B at the bulk conditions of phase B, which is defined as the edge of the boundary layer. at time step *n* (m s^{-1}).
$X_{k,s}^{A,n}$	Mole fraction of species *k* in phase A at time step *n* at the interface between phases A and B.
$X_{k,s}^{B,n}$	Mole fraction of species k in phase B at time step *n* at the interface between phases A and B.

$c_{k,s}^{A,n}$	Molar Concentration of species *k* in phase A at time step *n* at the interface between phases A and B. (kmol m^{-3})
$c_{k,s}^{B,n}$	Molar Concentration of species *k* in phase B at time step *n* at the interface between phases A and B. (kmol m^{-3})
$Y_{k,s}^{A,n}$	Mass fraction of species k in phase A at time step n at the interface between phases A and B
$\bar{V}_s^{A,n}$	Molar volume phase A at time step *n* at the interface between phases A and B. (m3 $kmol^{-1}$)
T_s^A	Temperature of phase A at the interface *s* (Kelvin)
T_s^B	Temperature of phase B at the interface *s* (Kelvin)
$P_s^{A,n}$	Pressure of Phase A at the interface *s* at time step *n* (Pascal)
$P_s^{B,n}$	Pressure of Phase B at the interface *s* at time step *n* (Pascal)
$P_{BULK}^{A,n}$	Pressure of Phase A at bulk conditions at time step *n* (Pascal)
$P_{BULK}^{B,n}$	Pressure of Phase B at bulk conditions at time step *n* (Pascal)
ΔL_{BL}^A	Boundary layer thickness on the A side of the interface at time step *n* (m).
ΔL_{BL}^B	Boundary layer thickness on the B side of the interface at time step *n* (m).
$\boldsymbol{n}^A$	Normal vector to the interface s pointing out of the A phase and into the B phase.
ρ^A	Density of the A phase (kmol m^{-3}).
M_A	Molecular Weight of species A.
$S_{A,k}^S$	Source term for the production of species *k* in phase A due to the interfacial reaction occurring on interface S. (kmol m^{-2} s^{-1})
$\underline{\underline{\boldsymbol{T}}}^{A,S}$	Stress tensor for phase A at the interface S.

H	Curvature of the interface at the current position
σ	Surface tension of the interface
$\boldsymbol{j}_{*,k}^{A}$	Mass diffusive flux of species *k* in phase A relative to the mass averaged velocity, at the control volume boundary in phase A. (kg m-2 s-1)
$\boldsymbol{j}_{*,k}^{B}$	mass diffusive flux of species *k* in phase B relative to the mass averaged velocity, at the control volume boundary.
$\boldsymbol{J}_{*,k}^{A}$	Molar diffusive flux of species *k* in phase A relative to the mass averaged velocity, at the control volume boundary in phase A. (kmol m-2 s-1)
$\boldsymbol{J}_{*,k}^{B}$	Molar diffusive flux of species *k* in phase B relative to the mass averaged velocity, at the control volume boundary in phase B. (kmol m-2 s-1)

1 INTRODUCTION

1.1 Background for Nuclear Waste Reprocessing

Nuclear waste reprocessing and nonproliferation models are needed to support the renaissance in nuclear energy. Our aim is to develop predictive capabilities targeting the design and monitoring of a next-generation nuclear fuel cycle to enable economic large-scale reprocessing with accurate material balances. Figure 1 shows an example of the front-end of a typical nuclear waste reprocessing based on wet chemical separation such as those in France at La Hague.

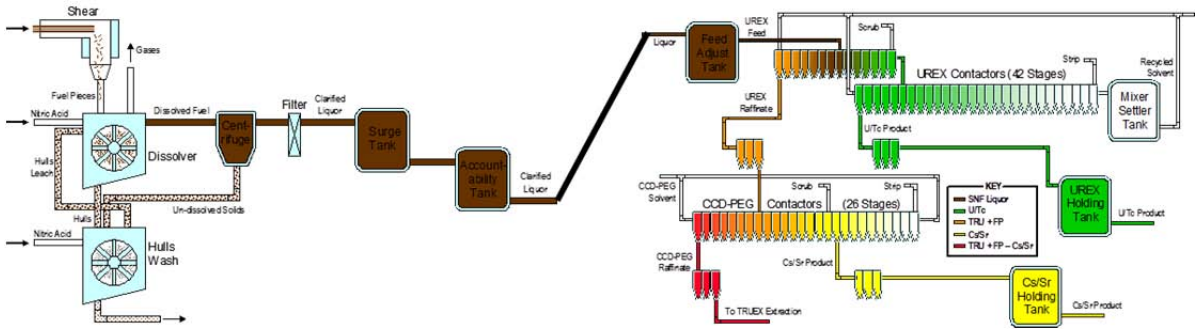

Figure 1. An example of the front-end of a nuclear waste reprocessing plant.

The spent fuel rod is 95% uranium, with the remaining constituents being daughter products that act to poison energy production in the nuclear reactor. If the spent fuel rod is reprocessed, *e.g.* separated from the fission products, the resulting material, a mix of uranium and plutonium, can be reused as nuclear fuel. The process begins by shearing the spent fuel rods to make them smaller and easier to dissolve in acid. Next these pieces are solubilized in acid as shown in Figure 2.

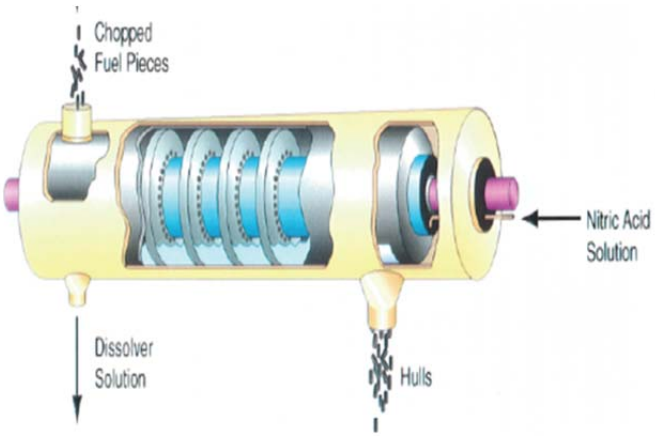

Figure 2. Spent fuel rods are dissolved in nitric acid solution to begin the separation process.

The heart of reprocessing is the PUREX process, where the acid solution from the dissolver, containing ions of uranium and plutonium oxide in solution, is mixed with organic phase (often dodecane mixed with tributyl phosphate (TBP), a surfactant that increases the selectivity of the separation) in a centrifugal contactor (Figure 3 shows the contactor experiment developed for this project). Production-scale contactors must be small (8cm diameter), and contact-times short, to address criticality issues for the radioactive materials. In order to achieve the desired separation, many contactors are connected in series with the product of one contactor being funneled to the next in line. In the example above, 42 contactors are connected to create the separation.

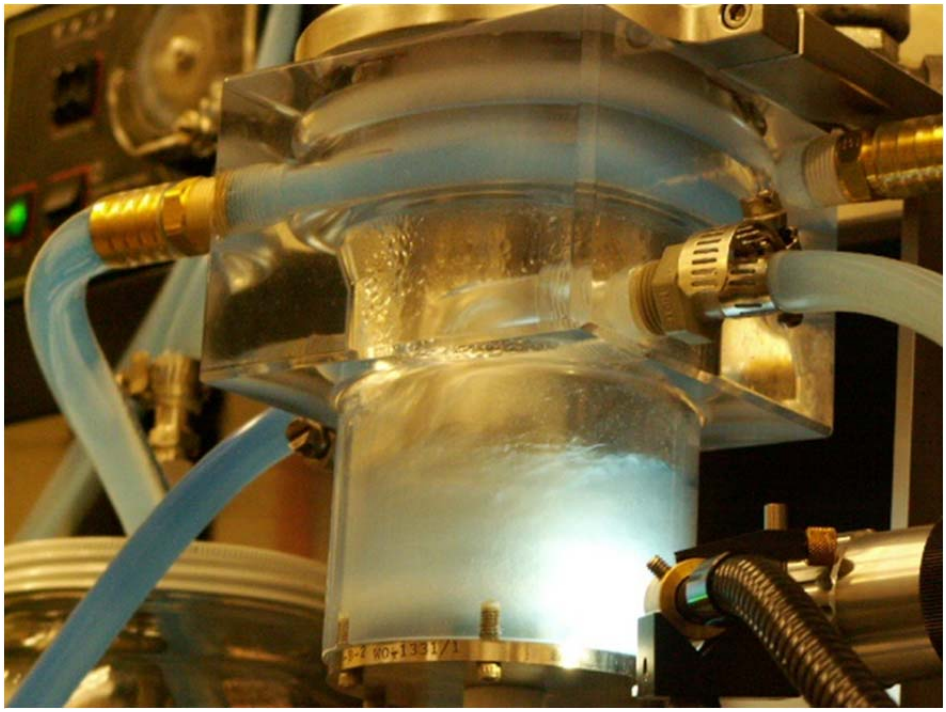

Figure 3. An example of an annular centrifugal contactor with organic and aqueous feeds. Here an acrylic housing is used to help visualize the free surface and the dispersed droplets and bubbles. A gas phase is always present in the contactor as the inflow and spin-rate of the rotor, sets the outflow.

In Figure 3, we can see that a head space filled with gas is always present during normal operation since the inflow rates and spin-rate of the rotor, set the outflow rate. Thus, two dispersed phases exist in the contactor: gas bubbles and emulsion droplets. If we blow up the image in Figure 3, we can see the two dispersed phases (Figure 4).

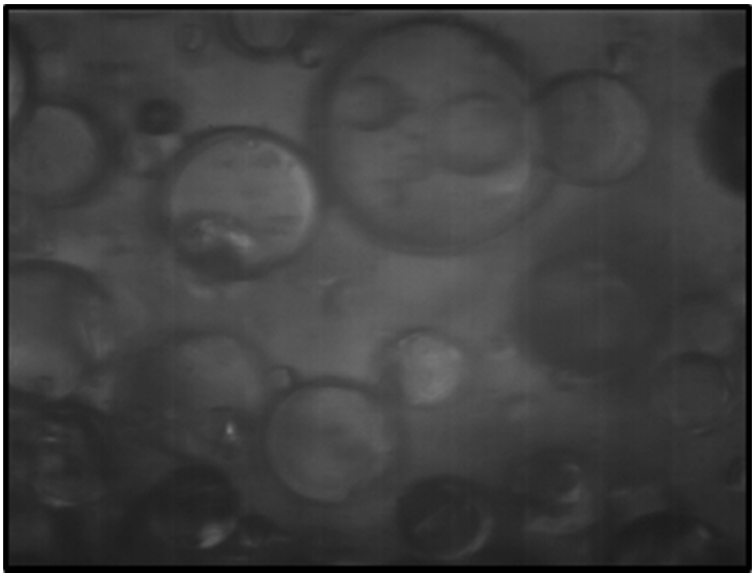

Figure 4. Blow-up of liquid region in the centrifugal contactor shows air bubbles and liquid droplets, which are hard to distinguish. The mass transport occurs at the interface between the droplet and the continuous phase.

The separation occurs when the uranium and plutonium ions moves from the acid phase to the organic phase. Mass transport occurs at the interface between the droplet and the continuous phase. Thus, understanding droplet-scale mass transport is fundamental to predicting contactor-scale mass transport.

The goal of this project was to develop a uranium separation model in SIERRA Mechanics, Sandia's high performance computing multiphysics code suite and Cantera, an open source software product for thermodynamics and kinetic modeling. Originally we sought to develop modeling capabilities from the plant-scale to the droplet-scale. Unfortunately, our work to develop models at the plant-scale leveraged a DOE Advanced Scientific Computing Research (ASCR) project to develop a novel, scalable network models to be used to create processing plant "flow sheets." When the lead for this project was reassigned to work at Oak Ridge National Laboratory on another project, we redirected our work to include more experiments at the droplet and contactor-scales and shifted the focus to modeling at these scales. Therefore, this work will be the focus of the report.

Much of the focus of the project has been to develop a moving conformal decomposition finite element method (CDFEM) method applicable to mass transport at the water/oil droplet interface that occurs in the turbulent emulsion of droplets within the contactor. Models are being developed contactor-scale using SIERRA Mechanics turbulence modeling capability with the classic level-set method. Unit operations occur at the column-scale where many contactors are connected in series. Population balance models were developed to investigate placements and coupling of contactors at this scale. Thermodynamics models of the uranium separation were developed in Cantera to allow for the prediction of distribution coefficients for variation concentrations of surfactant and acid.

1.2 Organization of Report and Research Highlights

The purpose of this report is to summarize the work from a three-year LDRD project. In this project, we have tried to focus on documenting our work through presentation, proceeding articles, journal articles and SAND reports. The project has produced thirteen presentations, seven seminars, two proceeding papers, and a SAND report. In addition, we have published two journal articles and one e-book chapter, have two more journal articles accepted for publication, and have submitted two other journal articles, and have four journal articles that are almost finalized. Thus, where possible we reference other documents instead of reproducing the work here. All other documents are either available from the open literature or from the PI, if the publication process is not yet complete. Some highlights from the project are shown in Figure 5.

The report is organized in the following manner. We begin by giving an overview of our numerical methods, namely CDFEM as implemented in SIERRA Mechanics. We discuss the theory and some of the verification efforts. In addition, to allow for turbulent flow modeling a hybrid CDFEM/Control Volume Finite Element Method (CVFEM) was developed and implemented in SIERRA. Laminar results from CDFEM are given at the droplet-scale including some preliminary mass transport work. Next, we summarize our microfluidic experiments to help elucidate mass transport and mixing phenomena at the droplet-scale and reference the two papers resulting from this effort. A contactor-scale model was developed for a single-phase material and is discussed in Chapter 5. Chapter 6 summarizes the centrifugal contactor experiments and references the paper produced from this work. Thermodynamic modeling is included as Chapter 7 including a summary of the results and references to the SAND report and journal article published on this work. Chapter 8 explains our population balance work to understand droplet-size evolution in the contactor, including mass transport, and references papers and presentations. In Chapter 9, we show how to put together individual contactors to make a column-scale model to predict mass transport at the unit-operations level. In Chapter 10, we summarize our accomplishments and discuss our plans for future work.

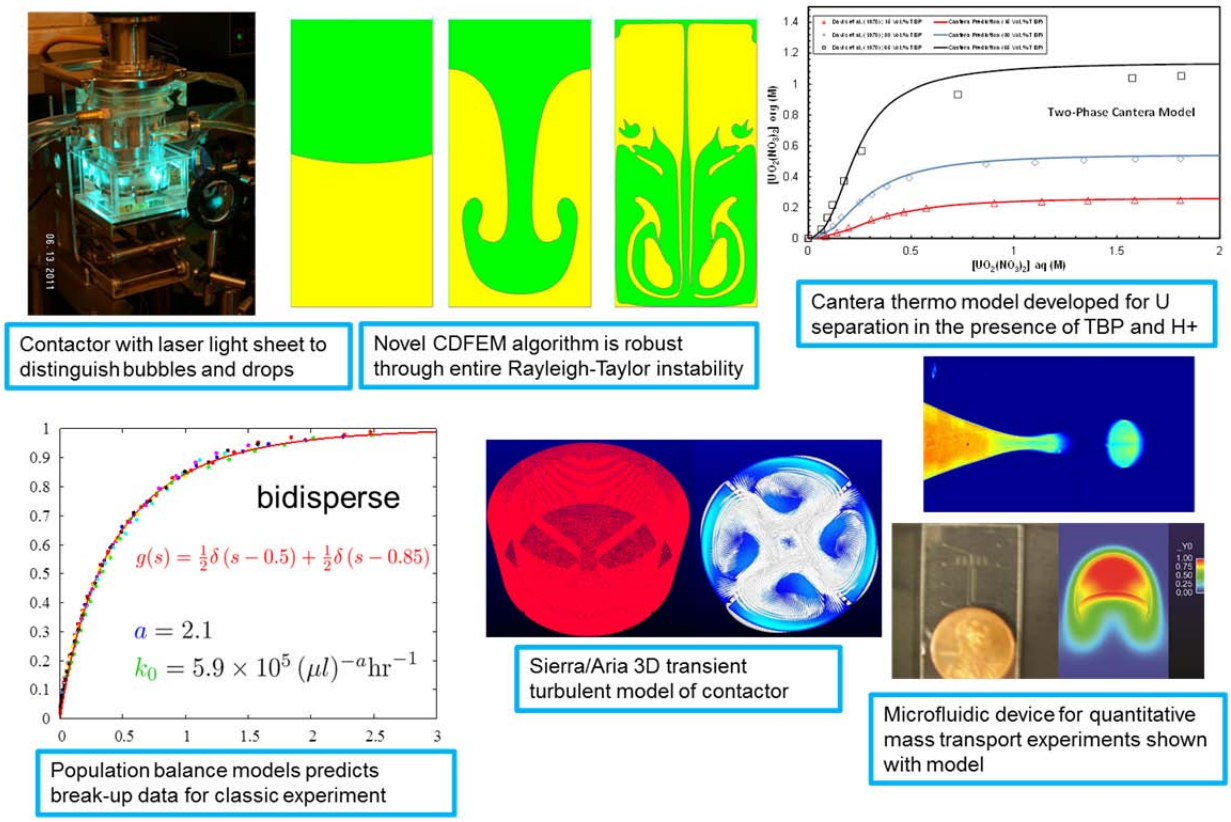

Figure 5. Selected Highlights from the project including experiments to understand droplet-scale and contactor-scale mass transport, new modeling capabilities for free-surface flows using CDFEM and thermodynamic modeling of PUREX in Cantera, and a new break-up kernel for population balance modeling.

2 NUMERICAL METHOD AND VERIFICATION PROBLEMS

In this section, we discuss the theoretical underpinnings of our numerical work and demonstrate verification of the algorithm. Much of this work will be published as a journal article targeted toward the Journal of Computational Physics [Noble et al., 2012]. The publication of this paper has been somewhat delayed by efforts to improve the algorithm, so multiple algorithms exist. For the focus of this chapter, we will concentrate on the unconstrained CDFEM algorithm, though constrained versions also exist and perform well.

2.1. Conformal Decomposition Finite Element Method

2.1.1 Introduction

The simulation of capillary hydrodynamics is challenging due to the combination of strong interfacial physics and moving interfaces with dynamic topology. The interfacial physics include the effects of surface tension as well as discontinuities in both density and viscosity. This physics can lead to a combination of strong and weak discontinuities in the pressure and velocity fields. Standard finite element shape functions cannot adequately capture these discontinuities. The moving interfaces with dynamic topology complicate simulations by requiring an approach that can describe this arbitrary interfacial motion. Interface tracking methods typically are not able to handle dynamic topologies.

In the finite element context, these requirements logically lead to the development of interface capturing methods with enriched finite element methods. Interface capturing methods, including volume of fluid (VOF) and level set (LS) methods, are able to describe the arbitrary topological evolution. Enriched finite elements are able to describe the interfacial physics and resulting discontinuities. In eXtended Finite Element Methods (XFEM), elements that span an interface are enriched with a combination of weakly and strongly discontinuous shape functions in order to describe the discontinuities. A study of XFEM for two-phase and free surface flows by Sauerland and Fries [Sauerland and Fries, 2011] contains a review of XFEM methods for this class of problems.

In this work, an alternate method of enrichment is employed. A background, non-conformal mesh is decomposed into elements that conform to the boundaries of the fluid domains, which are described in terms of one or more level set fields. Enrichment takes place by adding nodes where the edges of the background mesh intersect the level sets. The method is termed the conformal decomposition finite element method (CDFEM). By dynamically adding nodes and associated degrees of freedom on the moving interfaces, weak and strong discontinuities are described with standard finite element shape functions. See Figure 6 for a cartoon describing the algorithm.

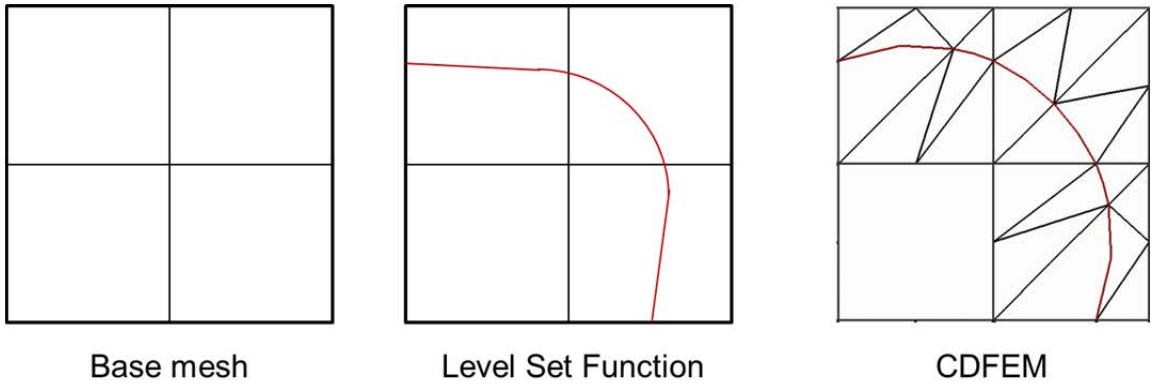

Figure 6. The CDFEM algorithm begins with a base mesh and then creates mesh on the interface location, as defined by the level set. As the interface moves, the old CDFEM mesh is deleted and new interface mesh is added. A meshed interface allows for easy application of discontinuities and interfacial physics.

The method is essentially a generalization of the finite element method using a Cartesian grid with added nodes (FEMCGAN) [Li, Lin, and Wu, 2003] to unstructured meshes of triangles and tetrahedra. The method is also closely related to the immersed-boundary finite element method [Ilinca and Hétu, 2011A, 2011B], but in that approach the added velocity degrees of freedom on the interfaces are eliminated using Dirichlet boundary conditions, and the pressure is discontinuous across faces and edges that are cut by the interfaces. A similar method is also developed by Li and Shopple [2011] for solidification and solvation applications. The method also shares some features with the fixed mesh arbitrary Lagrangian Eulerian (FM-ALE) method, which does not modify the mesh as the solution evolves, but instead projects the moving mesh solution back onto a fixed mesh [Codina et al., 2009].

In previous work, CDFEM was developed for stationary fluid interfaces [Noble, Newren, and Lechman, 2010]. A primary goal of that work was to quantify the accuracy of CDFEM. This is a concern because the level set surface cuts arbitrarily through the background mesh, and the quality of the resulting conformal elements may be quite poor. The accuracy of the method was quantified for multiple fluid problems using numerical examples. In all cases, optimal convergence rates for the piecewise linear elements were obtained both on the volumes and the surfaces containing the discontinuities. It was also argued that the discrete space introduced in CDFEM contains the space used in XFEM with Heaviside enrichment, since the XFEM space can be recovered by adding constraints on the nodes added in the conformal decomposition. According to Li et al., [Li, Lin, and Wu, 2003], this property guarantees that the CDFEM accuracy is no less than that afforded by XFEM with Heaviside enrichment. In this regard, CDFEM provides an alternative to XFEM, with the additional benefit of providing a layer of encapsulation separating all consideration of enrichment from the element assembly operations. The level set fields are used to decompose the mesh, thus enriching the finite element description. This decomposition produces a standard set of elements which are then assembled using standard finite element shape functions and quadrature. This is in contrast to XFEM where interpolation and quadrature must be significantly modified to accommodate the enrichment.

In the current work, a dynamic CDFEM method is developed for capillary hydrodynamics. Building on the static CDFEM work described previously, a dynamic CDFEM method is described and consideration is given to the time stepping method. Multiple enrichment schemes are explored in which the degrees of continuity in the level set, velocity, and pressure fields are varied. The method is verified by comparison against exact solutions and previous computational results in two and three dimensions.

2.1.2 Equations

2.1.2.1 Fluid Equations

Consider a computational domain, Ω, which consists of two immiscible fluids in Ω^+ and Ω^- separated by a moving interface Γ, with normal, **n** as shown in Figure 7.

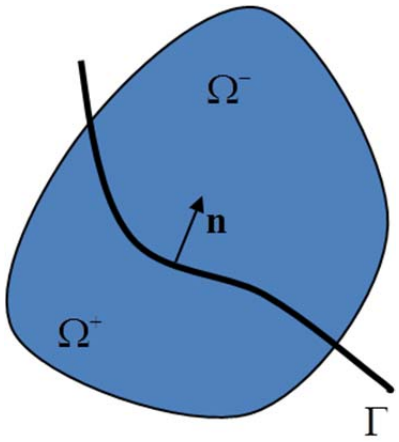

Figure 7. Computational domain, Ω, for two immiscible fluid Ω^+ and Ω^- separated by a moving interface Γ. The normal, n, is defined with respect to the interface.

The fluid velocity and pressure are described by the incompressible Navier-Stokes equations:

$$\rho \frac{\partial u}{\partial t} + \rho u \cdot \nabla u = \nabla \cdot \sigma + \rho g \tag{1}$$

$$\nabla \cdot u = 0 \tag{2}$$

with the stress tensor $\boldsymbol{\sigma}$ given by,

$$\sigma = -pI + \mu\left(\nabla u + \nabla u^t\right) \tag{3}$$

where μ is the Newtonian viscosity and **I** is the identity tensor. Along the interface Γ, the value of the velocity is continuous while surface tension produces a discontinuity in the stress:

$$[n \bullet \sigma] = \gamma \kappa n \ . \tag{4}$$

Here **n** is the surface normal, γ is the surface tension coefficient, κ is the curvature of the interface, and [*f*] defines the jump in *f* across the interface.

2.1.2.2 Level Set Equations

An interface capturing method, specifically a level set method, is used to describe the interface Γ. In this approach a scalar level set field is used to approximate the signed distance to the interfaces. That is, the magnitude is equal to the distance to the nearest point on the interface and the sign is dependent on which fluid the point lies within. The zero level set of the level set field, ϕ, represents the interface. This field is evolved via an advection equation:

$$\frac{\partial \phi}{\partial t} + u \bullet \nabla \phi = 0 \ . \tag{5}$$

This equation correctly evolves the zero level set, but does not preserve the signed-distance property. Consequently, the level set field must be periodically reinitialized. In this work, this is accomplished by recomputing the distance to the reconstructed interface that is developed as part of the conformal decomposition described below.

2.1.3 Conformal Decomposition

In CDFEM, enrichment takes place by decomposing the finite elements that span the zero level set into elements that conform to the original element as well as the zero level set surface or surfaces. In this work, the level set field is assumed to consist of a piecewise linear field on triangular or tetrahedral elements. Thus the interface consists of line segments in two-dimensions, and polygons in three-dimensions. The decomposition algorithms in both two and three dimensions, including degeneracy handling, are described in [Noble, Newren, and Lechman, 2010]. The result of the decomposition is a fully connected mesh of triangular elements in 2D or tetrahedral elements in 3D, which conform to the instantaneous locations of the immiscible fluids and their interfaces. For the dynamic case, mesh is both added and removed as the interface moves.

2.1.3.1 Dynamic Discretization via Interface Node Prolongation

The conformal decomposition process is much like the element refinement done in non-conformal adaptivity. The elements are subdivided into new elements and nodes are added in the process. Unlike non-conformal adaptivity, the new elements conform to the fluid domains, and the added nodes lie on the interfaces between the fluids. Just as in non-conformal adaptivity, the added nodes are populated with field data, or prolonged, based on existing field data.

Linear interpolation is commonly used in non-conformal adaptivity for prolongation. For fields that are C_1 continuous (continuous value and gradient), linear interpolation is a reasonable method for prolonging the field onto the added nodes. However, fields that contain weak or strong discontinuities across the interface (C_0 and C_{-1} fields, respectively) might require a different prolongation method that accounts for these discontinuities. Or, one of the other

methods described below may be more appropriate. In the extreme case, a field might be defined on only a subset of the fluids, and interpolation makes no sense since the field may be present on only a subset of the nodes of the element being decomposed. Also, due to the motion of the interfaces, some nodes will change material, or fluid, during the decomposition. Since, the nodes of the background, non-conformal mesh do not move during the conformal decomposition, these nodes change material as the interface passes over them. For C_1 fields, nothing needs to be done for these nodes, but otherwise the fields at such a node may need to be re-populated for the change in material.

2.1.3.2 Dynamic Discretization via Subdomain Integration

Another method for handling both new nodes and nodes that have changed material is to carefully form the assembly integrals and time derivatives in a way that conforms to the evolving subdomains. This is the approach recently taken in the context of XFEM [Fries and Zilian, 2009] and immersed boundary methods [Ilinca and Hetu, 2011B]. For example, using such an approach to assemble the Galerkin residual contribution for the time derivative for a scalar field, ψ, the integral over the entire domain is split into subdomains Ω^{++} (within Ω^{+} at both old and new time), Ω^{-+} (within Ω^{-} at old time and Ω^{+} at new time), Ω^{+-} (within Ω^{+} at old time and Ω^{-} at new time), and Ω^{--} (within Ω^{-} at both old and new time). This results in integration over 4 possible subdomains within elements:

$$\int_{\Omega} \frac{\partial \psi}{\partial t} w_i d\Omega = \int_{\Omega^{++}} \frac{\partial \psi}{\partial t} w_i d\Omega + \int_{\Omega^{-+}} \frac{\partial \psi}{\partial t} w_i d\Omega + \int_{\Omega^{+-}} \frac{\partial \psi}{\partial t} w_i d\Omega + \int_{\Omega^{--}} \frac{\partial \psi}{\partial t} w_i d\Omega \tag{6}$$

To evaluate this contribution the elements that span the interface must be decomposed into sub elements that conform to both the new and old locations of the interface. This method removes the need for prolongation by forming gradients and time derivatives using domain specific nodal values only at the times when the nodes lie within the given domain.

2.1.3.3 Dynamic Discretization via Moving Mesh

Fries and Zillian [2009] note that ALE methods also provide methods for handling time-dependent geometry and shape functions, employing an interface velocity in the formulation. However, they leave the idea of using such an approach for methods with dynamic enrichment as an open issue. A recent CDFEM work sought to expand on such an approach, and this is further developed here. One major advantage of this moving mesh approach is that the integration can be performed over subdomains that conform only to the new geometry.

In the moving mesh approach for handling the evolving discretization, the newly created nodes and nodes that have changed material are considered have moved to their current location from a previous location where all of the needed fields were already defined. The remaining nodes are taken to be stationary. The mesh motion is accounted for via a mesh velocity correction in the advection terms of the governing equations. For a moving node, the time derivative of a quantity, ψ, following the node can be expanded by the chain rule:

$$\frac{\partial \psi}{\partial t}\Big|_{\xi} = \frac{\partial \psi}{\partial t}\Big|_{x} + \frac{\partial x}{\partial t}\Big|_{\xi} \bullet \nabla_x \psi = \frac{\partial \psi}{\partial t}\Big|_{x} + \dot{x} \bullet \nabla_x \psi \tag{7}$$

Thus the time derivative at a fixed location in space can be evaluated using this Lagrangian time derivative, the mesh velocity, $\dot{x}$, and the gradient:

$$\frac{\partial \psi}{\partial t}\Big|_{x} = \frac{\partial \psi}{\partial t}\Big|_{\xi} - \dot{x} \bullet \nabla_x \psi \tag{8}$$

This form conveniently provides the time derivative of any field with a dynamic discretization by integrating over the new configuration, accounting for the change in discretization using the mesh velocity. For the time derivative of a scalar, this yields the Galerkin residual contribution,

$$\int_{\Omega} \frac{\partial \psi}{\partial t} w_i d\Omega = \int_{\Omega+} (\frac{\partial \psi}{\partial t}\Big|_{\xi} - \dot{x} \bullet \nabla \psi) w_i d\Omega + \int_{\Omega-} (\frac{\partial \psi}{\partial t}\Big|_{\xi} - \dot{x} \bullet \nabla \psi) w_i d\Omega \tag{9}$$

The only remaining issue is the definition of the mesh motion and the associated mesh velocity. In ALE, the interface is a material surface and interfacial nodes move with the discontinuity. Elsewhere, the mesh moves in an arbitrary manner. An example of an ALE implementation can be found in [Sackinger, Schunk and Rao, 1996] for 2D and extended to 3D by [Cairncross *et al.*, 2000]. This nodal mesh velocity is defined by differentiating the position of the nodes with respect to time. Using a backward difference, this gives,

$$\dot{x}_i = \frac{x_i^{n+1} - x_j^{n}}{\Delta t} \tag{10}$$

with *i=j* for the moving node. In CDFEM, however, the nodes of the parent element are fixed, and the interfacial nodes are placed at the instantaneous intersection between the parent element edges and the zero level set surface. As the level set traverses an element the interfacial nodes appear to move along the edges of the parent element. This observation motivates the current algorithm for the mesh motion. For node *i* with current location, $\mathbf{x}_i^{n+1}$, the previous location is $\mathbf{x}_j^{n}$, where the node *j* is the node that existed on the same edge at time *n*. When the edge was previously uncut, the node *j* is selected from the set of interfacial nodes at time *n* such that the length $|\mathbf{x}_i^{n+1}-\mathbf{x}_j^{n}|$ is minimized.

In this way, CDFEM exactly recovers an ALE method as the level set traverses an edge. That is, the node is considered to move along the edge. However, when a new edge is intersected by the level set, the new node is considered to have moved to its current location from the nearest node on the old interface.

Clearly other definitions of the mesh motion are possible. For example, it may be desirable to minimize the length of the relative mesh velocity, which is defined as the difference between the mesh velocity and the fluid velocity. The chosen algorithm is shown to perform well, however, for a patch test involving the advection of a weak discontinuity.

2.1.4 Finite Element Spaces

2.1.4.1 Surface Tension

Following the work of Cairncross in the context of ALE [2000], and the implicit surface tension work of Hysing [2000] the effect of surface tension is included without explicitly calculating the curvature using the surface integral,

$$\int_{\Gamma} \gamma \kappa n w_i d\Gamma = -\int_{\Gamma} \gamma \underline{\nabla} w_i d\Gamma - \Delta t \int_{\Gamma} \gamma \underline{\nabla} u \bullet \underline{\nabla} w_i d\Gamma \tag{11}$$

where $\underline{\nabla} f = \nabla f - (\mathbf{n} \cdot \nabla f)\mathbf{n}$. The second term in this implicit surface tension model is a stabilizing term that is motivated by the loose coupling between the momentum and level set equations.

2.1.4.2 Level Set Discretization

As mentioned earlier, the specific issues of the dynamic discretization depend on the continuity of the fields across the interface. In the next few subsections, the continuity of the level set, pressure, and velocity fields are considered. In possibly all published level set methods involving finite elements, the level set field is considered to be C_1 continuous across the level set interface, even if it is only C_0 across element boundaries. Even in XFEM simulations, where gradient or value enrichment could be performed, the level set field is not considered for enrichment. In CDFEM, however, where nodes are added along the interface, the natural space for the level set field is only C_0 across the interface, just like any other element boundary. The consequence of this reduced continuity is explored in the level set advection test below. These experiments show that the stability of the level set advection is adversely affected. To produce stable results, C_1 continuity must be maintained across the level set interface. In other words, for the linear triangle and tetrahedral elements used here, the level set field should be piecewise linear on the parent elements, not just on the conformal child elements. To maintain this continuity requires constraining the level set field on the interface nodes. This is accomplished in a way that is very similar to the hanging node constraints, which are generated in non-conformal adaptivity and can be removed from the system matrix using a variety of techniques such as static condensation. The interface nodes are constrained by the linear interpolant of the parent values on the edge.

2.1.4.3 Pressure Discretization

Enrichment strategies that allow for either weak or strong discontinuities have been explored in the context of XFEM for flows with and without surface tension (see Sauerland and Fries [2011] and references therein). Here the pressure is allowed to have a discontinuous value across the

interface in order to capture the effects of surface tension and discontinuous viscosity. This is easily accomplished in CDFEM by defining two pressure fields p_+ and p_- in the subdomains Ω_+ and Ω_-, respectively. Both fields are present on the interfacial nodes. For an implementation on problems without surface tension, we reduce the algorithm to a single pressure approach.

2.1.4.4 Velocity Discretization

The optimal enrichment strategy for velocity is less clear. A weak discontinuity in the velocity is produced by the viscosity difference between the fluids. For this reason enrichment of the velocity gradient has been considered [Sauerland and Fries, 2011; Rasthofer *et al.*, 2011]. Sauerland and Fries found that velocity enrichment to be problematic, however. The enrichment led to a more accurate approximation when a stable solution could be obtained, but the method was not sufficiently stable and robust. Meanwhile, Rasthofer et al. [2011] successfully enriched the velocity gradient in the context of quasi-static enrichment.

Numerical experiments performed using CDFEM have shown robustness issues when the velocity gradient is allowed to be discontinuous across the interface. One possible explanation for this lack of robustness is that the space requirements of the velocity are related to the space of the level set field. As discussed earlier, the level set field is typically piecewise continuous on an element, and, therefore, C_1 across the level set interface.

2.1.5 Finite element equations

We discretize the equations with the basic Galerkin approach, but use pressure stabilization on the continuity equation and streamline upwinding on advections terms. The momentum equation is weighted with the shape function, and second order terms are integrated by parts. All time derivatives are first order and discretized with a backward-Euler finite difference method.

$$\int_\Omega \rho \frac{u-u^n}{\Delta t} N_i \, d\Omega + \int_\Omega \rho\left(u-\dot{x}\right)\cdot\nabla u \, N_i \, d\Omega + \int_\Omega \left[-P\,I + \mu\left(\nabla u + \nabla u^t\right)\right]\cdot\nabla N_i \, d\Omega - \int_\Omega \rho g \, N_i \, d\Omega + \int_\Gamma S \, N_i \, d\Gamma = 0 \quad (12)$$

For the continuity equation, pressure stabilization adds extra terms that circumvent the LBB equation allowing for equal order interpolation.

$$\int_\Omega \nabla\cdot u W_i \, d\Omega + \int_\Omega \tau_u \left[-\nabla P + \rho g\right]\cdot\nabla W_i \, d\Omega = 0$$

$$W_i \Rightarrow N_i + \tau_u \, u\cdot\nabla N_i, \; \tau_u = \left[\left(\frac{2}{\Delta t}\right)^2 + u_i g_{ij} u_j + 12\left(\frac{\mu}{\rho}\right)^2 g_{ij} g_{ij}\right]^{-\frac{1}{2}} \quad (13)$$

The level set equation is also stabilized with a streamline-upwinding Petrov-Galerkin (SUPG) term that creates upwinding for this advection dominated equation. (We have also used Taylor-Galerkin upwinding).

$$\int_{\Omega} \frac{\varphi - \varphi^n}{\Delta t} W_i \, d\Omega + \int_{\Omega} u \cdot \nabla \varphi W_i \, d\Omega = 0$$
$$W_i \Rightarrow N_i + \tau_\varphi \, u \cdot \nabla N_i, \; \tau_\varphi = \left[\left(\frac{2}{\Delta t} \right)^2 + u_i g_{ij} u_j \right]^{-\frac{1}{2}} \tag{14}$$

2.2 Verification of CDFEM

Verification of the CDFEM algorithm was carried out on several problems addressed in the literature such as two-dimensional droplet/bubble rise and the two-dimensional Rayleigh-Taylor instability. Here we choose to focus on the unconstrained version of the algorithm where all fields are allowed to vary at the child level and are not constrained to the parent mesh as some of our other algorithms, which will be discussed later. All two-dimensional simulations are carried out of triangular element meshes with Q1 interpolation of all variables, and pressure-stabilized-Petrov-Galerkin (PSPG)-type stabilization to circumvent the LBB condition [Hughes, 2000]. First order time integration is used with SUPG on all advection terms.

2.2.1 Droplet/Bubble Rise a la Hysing

The first set of problems are drop and bubble rise problems in 2D from Hysing et al., [2009] where they present results from several different codes. Important dimensionless groups are the Reynolds number and the Eotvos number, and property ratios for the two fluids. The values for these two problems, indicated by Test 1 and Test 2 respectively, are given in Figure 8.

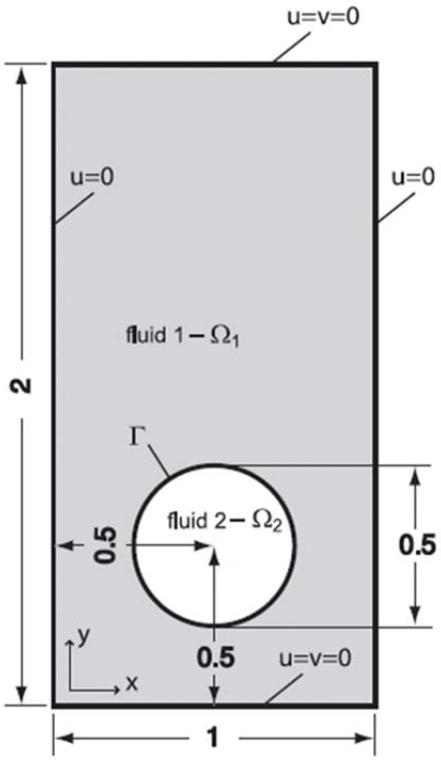

$$\mathrm{Re} = \frac{2\rho_1 U_g R_0}{\mu_1},\ Eo = \frac{2\rho_1 U_g^2 R_0}{\sigma},\ \frac{\rho_1}{\rho_2},\ \frac{\mu_1}{\mu_2} \text{ where } U_g = \sqrt{2gR_0}$$

Table I. Physical parameters and dimensionless numbers defining the test cases.

Test case	ρ_1	ρ_2	μ_1	μ_2	g	σ	Re	Eo	ρ_1/ρ_2	μ_1/μ_2
1	1000	100	10	1	0.98	24.5	35	10	10	10
2	1000	1	10	0.1	0.98	1.96	35	125	1000	100

Figure 8. Two-Dimensional droplet and bubble rise problems from Hysing et al., 2009.

Test 1 deforms smoothly from the initial circular configuration and gives a smooth profile after 3.0, producing a cap-like shape. All methods seem to do well on this problem including a diffuse interface method (Figure 9). The density and viscosity ratios are 10, Re=35 and Eo=10.

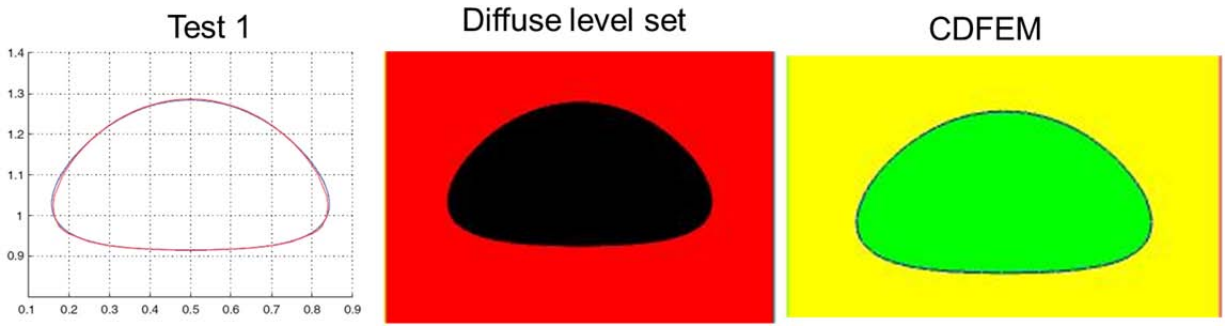

Figure 9. Results from Test 1. Left shows the published results from Hysing et al., 2009, middle gives the diffuse interface results, and right shows the CDFEM results. Results are given for the coarsest mesh (1/40).

We can examine the results from Test 1 as a function of mesh refinement. Here three mesh resolutions are examine R0=1/40, R1=1/80 and R2=1/160. Following Hysing *et al.* [2009], we examine three metrics from the simulation: the circularity, center of mass, and rise velocity. The circularity is a measure of how close the drop compared to circular.

$$\text{circularity} = \frac{\text{perimeter of area-equivalent circle}}{\text{perimeter of bubble}} = \frac{\pi d_a}{P_b} \tag{15}$$

The center of mass is defined as the x-moment of the drop divided by the droplet area.

$$\text{center of mass} = \frac{\int_A x dx dy}{\int_A 1 dx dy} \tag{16}$$

The rise velocity is defined as the integral of the velocity over the droplet divided by the droplet area, which can also be an evolving quantity.

$$\text{rise velocity} = \frac{\int_A u_x dx dy}{\int_A 1 dx dy} \tag{17}$$

Here, we can test whether they are convergent with mesh refinement. The results from this study are shown in Figure 10. This shows good convergence as the mesh is refined, with the results from R1 and R2 lying almost on top of each.

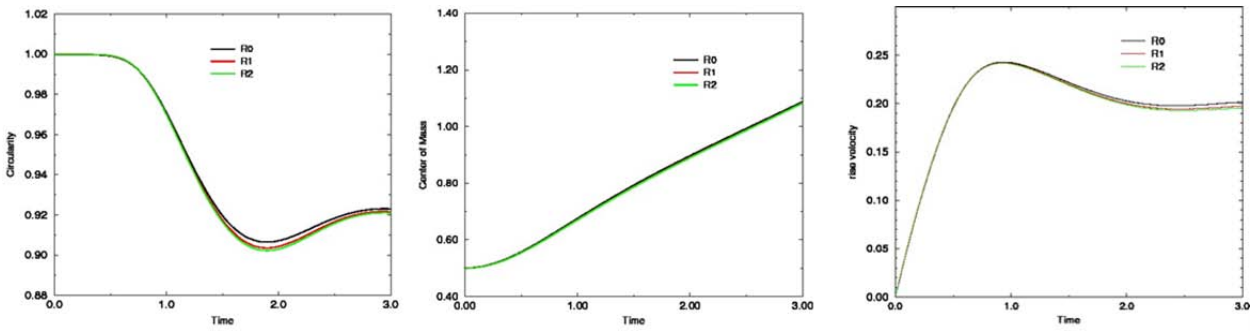

Figure 10. For problem Test 1, CDFEM shows good convergence with mesh refinement for circularity, center of mass, and rise velocity metrics.

Mass conservation is always an issue for level set methods. Here we examine the maximum deviation from the initial mass as a measure of the error in the simulations. This is shown in Figure 11.

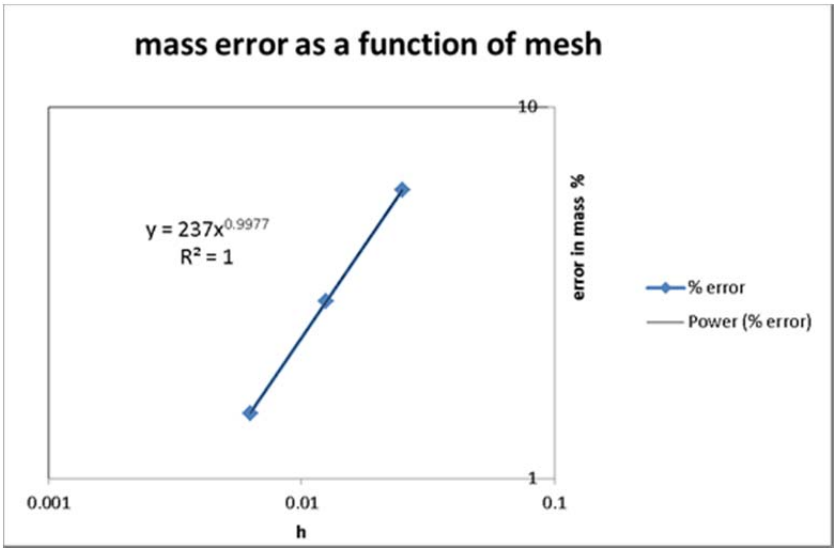

Figure 11. Error in mass conservation as a function of mesh refinement (h=1/40, h=1/80, and h=1/160). Unconstrained CDFEM shows roughly first order accuracy on a smooth problem such as Test 1.

Thus the unconstrained CDFEM demonstrates itself to be a convergent method, accurate to first order on smooth problems.

Test 2 serves as a more stringent test of the algorithm, at a density ratio of 1000 and viscosity ratios of 100, (Re=35 and Eo=125). Fine trailing structures form below the drop as it rises in the fluid. The shape of these structures is different for the varying algorithms, as seen from Figure 12.

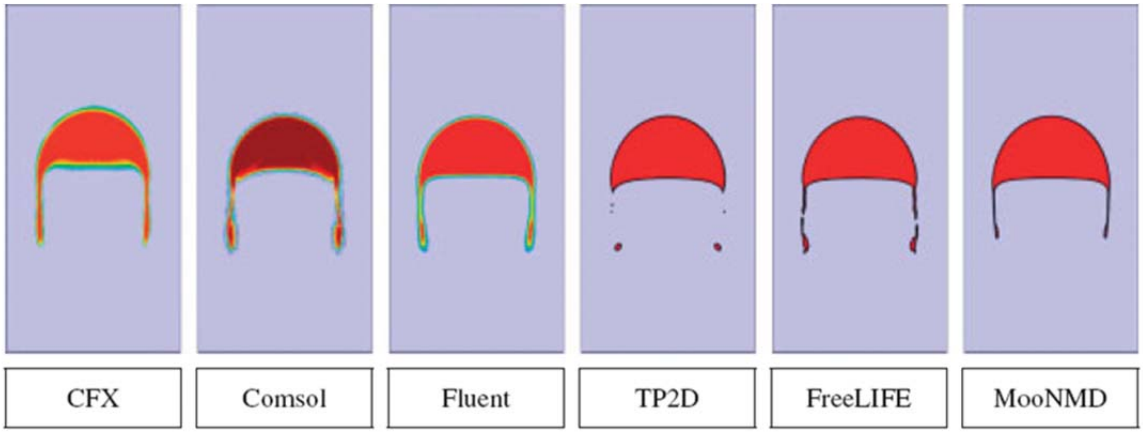

Figure 12. Figure 1 from Hysing et al., 2009 showing results for Test 2 from various codes. The diffuse interface methods produced from CFX, COMSOL and Fluent look different from the sharp interface method (TP2d) and the ALE moving mesh code (MooNMD).

Here we have results for CDFEM on Test 2 from the unconstrained algorithm, using frequent renormalization, and local normals (see Figure 13).

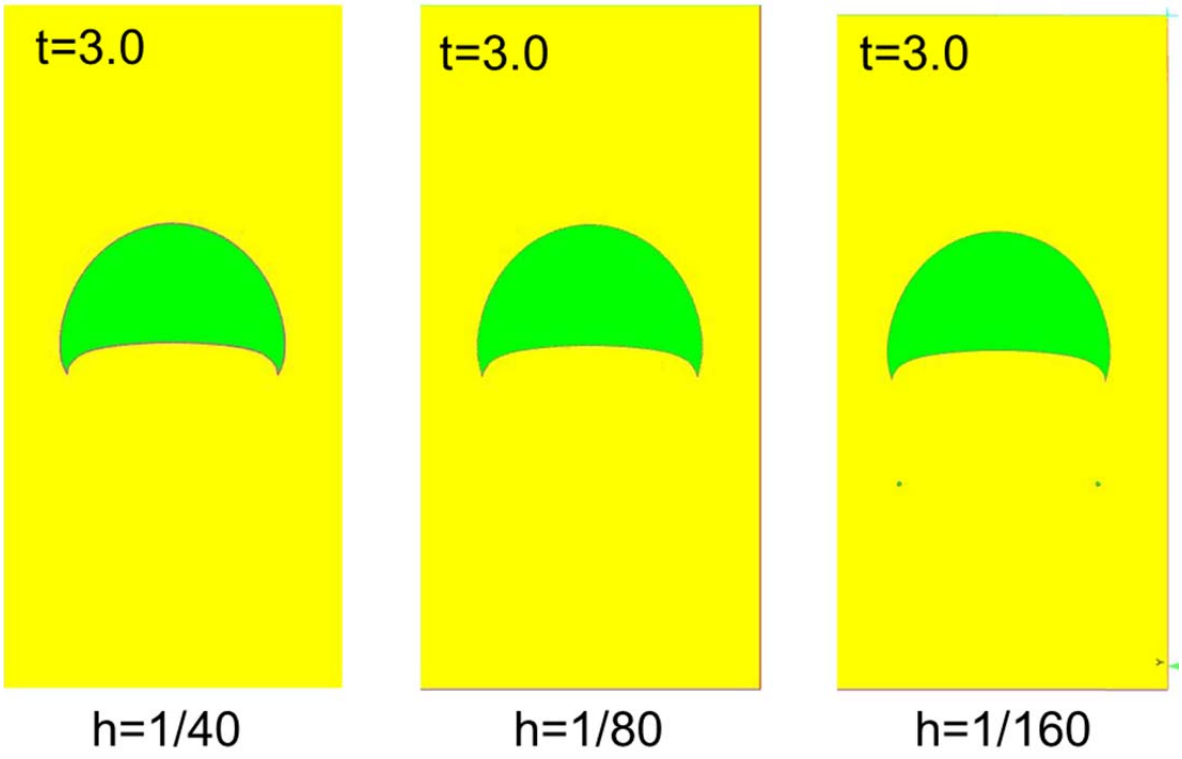

Figure 13. Unconstrained CDFEM results for Test 2 showing convergence with mesh refinement for gross features, but loss of fine features such as trailing tails or satellite drops.

The results show convergence in the gross features on all three meshes. On the coarser meshes (h=1/40 and h=1/80), we find that satellite drops form but then are small enough compared to the

grid size that they disappear. This is true even though overall mass conservation is quite good. The satellite drops contain very little of the problem mass.

We have also examined the rise velocity as a function of mesh refinement in Figure 14.

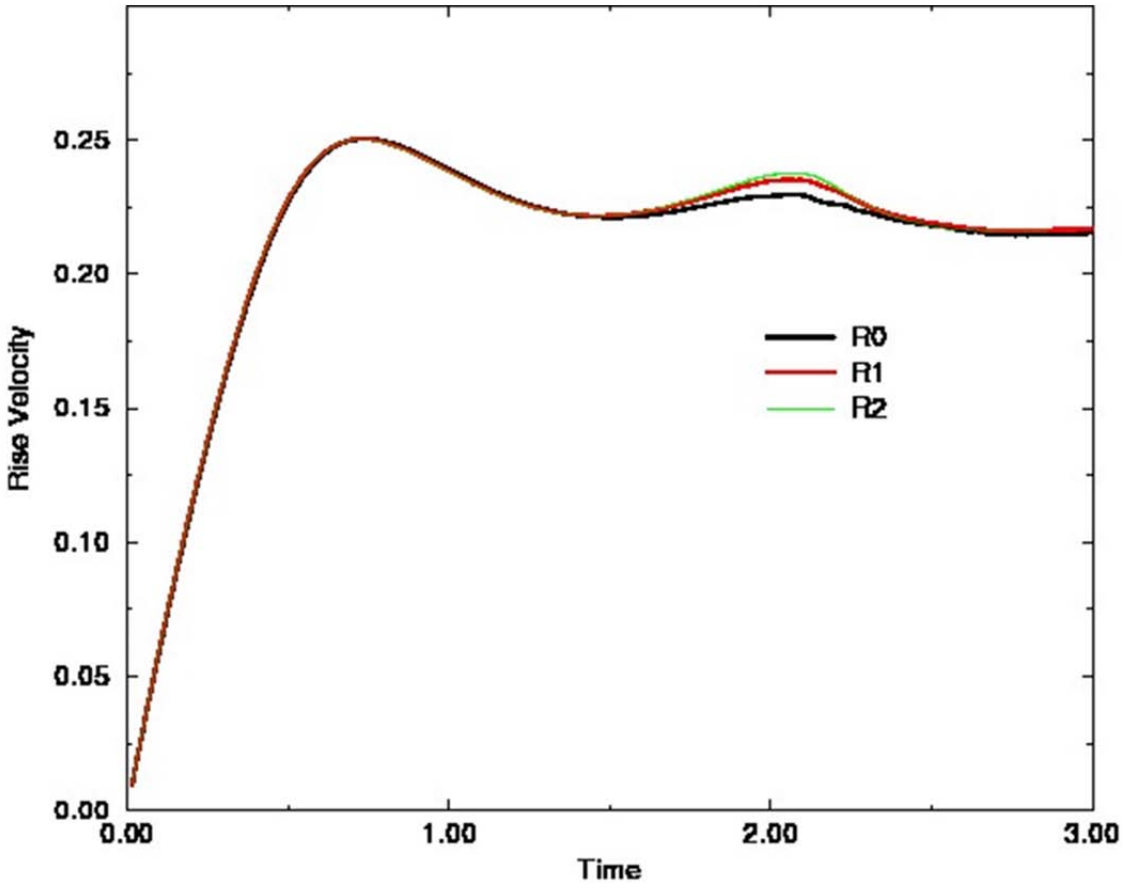

Figure 14. Rise Velocity as a function of time and mesh refinement for unconstrained CDFEM on Test 2.

Here we can see that the results for all three meshes lie almost on top of each other, except in the area where we start losing the satellite drops at roughly time=2s. Still R1 and R2 show good convergence throughout.

2.2.2 Rayleigh-Taylor Instability

A classic test for a moving boundary algorithm is the Rayleigh-Taylor instability, where a simulation begins with an unstable stratification of heavy fluid over light fluid. Here we set up the problem in an identical manner to the Rayleigh-Taylor instability from Smolianski [2005]. The initial conditions, boundary conditions, and material properties are show in Figure 15. Initial condition for the shape of the interface affects wave number and symmetry of instability. Here we perturb the interface with a symmetric deformation.

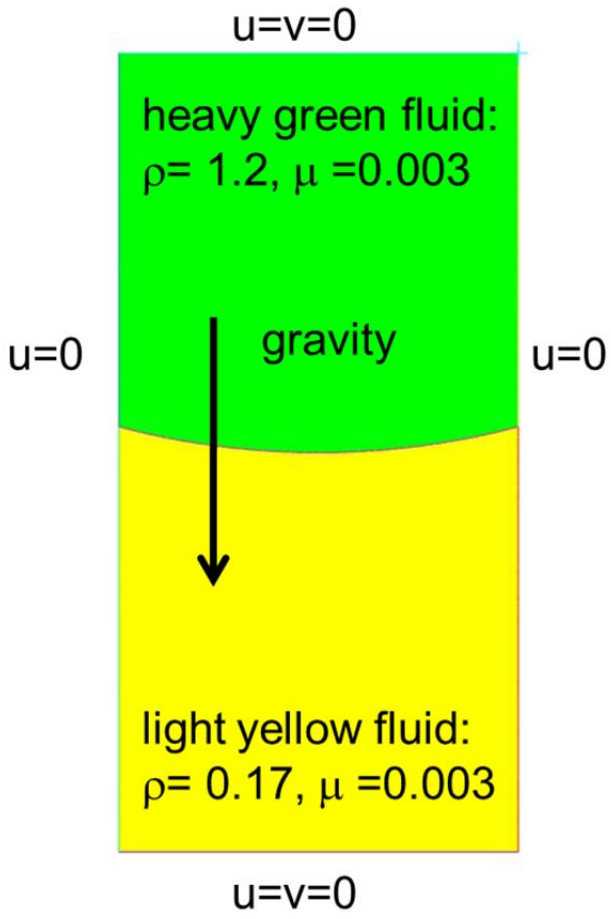

Figure 15. Problem set up for 2D Rayleigh-Taylor instability including physical properties for both phases, and boundary conditions. The interface is perturbed with a symmetric function to excite a symmetric instability.

Results are given from Smolianski in Figure 16 on a coarse mesh (h=1/40) and a large time step.

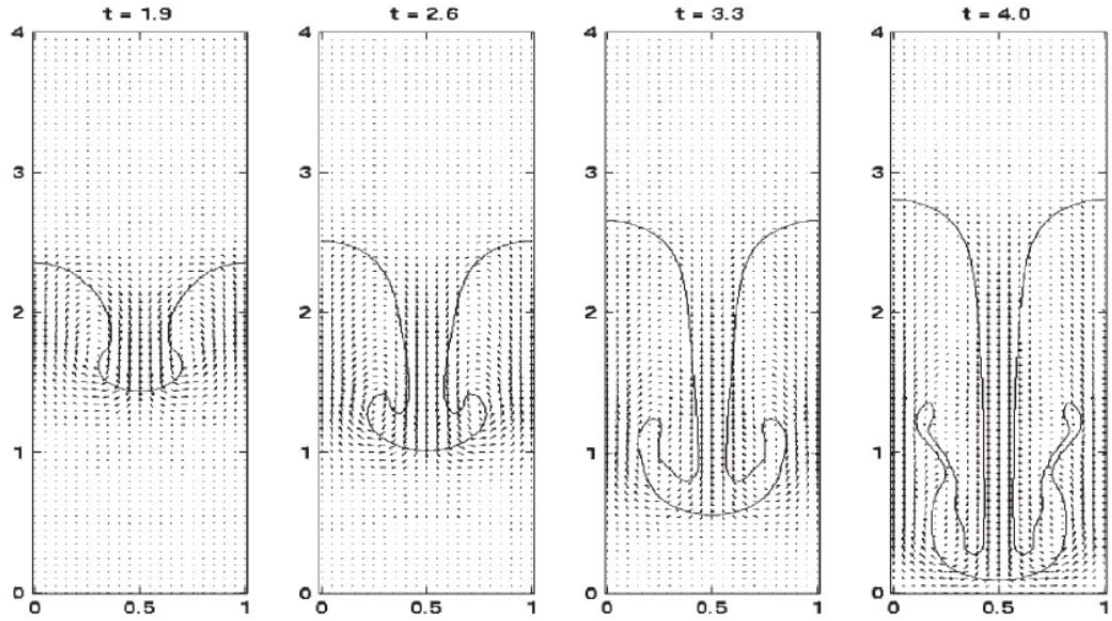

Figure 16. Rayleigh-Taylor instability with zero surface tension on h=1/40 and $\Delta t=2h$ from Smolianski [2005].

Results are given for zero surface tension, where a single pressure is used in our CDFEM formulation. Because there is larger deformation than in the case with surface tension, this is a stringent test. Fine features are formed, which should stretch without breaking. When they do break, it is a numerical effect since the simulation is two-dimensional and there is no surface tension. Figure 17 shows CDFEM results for four different meshes at four different time planes.

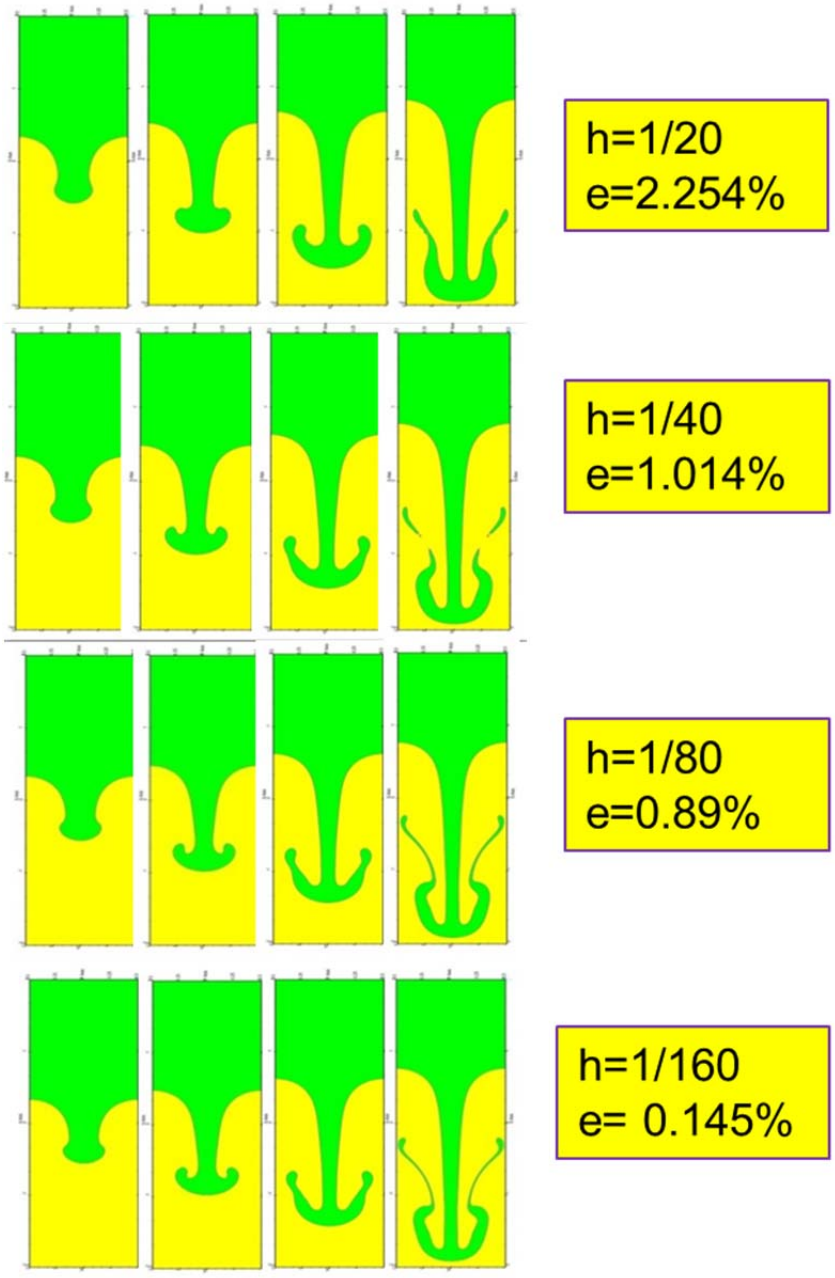

Figure 17. CDFEM Rayleigh-Taylor instability results for four different meshes at four different time planes (t=1.96, 2.6, 3.3, 4.0). Also included is an error measure, the maximum mass loss before 4.0s. The time step is based on the element size, $\Delta t=h/3.0$. Standard renormalization occurs at every 0.05s for each mesh.

From Figure 17 we can see that the algorithm is convergent. On the coarsest mesh (h=1/20), the solution is very diffusive and does not contain any fine features. As we refine the mesh, we begin to see the fine features but obtain a filament that breaks for h=1/40. As we go to the finer meshes (h=1/80 and h=160), we see nearly identical results where a fine filament is formed at the last time plane and able to maintain itself while thinning.

We can look at a quantitative error metric, which is the maximum area loss in the first 4s from an initial area is 2.0 (see Figure 18).

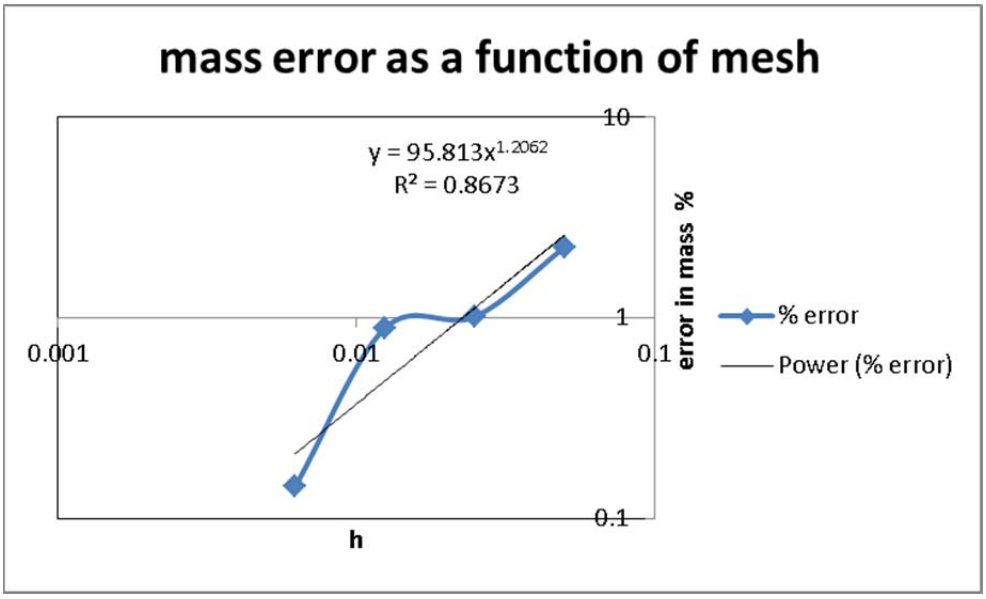

Figure 18. Mass error as a function of mesh refinement for Rayleigh-Taylor

Convergence looks slightly higher than first order (though not shown here, the constrained CDFEM is lower than first order). The plot is not monotonic, and shows a change of slope from h=1/40 to h=1/80, with the finer meshes showing a higher convergence rate. For this problem, filament breakage/topology change may be the cause of the non-monotonic error curve.

2.2.3 3D Droplet in Shear Verification

Many of the verification problems in the literature are two-dimensional such as the droplet rising and Rayleigh-Taylor instabilities we included in the previous sections. Unfortunately, most of the problems that we are interested in are three-dimensional. To that end, we have investigated a three dimensional verification problem of a droplet flow in shear flow. The drop begins as a sphere and then deforms due to the flow into a capsule-like shape. We look at three different mesh resolutions (50,000 nodes, 100,000 nodes and 200,000 nodes) for meshes of tetrahedra. CDFEM mesh refinement is much more complicated in three-dimensions, and this test case was able to highlight several bugs in the code that had to be fixed in order to achieve results.

Results for a 3D drop in shear flow are given in Figure 19. Surface tension is included and the physical properties are identical for the both phases, though they are immiscible and have a jump in pressure across the interface due to surface tension. Constrained renormalization is used periodically as the level set diverges from being a distant function.

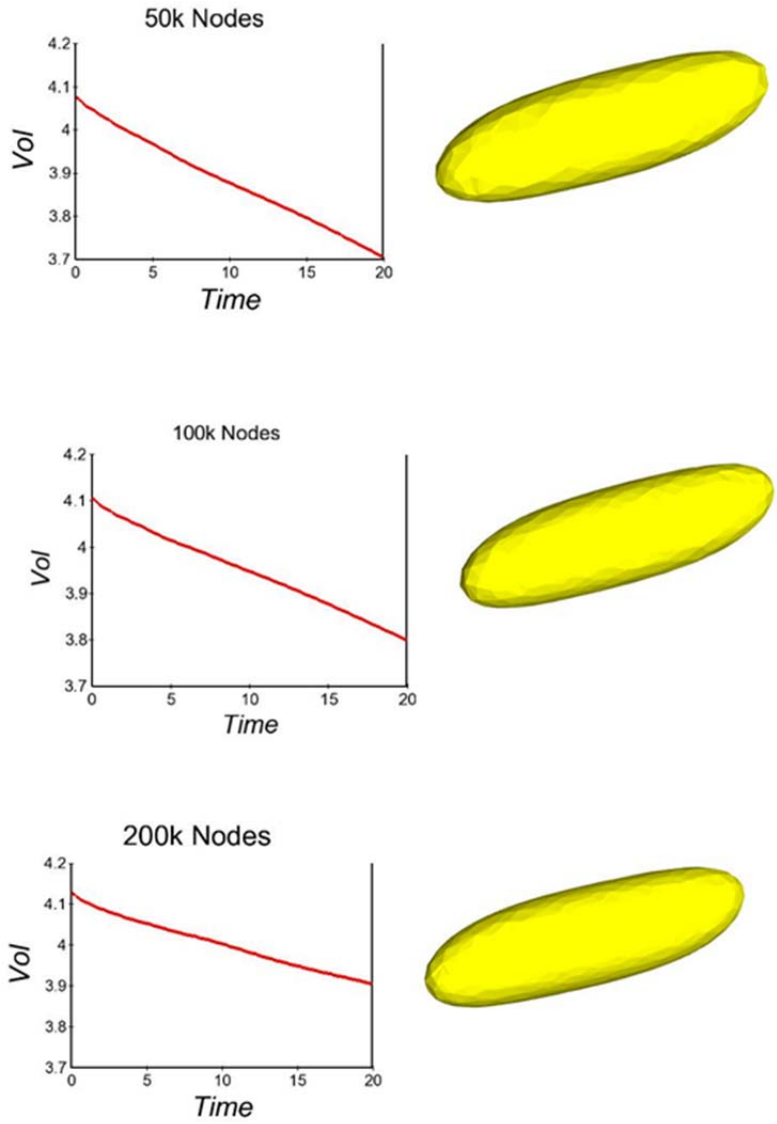

Figure 19. 3D drop in shear flow for three different meshes.

From this example problem, we can see that the shape of the drop is quite consistent for all three meshes at the final time of 20s. Figure 20 shows the maximum mass loss normalized by the initial mass for the three different meshes plotted as a function of h, a linear measure of the mesh size.

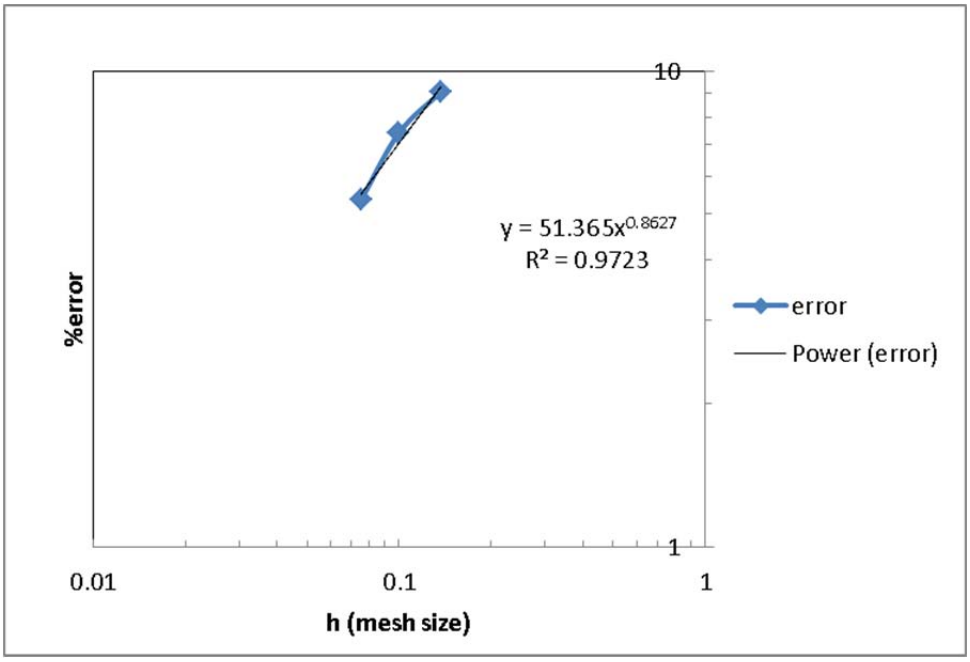

Figure 20. Mass error as a function of mesh refinement for 3D drop in shear flow.

Mass conservation does improve as the mesh is refined, though mass loss continues to be an issue for problems with low capillary number. From Figure 20, we can see that the error decreases in a first-order fashion with mesh size.

2.2.4 Constrained Algorithm CDFEM Unconstrained CDFEM

Many different version of the CDFEM algorithm were investigated, and only two proved unconditionally stable. The unconstrained CDFEM, where all variables were mapped to the child space allowing for jumps in velocity gradient and discontinuous pressure, was stable. The fully-constrained CDFEM, where all variables were mapped to the parent space, except for pressure, which was allowed to be discontinuous as necessary for problems with capillarity, was also stable. Variations in between these cases were all unstable.

An example of the results for the Hysing bubble rise problem with the two stable algorithms is given in Figure 21.

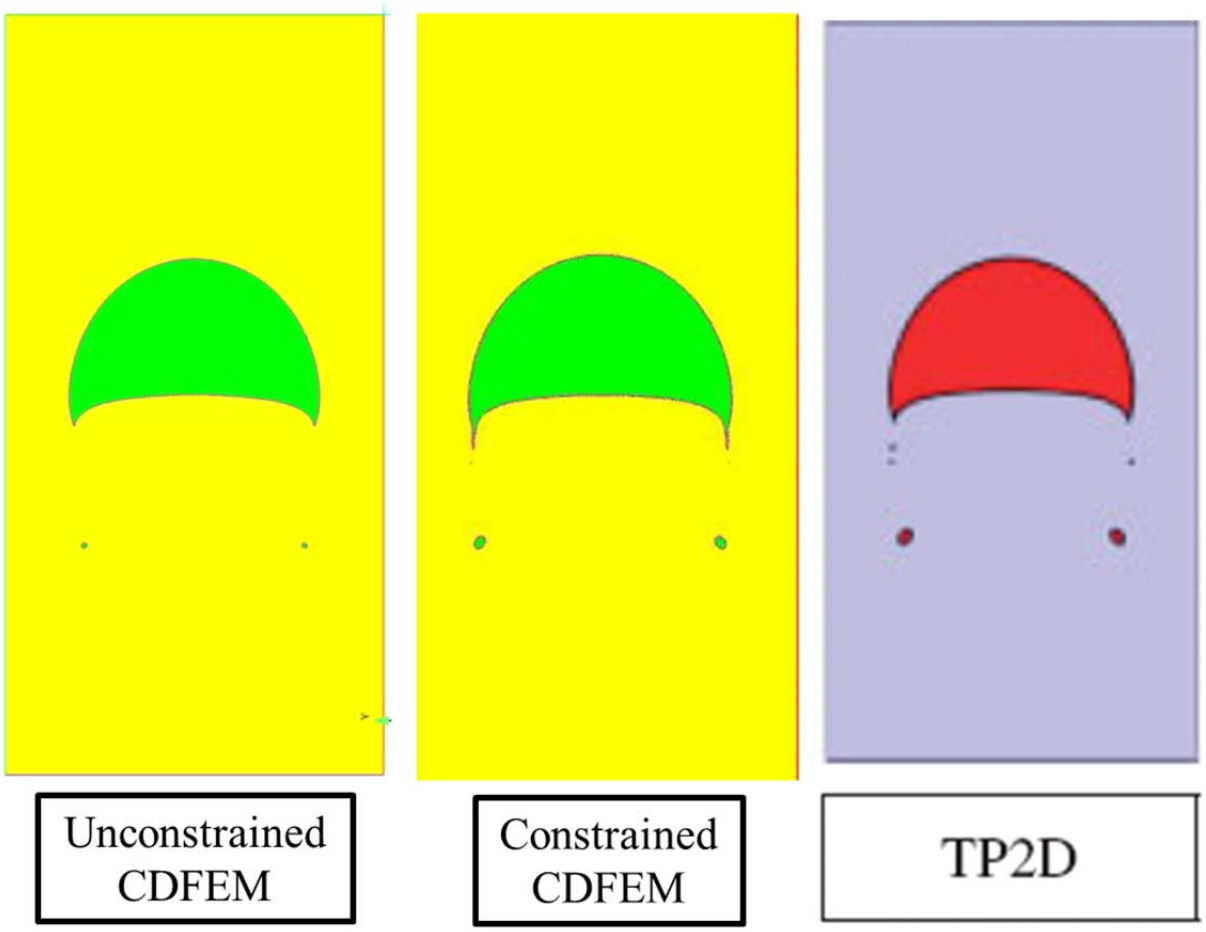

Figure 21. Unconstrained CDFEM algorithm for Hysing problem 2 on the most refined mesh as compared to a constrained CDFEM for the same mesh. Hysing result is shown from his paper for comparison.

The constrained algorithm seems to be somewhat better at mainraining small features such as the satellite drops that form as the bubble rises. Loss is higher for the mass in the satellite drops for the unconstrained algorithm, though overall mass conservation is similar for both methods since very little of the problem mass is contained in the satellite drops.

2.3 Mass Transport with CDFEM

One of the natural strengths of the CDFEM algorithm is that the interface between the two fluids has a meshed interface, upon which we can apply boundary conditions, jumps in material properties, and discontinuous variables. In liquid-liquid extraction, interfacial mass transport is crucial to the separation process. A cartoon of this process is given in Figure 22 where mass moves from phase A into phase B, and also in the reverse direction, in an equilibrium process. The concentration is discontinuous across the phase boundaries.

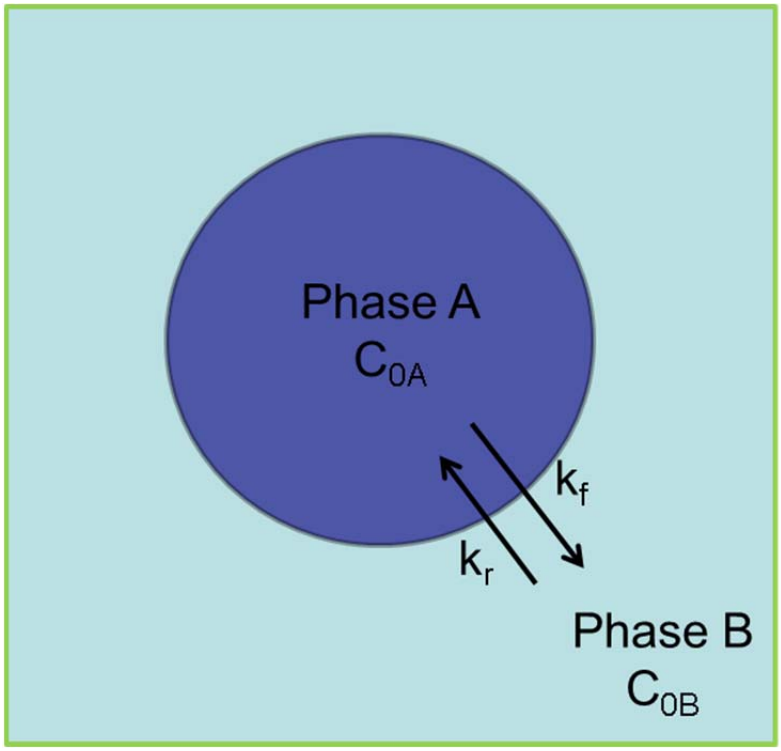

Figure 22. A schematic of the interfacial mass transport where material goes from phase A to phase B in equilibrium. A concentration jump occurs at the interface between phase A and B.

We can write a transport equation for each phase:

$$\begin{aligned} \frac{\partial c_0}{\partial t} + u \bullet \nabla c_0 &= \nabla \bullet (D_{0A} \nabla c_0) \text{ phase A} \\ \frac{\partial c_1}{\partial t} + u \bullet \nabla c_1 &= \nabla \bullet (D_{1B} \nabla c_1) \text{ phase B} \end{aligned} \tag{18}$$

When we apply the Galerkin finite element method, a shape function representation of the concentration variables is formed based on the nodal variables. This is then substituted into the differential equation for transport. It is then weighted by the shape function itself, and second derivatives are integrated by parts. Here we write the equation for the generic concentration variable, but it is applicable to both phases:

$$R_i^{mass} = \int_V (N_i (\frac{\partial c}{\partial t} + u \bullet \nabla c) - \nabla N_i \bullet D \nabla c) dV + \int_S n \bullet D \nabla c dS = 0 \tag{19}$$

The surface integral in equation (19) is the natural boundary condition that occurs on all interfaces and boundaries. At the interface, this term is balanced by the interfacial mass transport equation written for concentration variables, c_0 and c_1:

$$
\begin{aligned}
&rate = k_f c_0 - k_r c_1 \\
&\int_S n \bullet (D_{0A} \nabla c_0 - rate) dS = 0 \\
&\int_S n \bullet (D_{1B} \nabla c_1 + rate) dS = 0
\end{aligned}
\tag{20}
$$

We test this formulation for the problem of a quiescent 2D drop with the properties given in equation (21).

$$
\begin{aligned}
&k_f = 1, \; k_r = 2 \\
&D_{0A} = D_{1B} = 0.05 \\
&C_0^{init} = 1, C_1^{init} = 0
\end{aligned}
\tag{21}
$$

The results are shown in Figure 23. Here we see the species of interest starts off contained inside the drop. It then slowly leaches out into the external fluid. This fluid starts off with a zero concentration of this species.

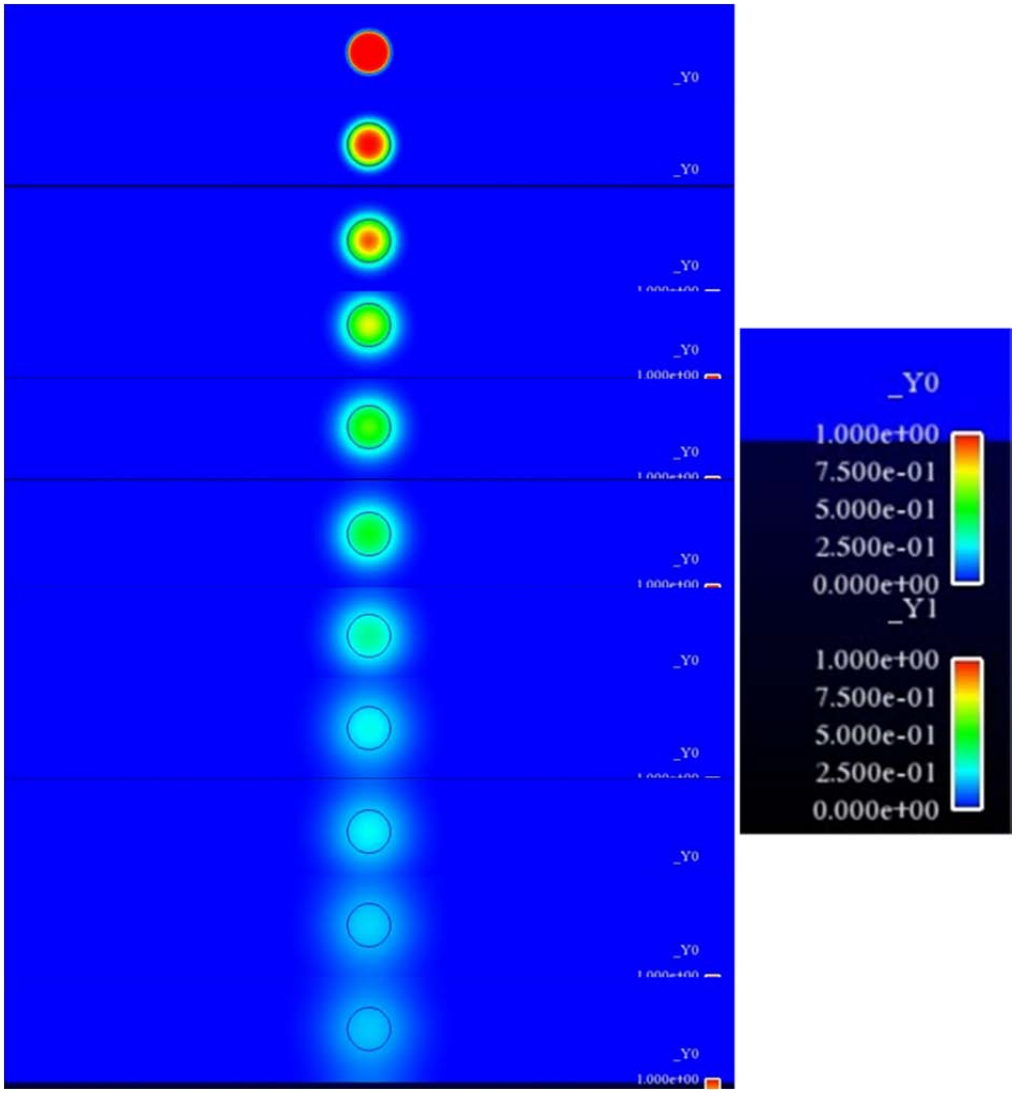

Figure 23. Interfacial mass transport from a quiescent drop in 2D where Y0 is the species in the droplet phase and Y1 is its counterpart in the continuous phase. Time evolves from top to bottom.

For this problem, no flow occurs so mass transport occurs only by diffusion and interfacial mass transport. A short time, the mass transport is fast compared to diffusion and a boundary layer is formed in the drop that is depleted of species 0. Since the mass transport rate depends on the concentration of species 0, it slows over time and allows diffusion to catch up. At late time, the material diffuses away from the drop in phase B creating a halo effects.

We can also couple the mass transport to flow for the deforming bubble from Test 2 shown previously. This result is shown in Figure 24, with the same properties as the previous example but including the effects of convective mass transport.

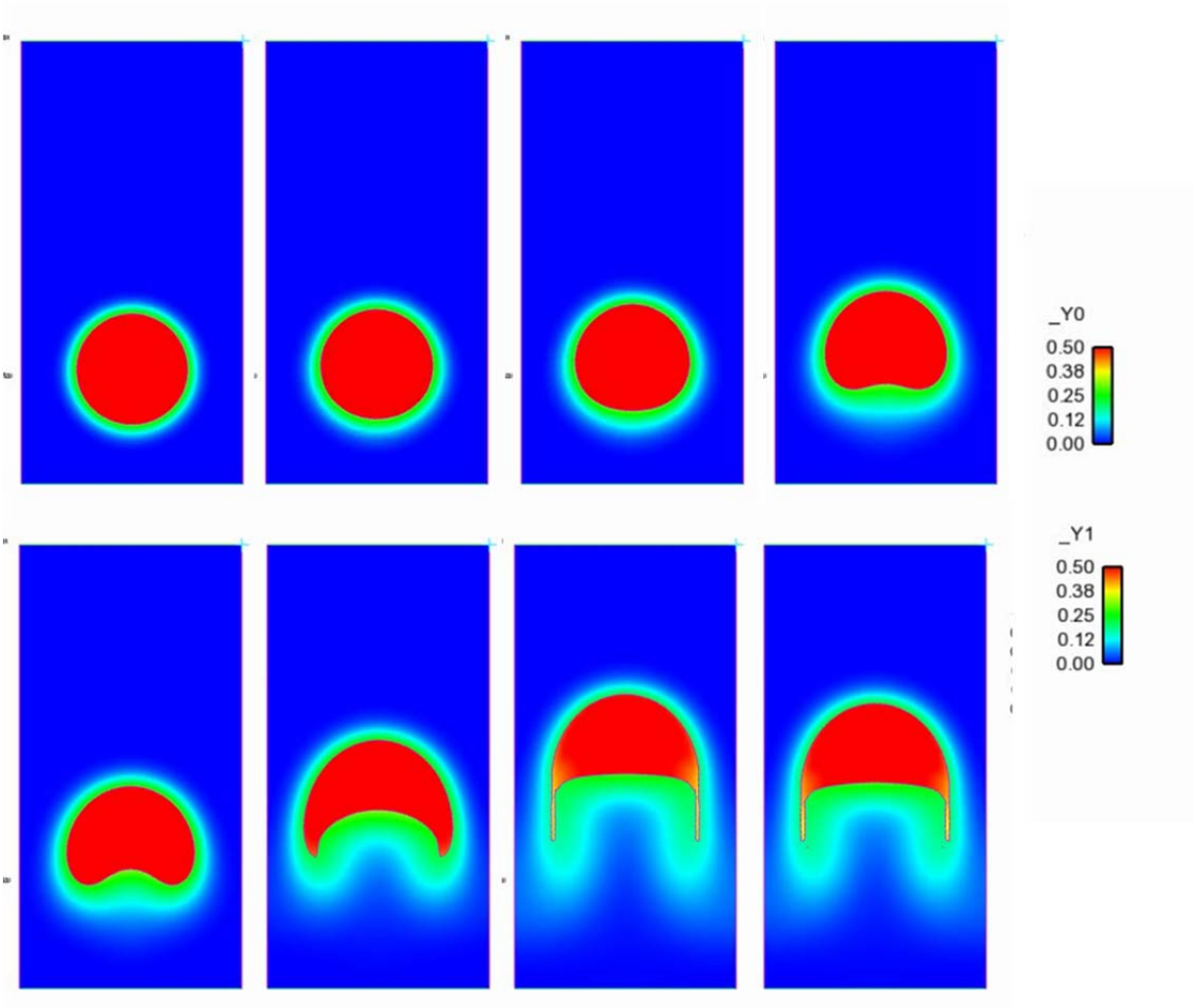

Figure 24. Test 2 with interfacial mass transport. The top left figure is the initial time plane, and time evolves from left to right. The bottom left is the fifth time plane.

Here we can see that the motion of the drop leaves a wake of species 1 in the phase B, enhancing mass transport compared to diffusion alone. For this problem, the drop remains well-mixed since only the first 3s were examined.

A 3D version of this algorithm is also available in Sierra Mechanics, though we currently have a parallel bug that constrains us to run on a single processor, which greatly hampering our ability to run realistic drops.

2.4 CDFEM Coupling to Control Volume Finite Element Method

The goal for this component of the project was to have the capability to run a multi-phase flow wedge calculation of a contactor at the highest Reynolds number possible and to achieve the highest performance possible within available computational resources. The Conformal Decomposition Finite Element Method (CDFEM) is utilized in order to represent droplet

surfaces as sharp, moving interfaces. To maximize computational performance, the Control Volume Finite Element Method (CVFEM) with an approximate projection scheme was chosen since CVFEM is robust for high Reynolds number flows and the segregated pressure approach should be more efficient for large scale computations. The code development effort has been to combine these three elements to work congruently within the SIERRA/Aria framework.

The following code modifications have been put in place to allow for CDFEM mesh decomposition to link with CVFEM:

(1) CVFEM now functions with triangles/tetrahedral elements since CDFEM mesh decomposition is implemented for only these element types.

(2) Changes have been made to the CVFEM level set equation to include a conformal decomposition utility and expression save-off utilities have been updated to allow for CDFEM mesh motion.

(3) The nodal control volume now gets properly updated for CDFEM mesh motion, in addition to ALE mesh motion.

(4) Additionally, there are two formulations of the CVFEM equations for continuity and momentum available in Aria, both of which require source terms proportional to the mesh velocity (or mesh velocity relative to the fluid velocity) as well as interfacial flux boundary conditions that must be included to account for a density jump across the interface within a control volume. The first formulation is:

$$\int_{\Omega} \frac{\partial(\rho\phi)}{\partial t} dV - \int_{\Omega} \dot{x} \nabla \bullet \rho\phi dV + \int_{\partial\Omega} \rho\phi v \bullet n dA = 0 \ , \tag{22}$$

where **v** is the fluid velocity and $\dot{x}$ is the mesh velocity. The second formulation is:

$$\int_{\Omega} \frac{\partial(\rho\phi)}{\partial t} dV - \int_{\Omega} \rho\phi \nabla \bullet \dot{x} dV + \int_{\partial\Omega} \rho\phi (v - \dot{x}) \bullet n dA = 0 \ . \tag{23}$$

The second terms are the source terms mentioned above and the third terms are the additional boundary terms.

Both of these forms have been tested and are correct to machine precision for a convecting drop with a density ratio of 1:1000. Two regression tests have been added to the Aria test repository: (1) an interface drop convection problem with a high density ratio and (2) a rising droplet problem (due to gravity and density ratio) that includes surface tension and double-valued pressure.

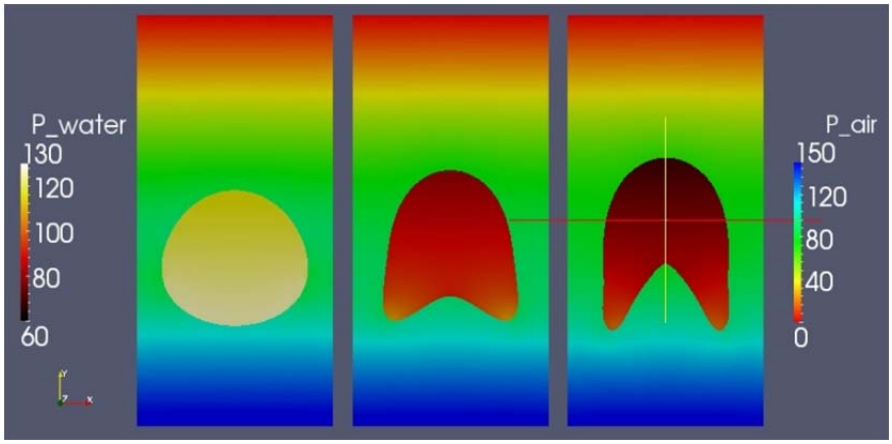

Figure 25. The CVFEM/CDFEM rising droplet test problem for 3 different surface tensions. Drop rises due to gravity force and density ratio between drop and external fluid. Double-valued pressures are used to capture the interfacial pressure jump. A fully coupled solve is utilized here.

The use of double-valued pressures to represent sharp interfacial pressure jumps that occur when surface tension is non-negligible has been investigated. The following code modifications have been made to allow for double-valued pressure with CVFEM and a projection method: (1) Indices are included to tag the continuity equation and the pressure, which gets passed into the mass flux vector and CVFEM utilities. This index also gets added to utilities that require pressure. (2) A pressure jump contact flux interfacial boundary condition has been added such that the average between the current and opposite surface terms is used. (3) Steps have been taken to ensure that the projection step is consistent with the momentum equation at the interface. Once the code was set up to handle double-valued pressure with a segregated pressure solve, it was determined that this combination does not appear to provide satisfactory convergence. It is possible that instead a single pressure segregated solve with a level set balance force approach may prove to be a better option, however this approach negates a fraction of the benefits of CDFEM's sharp interfacial representation. At the large scale of the problem, computational performance is more necessary than well-defined droplet boundary conditions.

3 PARTICLE-SCALE AND DROPLET-SCALE MODELS

In this section, we discuss modeling results for CDFEM. When we first began using CDFEM for problems with moving boundaries, many issues came up as compared to the steady case [Noble, Newren, and Lechman, 2010]. For that reason, we decided to step back and clarify the algorithm for the simpler case of a solid-particle with a prescribed velocity. This work resulted in a journal publication [Lechman, Noble, and Nemer, 2012]. Thus, only a short summary is given here along with an update of the work. In the other sections, we discuss droplet-scale modeling using CDFEM in a flow-focusing device. Other applications of CDFEM are also highlighted to show the versatility of the algorithm for capillary hydrodynamics and two-phase flows.

3.1 Particle-scale modeling with CDFEM

Particle suspensions play an important role in many engineering applications, yet their behavior in a number of respects remains poorly understood. In conjunction with careful experiments, modeling and simulation of these systems can provide key insight into their complex behavior. However, these two-phase systems pose the challenge of simultaneously, accurately, and efficiently capturing the complex geometric structure, kinematics, and dynamics of the particulate discrete phase and the discontinuities it introduces into the variables (e.g., velocity, pressure, density) of the continuous phase. To this end, a new conformal decomposition finite element method (CDFEM) is introduced for solid particles in a viscous fluid. The method is verified in several simple test problems that are representative of aspects of particle suspension behavior. In all cases, we find the CDFEM to perform accurately and efficiently leading to the conclusion that it forms a prime candidate for application to the full direct numerical simulation of particle suspensions.

We have presented the results of several problems involving rigid discrete particles in an incompressible, Newtonian continuum fluid. The problems are simple but prototypical of aspects of the behavior of particulate suspensions. We have been able to verify the efficacy of the CDFEM as applied to these types of problems. Specifically, we have shown that the method performs quite well in the quasi-static limit with dynamic interfaces and coupling to a particle dynamics solver. Additionally, when the elements of the decomposition become ‘extreme’, as in the case of surfaces in close contact, CDFEM performs at least as well as other methods. In some sense, perhaps, it performs better as the lubrication forces are stronger but not singular at contact. In cases where full 3D transient flows with dynamic interfaces are relevant, CDFEM shows accuracy as good as an ALE method. Hence, CDFEM allows for efficient, accurate introduction of discontinuities to the continuum fields, which makes it very well suited for simulations of particle suspensions. Figure 26 shows an example of a CDFEM particle from the paper.

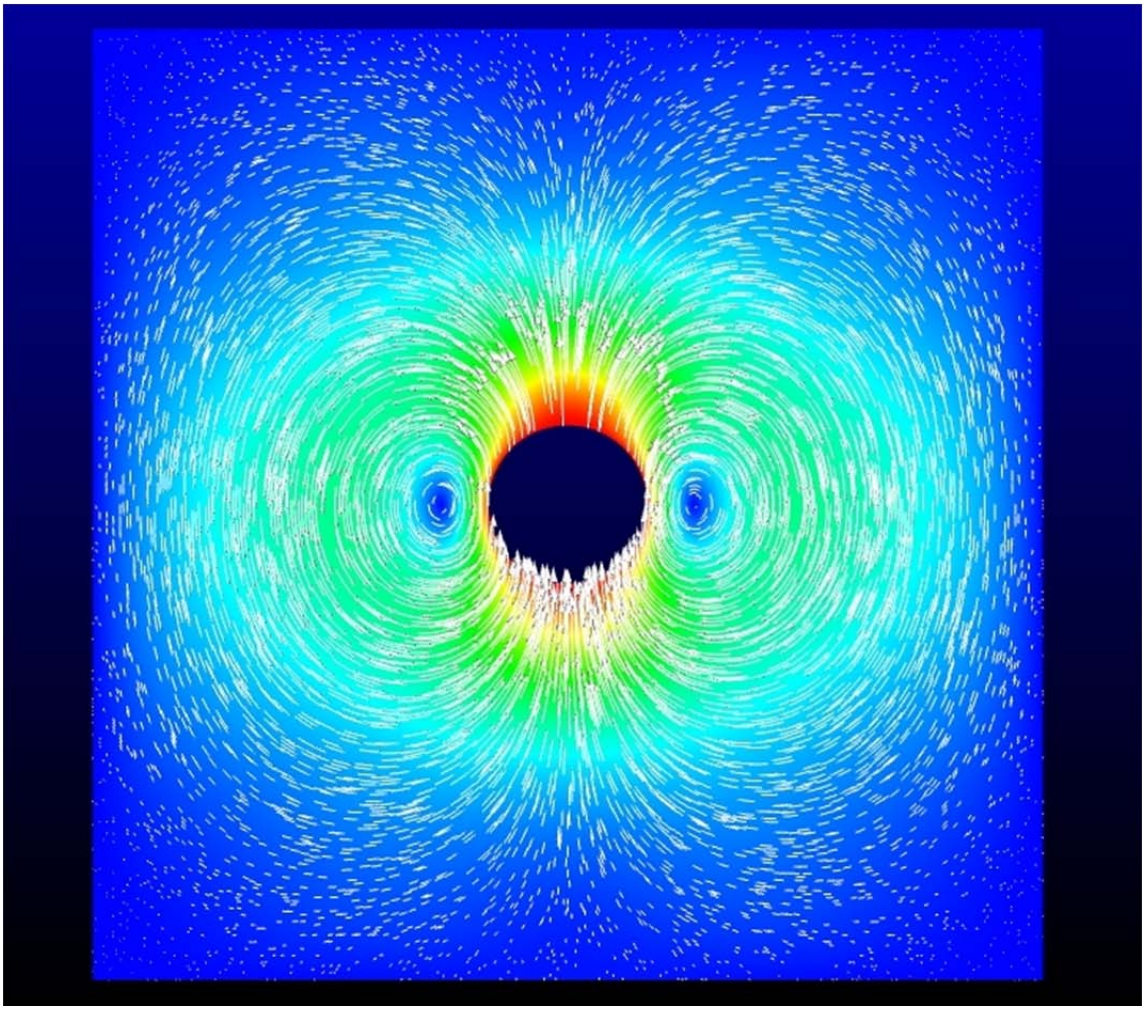

Figure 26. Typical flow field produced by sphere driven by constant force. Colors indicate magnitude of fluid velocity and vectors indicate direction.

In particular, sedimentation of a cloud of particles or flows with free surfaces can be handled with this approach. One final note is on the application of this type of approach to suspension behavior. Although the method may be limited in length and timescales that are achievable given current computational resources, it certainly can play a role in constitutive model development in representative volume element-type simulations. This is due to the fact that it captures the relevant physics of suspension flows, namely, the complex geometric structure and dynamics of the particulate discrete phase and the discontinuities it introduces into the field variables of the continuous phase.

The work has been extended to 3D multi-particle flows as seen from Figure 27.

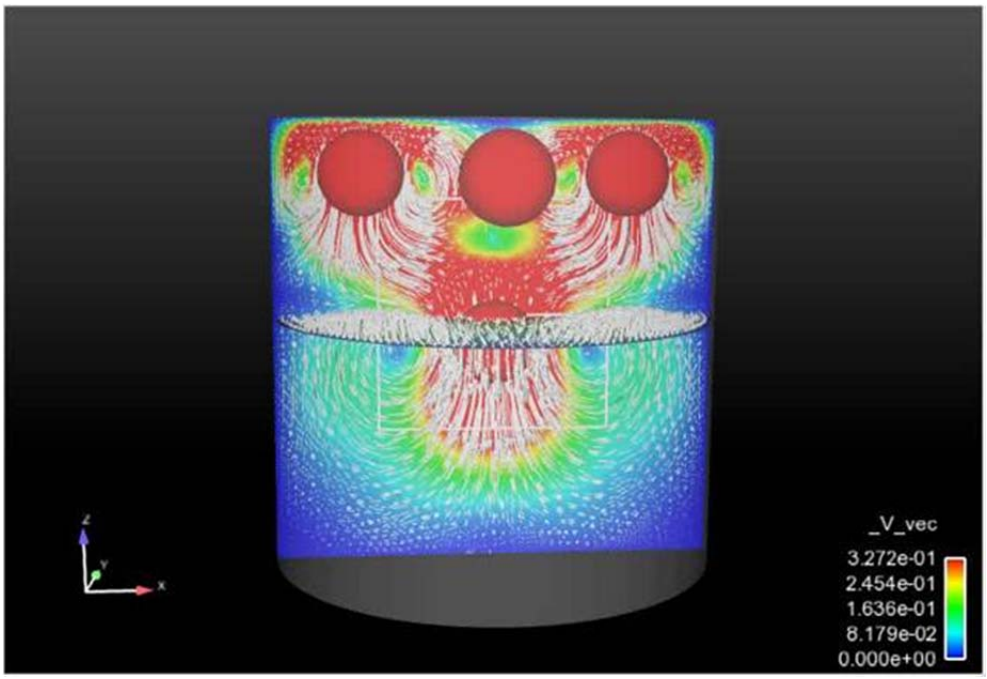

Figure 27: Four spherical particles settling in a cylindrical container.

We are currently working to extend the method to many more particles for problems such as mixing of powders into fluids.

3.2 Simulation of Droplet Formation in a Microfluidic Droplet Generator

The microfluidic droplet generator is a device designed to produce large quantities of uniformly-sized droplets within a carrier liquid. A typical droplet generator geometry (illustrated in Figure 28) consists of an intersection of three liquid streams that pass through a constriction.

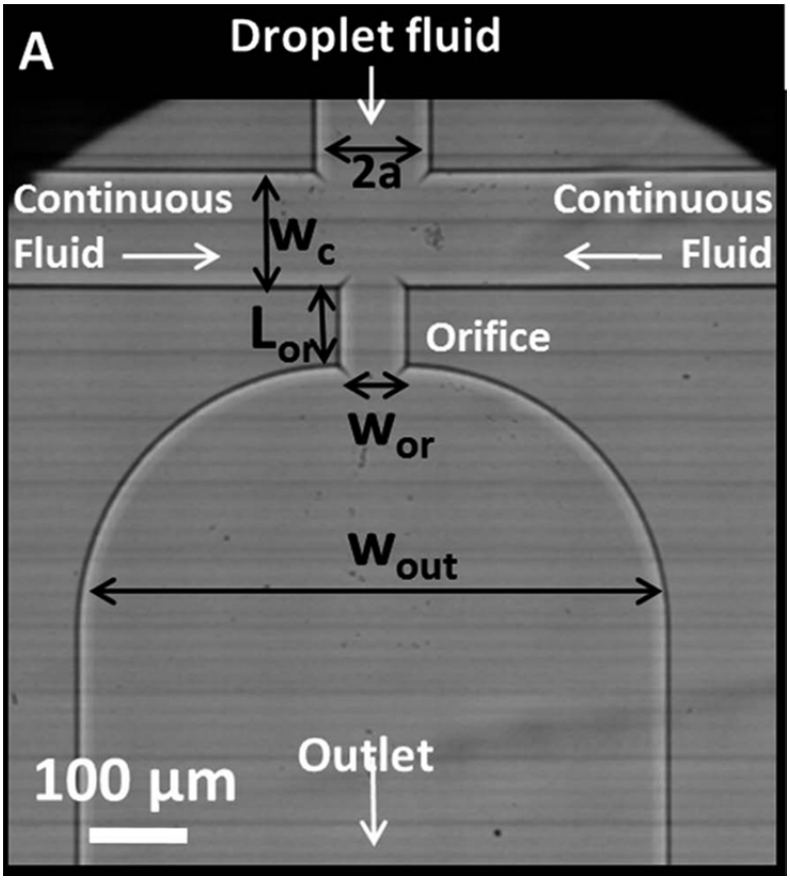

Figure 28. Microfluidic experiment from Chapter 3 and Robert et al., 2012.

By varying the geometry, liquid properties, and liquid flow rates, droplets of various sizes can be produced. The generator was simulated using the CDFEM. This technique allows for the definition of interface properties and captures physical properties that are not continuous across the interface (e.g. pressure when surface tension is nonzero). A more in depth discussion of CDFEM is provided in the previous section.

3.2.1 2D Simulations

To get started with the microfluidic simulations, we began with a 2D approach where we only looked at the flow in plane. This was to allow us to debug the input decks and get started with the simulations. The results look surprisingly similar to the experimental work discussed in the following.

The system we worked to model had dodecane as the droplet phase with a density 0.74 g/cm^3 and a kinematic viscosity of 1.8 cSt. To make drops, the flow rate was 0.01 ml/hr. The continuous phase was water with a density of 1.0 g/cm^3 and a kinematic viscosity of 1.0 cSt. The water flow rate was 0.5 ml/hr. The surface tension between water and dodecane was measured to be 52 mN/m. The dimensions of the microfluidic chip are:

2a = 200 microns

W_c = 200 microns
L_{or} = 110 microns
W_{or} = 120 microns
W_{out} = 500 microns

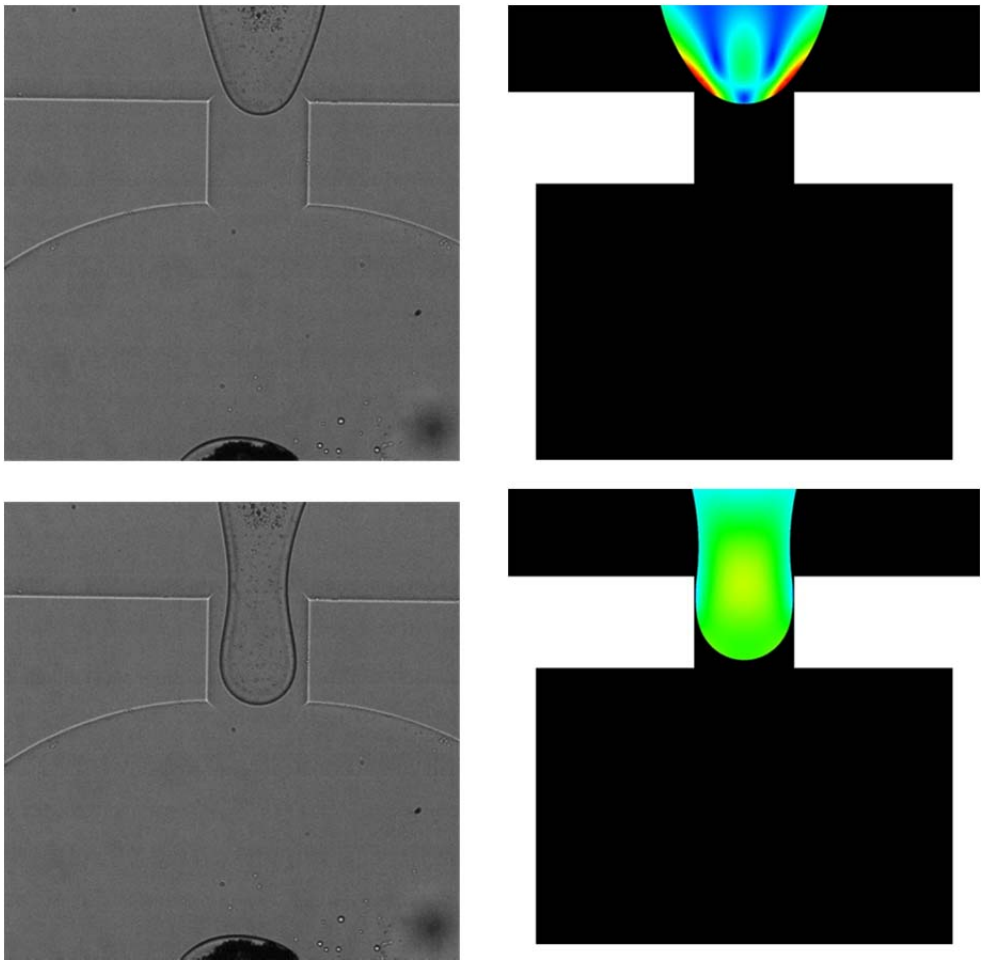

Figure 29. Droplet generator for two different flow rates. Experiments are on the left and simulations on the right.

We can examine the drop as it forms and then view it as the dodecane starts to neck and release the drop.

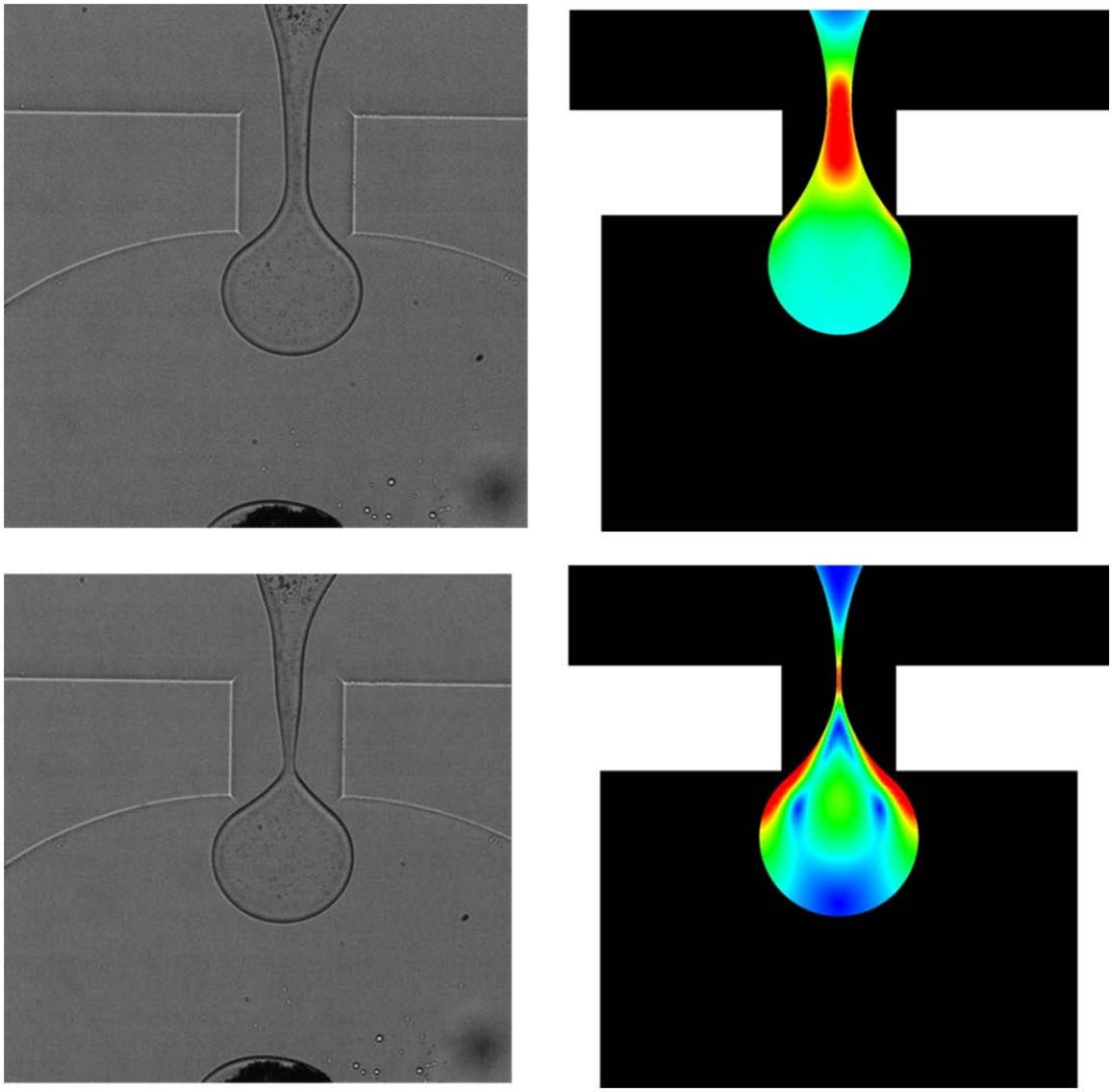

Figure 30. The stream necks as the drop is released from the microfluidic droplet generator. Two different flow rates are shown. The left shows the experiments, the right is the simulations.

Again, given that these simulations are missing a dimension and are therefore physically unrealistic, we are surprised at how similar the simulations are to the experiments implying that in-plane surface tension and flow may be important to the dynamics of droplet breakup in the microfocusing device.

3.2.2 3D Simulations

We have also investigated 3D CDFEM simulations of the microfocusing device as shown in Figure 31. Compared to the 2D simulations presented in the previous chapter, this simulation becomes much more complex due to a number of factors. This includes applying the appropriate boundary conditions on the top and bottom plate, where it is essential to apply a Navier slip

condition, instead of no slip, so the drop does not get trapped in the device. Adequate mesh refinement is also much easier to achieve in 2D than 3D and without this mass loss becomes more of an issue.

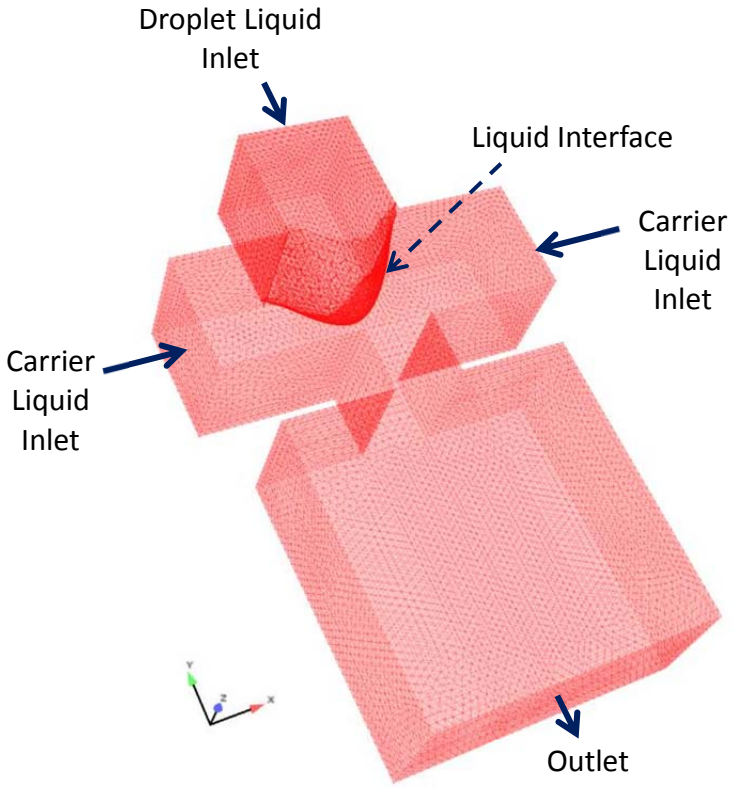

Figure 31: Microfluidic droplet generator geometry used for simulation including the mesh.

Initially, the interface of the droplet fluid slowly creeps down the channel. As it approaches the constriction, the velocity increases and a long strand of liquid is formed. The strand narrows and breaks resulting in a droplet. The droplet then flows down the channel entrained in the carrier liquid. An in-plane slice is shown in Figure 32.

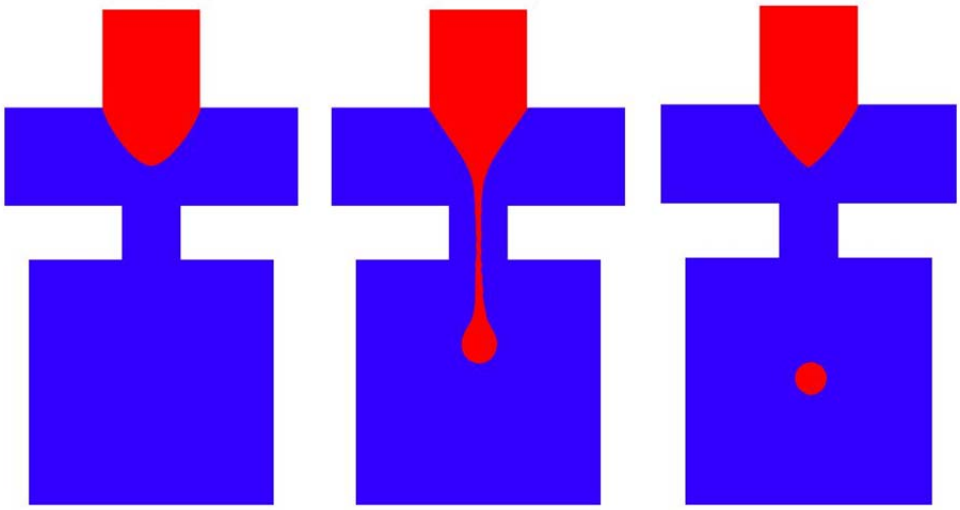

Figure 32. Cross section of the droplet formation process in the droplet generator. The first time plane is on the left.

Figure 34 illustrates the same simulation in three dimensions. In this figure, the pinching of the liquid strand is apparent in both the x and z directions. Since the simulation is performed in three dimensions, the breaking of the liquid strand is a physical phenomenon as opposed to a numerical phenomenon that would occur in a simulation with only two dimensions.

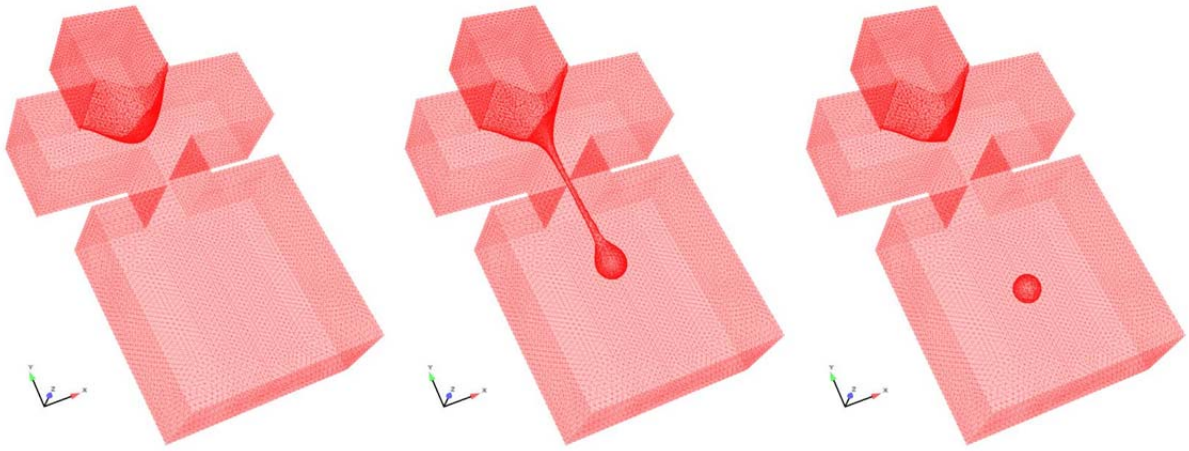

Figure 33. Droplet generation in three dimensions. The first time plane is on the left.

Overall, this simulation illustrates complex flow phenomena (droplet formation) between two immiscible liquids in a microfluidic device. The purpose of this simulation was to evaluate new capabilities within Aria (CDFEM) and qualitatively compare the results with the droplet generator experiments described elsewhere in this report. This new Aria capability was able to successfully capture the behavior of the microfluidic droplet generator for large capillary number scenarios. Future work will focus on making the CDFEM capability in Aria more robust and able to handle the more challenging case of small capillary number flows, which are more

relevant to the actual process. Additionally, mass transfer will be included to simulate the rate of mass transfer between the two liquids.

3.3 Confined Droplet in a Rectangular Channel

We have examined the flow of a large drop (with low capillary number) generated from the microfluidic device discussed in the previous section using CDFEM. This drop is larger than the channel depth and will move down the channel with the outer flow, but at a net velocity much slower than the maximum channel velocity, due to its large size. To simplify the simulation, we do not capture the breakup of the drop from the orifice. Instead, the drop is initialized as a cylinder, so the necessary volume is there but the material does not touch the walls, and then allowed to reach its pseudo-steady-state shape. This allows us to examine the short-time transient response of the drop relaxing to its final shape, including oscillatory behavior. Here we start with a drop that would be 1.2 times the channel depth if it were spherical. Results showing drop shape as a function of time are given in Figure 34.

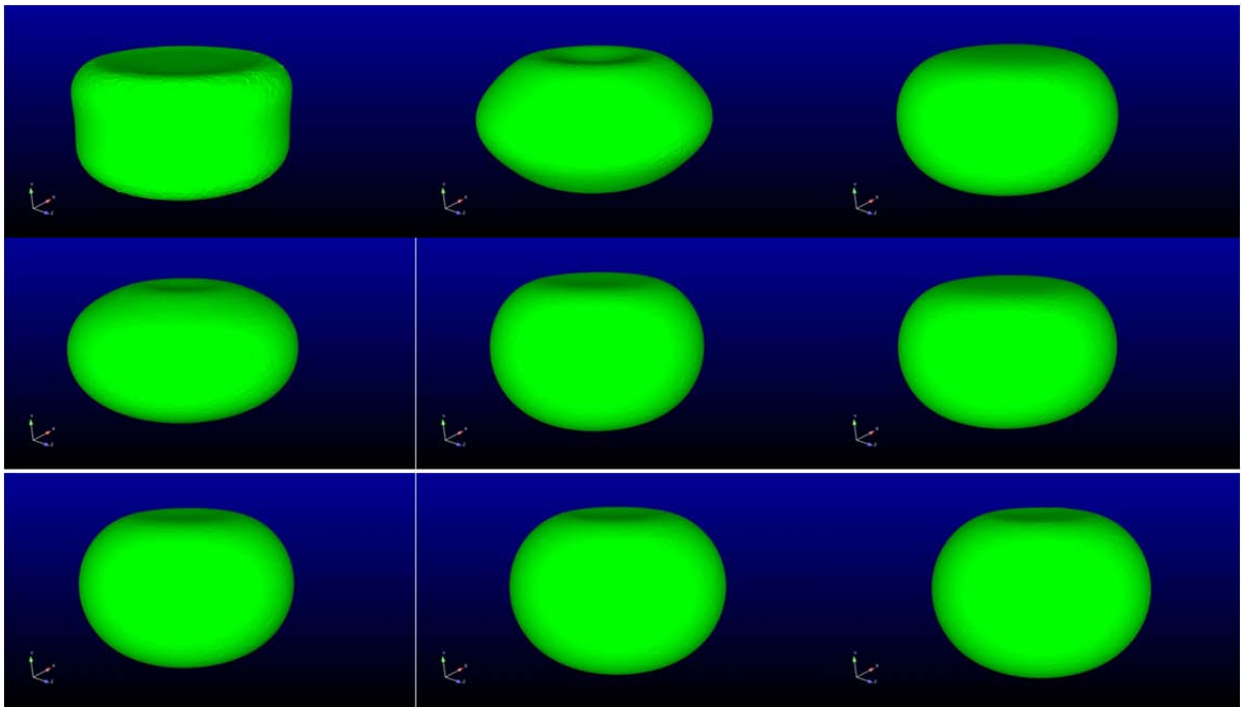

Figure 34. 3D Simulation of a confined droplet in between rectangular plates. Drop radius is 1.2 times the gap width if it was a sphere and initialized as a cylinder.

At early times, the drop is released and begins to flow downstream. The initial cylindrical shape becomes smooth, due to surface tension and flow, creating an elastic instability that damps out quickly. At later times, a capsule shape is achieved and the drop advects downstream. Figure 35 shows the velocity profile inside the drop once it has achieved its final shape.

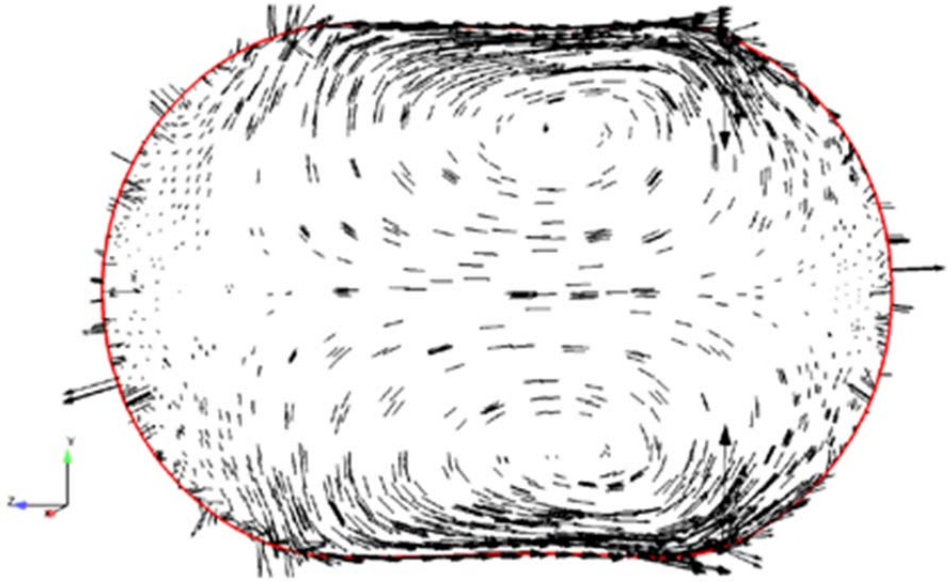

Figure 35. Velocity profile inside the confined drop. Here the velocity is shown in the reference frame of the drop. Qualitatively, the results look similar to the experiment but are noisy possibly due to parasitic currents.

From this figure, we can see the recirculation of the fluid inside the drop and the sharp gradients near the top and bottom plate. In addition, we can see that the velocity vectors are noisy due to parasitic currents created by the numerical discretization of surface tension.

3.4 Bottle Filling using CDFEM

One of our application areas of interest at Sandia is in mold filling and bottle filling, where fluids with non-Newtonian rheology are injected into molds with complex geometries. To this end, we examined how well CDFEM would perform for filling of a bottle with a complex shape. Figure show results for bottle-filling of a Carreau fluid.

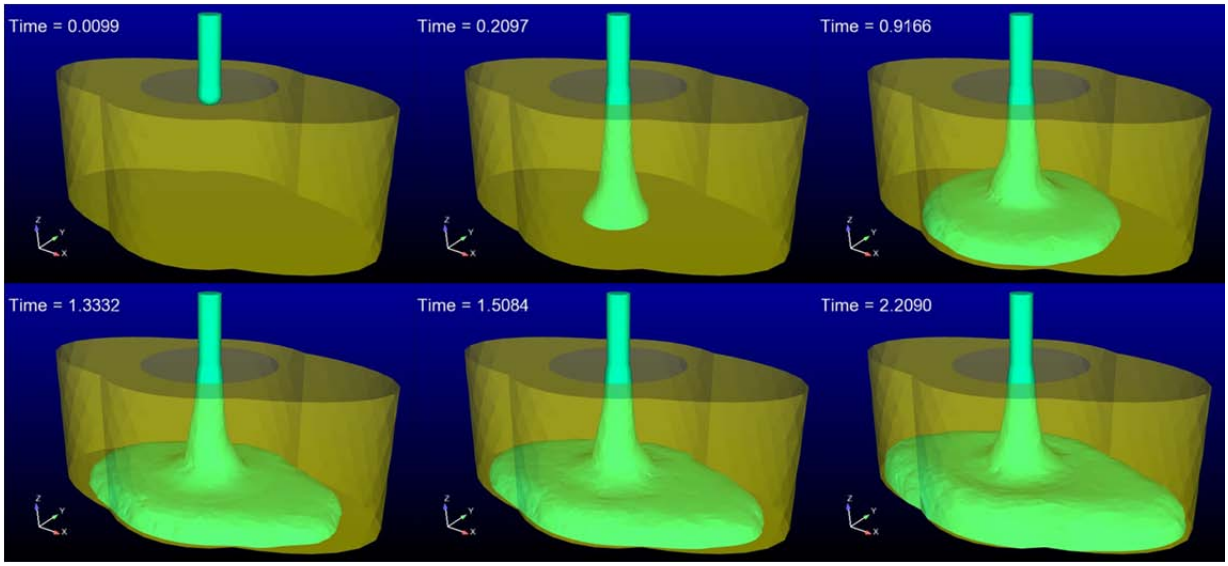

Figure 36: Bottle filling of a non-Newtonian fluid using a Carreau model and the CDFEM free surface algorithm

CDFEM is able to capture the buckling instability that occurs at early times as well as capturing the complex flow behavior as the fluid hits the bottom of the container and spreads. Thus, we forecast that CDFEM will perform well for problems such as mold and bottle filling, where surface tension is less important than microfluidics. This may be an area to focus on for the future.

3.4.1 Conclusions

We have used the CDFEM algorithm for several problems in capillary hydrodynamics. We have shown good results, but still have issues with mass loss and spurious currents for problems with low capillary numbers. The algorithm works better for moderate capillary number flow such as mold filling of foams.

4 MICROFLUIDIC EXPERIMENTS

As discussed in chapter 1, all mass transfer in a centrifugal contactor occurs at the interface between the droplet phase and the continuous phase. Thus, understanding the nuances of mass transport at the droplet scale in a detailed sense can help us build full-scale models of contactors. To this end, we focused on single drop experiments in a microfluidic device first to understand the drop making process and then to understand the mass transport. Three journal articles arose from this work. The first one on droplet generation on wetting and non-wetting surfaces was published in Laboratory on a Chip [Roberts et al., 2012A], the second paper on the detailed fluid dynamics at the droplet-scale examined with experiments and finite element simulations will be submitted to Physics of Fluids [Roberts et al., 2012B], and the third on mass transport, using the microfluidic device and scaled-up to the centrifugal contactor will be submitted to Chemical Engineering Science [Roberts et al., 2012C]. The mass transport in the contactor is discussed in the contactor experimental chapter, while the base neodymium mass transport in the microfluidic device is summarized here.

4.1 Droplet Generator

A thin flow-focusing microfluidic channel was first evaluated for generating monodisperse liquid droplets. In a flow-focusing channel, a liquid stream, jacketed by a second, co-flowing immiscible liquid becomes unstable as it passes through a constricting orifice (Figure 29). Droplet sizes range from the orifice size to a fraction of the orifice size, and can be controlled by altering flow conditions. [Anna, Bontoux, and Stone, 2003; Nie et al. 2008; Tan et al, 2008; Tan, Cristini and Lee, 2006] Typically, produced emulsions can have droplet size poly-dispersities less than 5%. Thin channels were of interest specifically for producing a more two-dimensional flow field that could be more easily imaged.

The production of both oil in water and water in oil emulsions were studied in a thin channel microfluidic chip. The microfluidic device was used in its native state, which is hydrophilic, or treated with octadecyltrichlorosilane (OTS) to make it hydrophobic. Having both hydrophilic and hydrophobic surfaces allowed for a large parameter study of viscosity ratios (droplet fluid/continuous fluid ranging from 0.05 to 96 and flow rate ratios (droplet fluid/continuous fluid) ranging from 0.01 to 2 in one geometry.

Figure 37 shows the production of droplets using a variety of flow rates, orifice sizes, and fluids. Here, a high speed camera was used to capture various stages of drop breakup. The appearance of the breakup is qualitatively comparable to two and three dimensional finite element simulations discussed previously in Chapter 3.

The hydrophilic chip provided a partially-wetting surface (contact angle less than 90°) for the inner fluid. This surface, combined with the unusually thin channel height, promotes a flow regime normally not observed in flow focusing devices where the inner fluid wets the top and bottom of the channel in the orifice and a stable jet was formed. Through confocal microscopy, this fluid stabilization was shown to be highly influenced by the contact angle of the liquids in the channel. Non-wetting jets undergo breakup and produce jets when the jet is comparable to or

smaller than the channel thickness. In contrast, partially-wetting jets undergo breakup only when they are much smaller than the channel thickness.

Drop sizes were found to scale with a modified capillary number based on the total flow rate, regardless of wetting behavior. The modified capillary number used the reciprocal-averaged viscosity of the two fluids. By defining the capillary number in this way, both oil-in-water and water-in-oil droplet sizes were found to collapse onto one common relationship. The effectiveness of this new capillary number indicates that both fluids are important to defining the stress balance in the orifice during the necking of the droplet fluid.

Although thin (25μm) flow-focusing devices were shown to produce monodisperse droplets of predictable size, the droplets tended to become stuck in the channel when the droplet diameter was much larger than the channel thickness. Therefore, a conventional flow-focusing device (100 μm thick) was used for mass transfer and flow experiments.

A more detailed description of the work that is summarized here was published in *Lab on a Chip* [Roberts et al. 2012A]. Since we have a journal article on the subject, here we will just summarize the results.

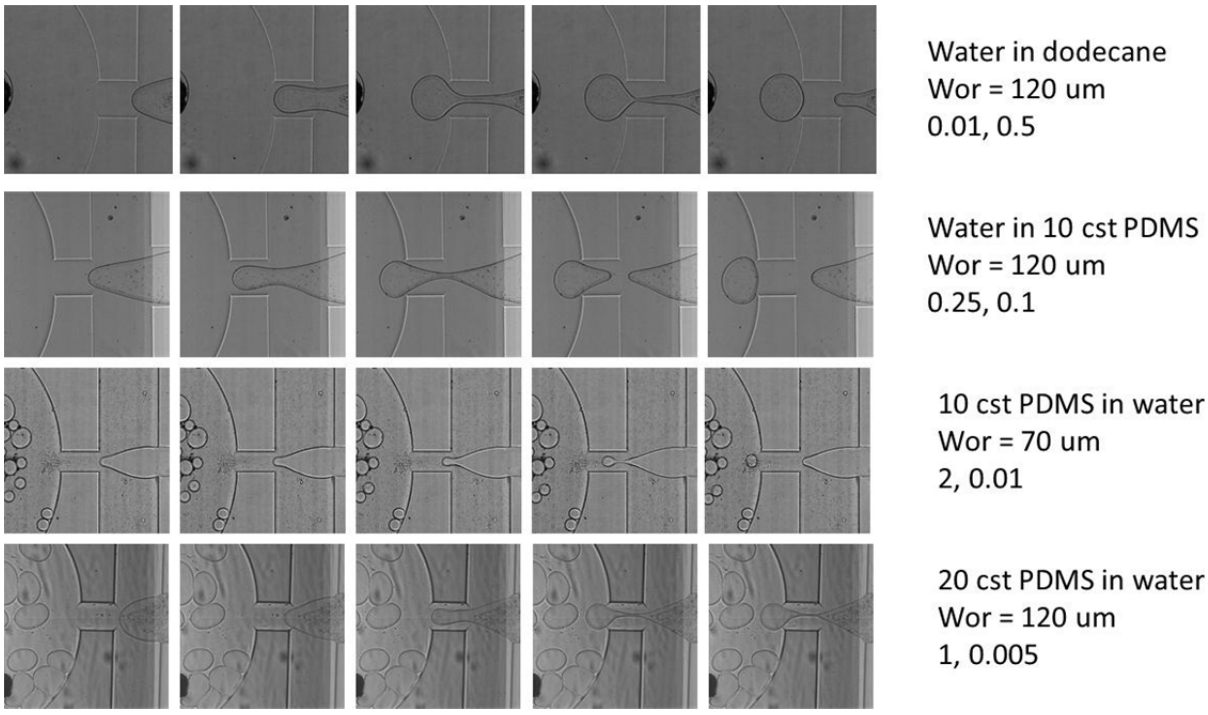

Figure 37. Production of oil-in-water and water-in-oil emulsions in a flow-focusing microfluidic device. The orifice width (W_{or}) as well as the flow rates of the inner and outer fluids (in mL/hr) is defined for each case.

4.2 Droplet dynamics

This is the summary of a paper which will soon be submitted to Physics of Fluids [Roberts et al., 2012B]. The PI has a copy of the entire submitted article.

4.2.1 Background

Mass transfer in a liquid-liquid extraction system is driven by both convection and diffusion. Therefore, it is important to fully characterize the flow inside and outside of the droplets at various flow rates and with varying droplet sizes.

In the case of droplets moving in Poiseuille flow, circulation within the drop is driven by a mismatch between the velocity of the droplet and the velocity of the continuous fluid. Nadim and Stone [1991] and others modeled the velocity of a drop in Poiseuille flow for droplet diameters less than the channel depth [Chan and Leal, 1979; Nadim and Stone, 1991; Hudson, 2009]. A small droplet moving along the centerline of the channel has a velocity that approximately matches the maximum velocity of the continuous fluid. As the droplet grows, it is influenced by a greater cross section of the flow, including the slower fluid near the walls. The large droplet therefore moves more slowly than the continuous fluid at the centerline of the channel. Thus, a large droplet in Poiseuille flow experiences shear from the faster moving continuous fluid at the centerline of the channel, and also shear imposed by both channel walls. This drives a circulation pattern within the drop.

The expected pattern of flow inside of a small droplet moving in a rectangular channel has been modeled [Nadim and Stone, 1991; Hudson, 2009]. Two pairs of vortices are expected. The first is driven by the drag of the top and bottom of the channel. In the reference frame of the droplet, the channel moves opposite the droplet motion, dragging the aqueous fluid with it. Conservation of mass dictates that this fluid must return to the front of the droplet in a path down the droplet center towards the front of the drop. This creates a fountain flow appearance in the vertical zx plane (see Figure 41).

If the channel geometry is a wide Hele Shaw slit, simulations predict that vortexes are only apparent in the vertical zx plane. However, in a unique case, Lee et al. observed recirculation patterns in a droplet containing surfactant that was anchored to be stationary in a Hele-Shaw cell [Lee, Gallaire, and Baroud, 2012]. In this case, they observed a vortex in the horizontal xy plane that scaled linearly with the velocity of the continuous liquid. This vortex is driven by the continuous fluid flowing around the outside of the drop. A horizontal xy plate vortex is also apparent if the channel cross section is square, due to the drag from the side walls. Researchers have used particle image velocimetry and other methods to image the described pattern in the specialized case of slug flow, where the droplet completely fills the channel [King, Walsh, and Grimes, 2007; Kashid et al., 2011; Fries and von Rohr, 2009; Sarrazin et al., 2008]. Simulations of confined cases have also been performed [King, Walsh, and Grimes, 2007; Kashid *et al.*, 2011; Fries and von Rohr, 2009; Sarrazin *et al.*, 2008].

When accurate fluid flow models are available for droplets in a channel, it has been shown that microfluidic devices can be used to characterize parameters in liquid-liquid systems. For

example, microfluidic devices have been used to probe the effects of surfactant on droplet interfaces by observing the interior flow to the droplet [Hudson et al. 2005; Schwalbe 2011]. Information pertaining to the slip at the liquid-liquid interface and Marangoni stresses can be elucidated.

Using the flow-focusing channel geometry that was chosen for mass transport studies, drops are produced that have large diameters with respect to the channel depth. In certain cases, the droplets overfill the channel, with diameters that are larger than the channel depth. Therefore, it is important to understand the expected velocity of such droplets in the channel, as well as the fluid circulation pattern that is driven in the droplet fluid. In this section, these parameters are measured for various flow rates and droplet sizes. A finite element ALE model is also produced in order to understand the flow inside and outside of the droplet. Finally, surface active tri-n-butyl phosphate (TBP) is added to the continuous fluid in order to determine whether it affects the flow within the droplet in a measurable way.

4.2.2 Experimental Methods

4.2.2.1 Drop production and flow visualization

Homogeneous droplets were produced in a flow-focusing microfluidic device shown in Figure 1. Glass chips were purchased from Translume (Ann Arbor, MI), and were made hydrophobic using a 2 vol% octadecyltrichlorosilane (OTS) (Sigma-Aldrich, St. Louis, MO, > 90% pure) in hexadecane (Sigma-Aldrich, St. Louis, MO, >90%) wash. Chip orifice widths were 50 μm and 100 μm, and the chip depth was always 100 μm.

In droplet flow visualization experiments, the droplet fluid is water that is purified using a Milli-Q purification system. A small amount (0.015 vol%) of 1 μm diameter red polystyrene particles (Fluoro-max, Thermo Scientific, Waltham, MA) are added as tracer particles. The continuous fluid is dodecane (Sigma-Aldrich, St. Louis, MO, >99% pure). Flow rates are specified using syringe pumps (Harvard Apparatus, PhD 22/2000, Holliston, MA), which were calibrated gravimetrically using a balance (Mettler Toledo, XS1003S, Columbus, OH). Droplet production in a similar system was discussed previously, including control of size and frequency of droplets [Roberts et al. 2012].

Flow is visualized using an inverted microscope (Leica DM IRB, Germany), and recorded using a high speed CCD camera (Phantom v 9.1, Vision Research, Wayne, NJ), with frame rates as high as 5000 frames per second. Distances are calibrated using Klarmann Rulings, Inc (Litchfield, NH) KR-868 reticules. Trajectories of the tracer particles are inferred using a particle tracking routine adapted by Blair and Dufresne for MATLAB [Blair and Dufresne, 2008]. Using this setup and technique, two-dimensional flow in a 15 μm thick horizontal plane of the chip can be visualized. By changing the focal plane, a picture of the three-dimensional flow can be created.

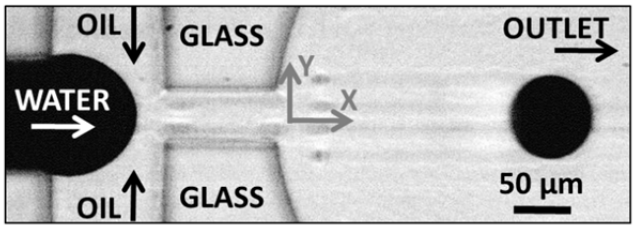

Figure 38. Flow focusing geometry, showing aqueous drops (dark) being produced in dodecane. Orifice sizes are 50 µm and 100 µm, with all other dimensions being equal. The channel depth is 100 µm

4.2.2.2 Finite Element Model

Two-phase flow of droplets in a rectangular channel is simulated using an arbitrary Lagrangian-Eulerian (ALE) method in Sierra/Aria [Notz et al., 2007]. A pressure gradient is applied down the channel, causing a Poiseuille flow to set up through the channel, moving the drop. In order to simulate a moving drop using an ALE method without significant mesh deformation, a change-of-reference is necessary. We would like to work in the reference frame of the drop, such that the drop is stationary and the walls move backwards.

An Aria user plugin was written to implement a proportional–integral–derivative (PID) controller that measures the drop velocity and displacement, and then calculates the wall velocity that is necessary to keep the drop stationary. This controller leads to the oscillatory behavior seen in Figure 39 and requires tuning parameters for expedient convergence. Standard control theory is used to set these parameters.

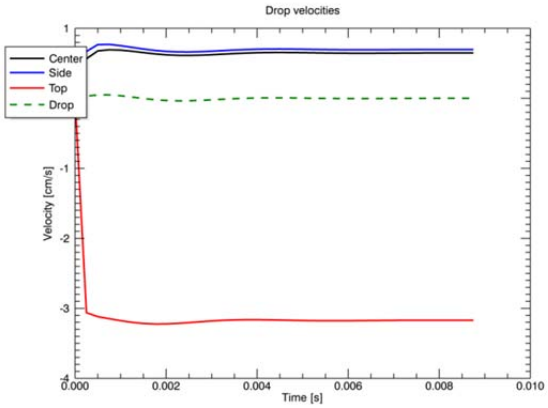

Figure 39: Example transient simulation of a drop flowing down a channel. The drop diameter is 90% of the channel depth.

4.2.3 Droplet Velocity

Using particle tracking, the continuous fluid streamlines were confirmed to be consistent with Poiseuille flow through a rectangular channel [White, 1991]. Experimentally observed droplet

velocities matched the Nadim and Stone [1991] predictions well for droplet diameters ranging from 0.5-0.8 times the channel height (Figure 40).

Because the Nadim and Stone [1991] solution is a simple asymptotic solution that neglects any wall effects or any deviations from spherical of the drop, it does not accurately predict the velocity of large droplets in rectangular channels. Therefore, a full ALE finite element model was created in Aria/Sierra to model the droplet motion as well as the circulation within the drop. Since the FEM solution does capture the flow of the continuous fluid between the drop and the wall as the drops get large, it was more accurate in predicting the drop velocities for larger drops up to diameter to height ratios of 97% (Figure 40).

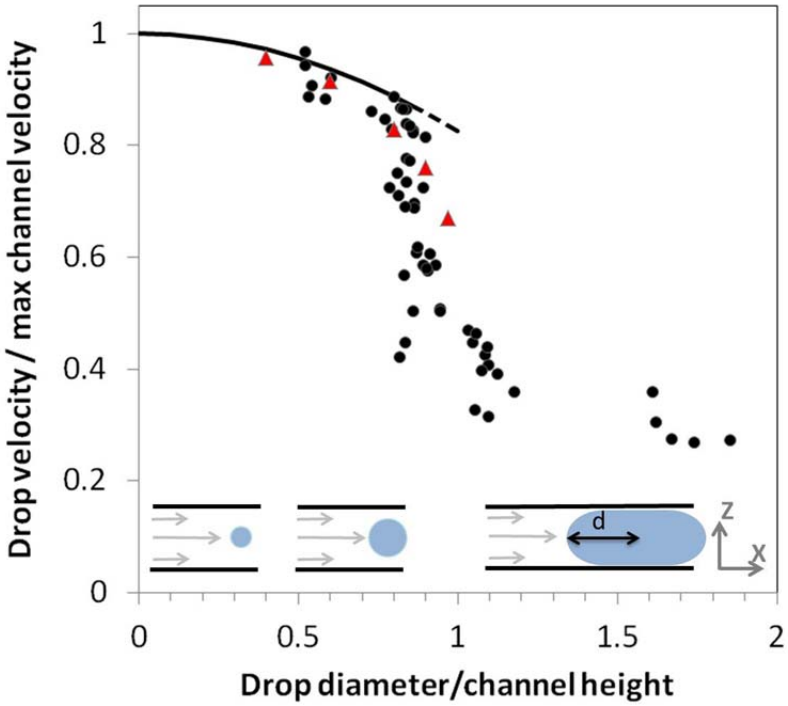

Figure 40: Normalized drop velocity in Poiseuille flow with respect to normalized droplet size, d/h. Symbols correspond to experimental observations (.), Nadim and Stone model (--), and ALE FEM simulation (Δ).

Droplets were also experimentally made which fill or overfill the channel. In this case, only a small lubrication layer of continuous fluid separates the drop from the channel walls, creating substantial drag on the droplet. Figure 40 shows how this additional drag drastically slows droplets with diameters equal to or greater than the channel height. When the droplet diameters are 1.5 – 2 times the channel height, the velocity asymptotes to a value that is approximately half of the average continuous fluid velocity.

4.2.4 Droplet Circulation

Because the continuous fluid is faster than the drop and the drop is also being sheared by the walls of the channel, a circulation pattern develops within the drop. This circulation pattern was modeled using ALE FEM for water drops in dodecane and is shown in Figure 41. The expected fountain flow circulation pattern modeled by others for a droplet in a Hele Shaw channel is found. Here, one pair of vortexes is evident in the x-z plane. This circulation pattern was predicted for drop diameters up to 97% of the channel depth by ALE FEM simulations and by other researchers for even larger droplets [Sarrazin et al., 2008]. The Poiseuille flow in the outer fluid is also perturbed by the drop. Because the flow is constricted near the wall and also around the drop sides, the outer fluid velocity increases to flow around the drop.

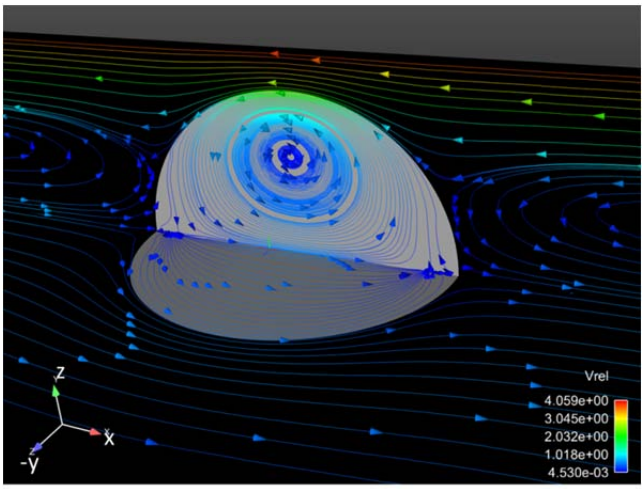

Figure 41: Streamlines for the final steady state of an ALE FEM simulation for a water drop in dodecane. The drop diameter is 80% of the channel depth, and the velocities are drawn relative to the net drop velocity. Both x-y and x-z planes are drawn.

The experimental setup allows only motion in the x-y plane to be imaged. When the droplets are small ($d/h \approx 0.5$), the expected circulation pattern is observed, where all streamlines flow towards the front of the drop. The velocity of this fluid is less than is predicted through simulations, perhaps because of slip at the liquid-liquid interface due to surfactant introduced with the latex particles used to track the fluid. Unfortunately, the liquid-liquid interface interferes with the visualization of the particles at the edges of the drop in order to verify that this slip exists. The thickness of this interference varies with the focal plane.

When the drops become larger than 0.6 times the channel depth, a vortex is observed in the x-y horizontal plane. Figure 42 shows streamlines in three different planes ranging from near the wall to the center in the reference frame of the drop. Close to the wall, streamlines are dominated by shear from the top of the channel and all tracer particles move opposite the direction of the drop movement. In the plane near the droplet center, the continuous fluid is much faster than the drop. This fluid drags the droplet fluid at the liquid-liquid interface

forward, in the direction of the droplet motion. The fluid returns down the droplet center. The three-dimensional fountain flow is drawn in a schematic in Figure 43.

Because the observed droplets have large diameters with respect to the chip depth they move slowly and the continuous fluid exerts a more substantial shear on the droplet, approaching the anchored drop case of Lee et al. [2012]. In fact, in most of the cases that were investigated, the difference between the drop speed (V_d) and the maximum speed of the continuous fluid (V_{max}) was greater than the difference between the drop speed and the wall (0). Therefore, it is unsurprising that a vortex is imaged in the x-y plane, the plane that experiences the greatest shear. The consequence is that in large droplets the x-y plane does experience a fountain flow, and the direction of the flow at the drop center is towards the back instead of the front of the drop. If there is a vertical plane vortex, its existence cannot be determined using the current experimental setup.

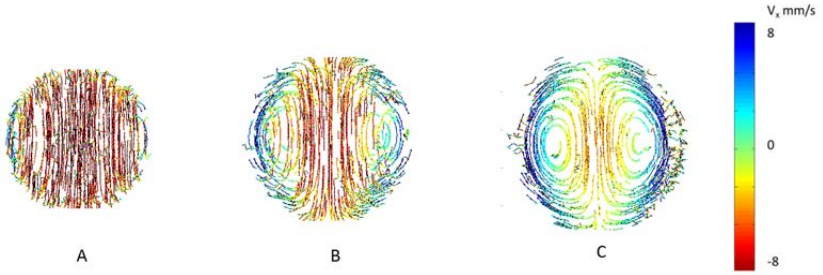

Figure 42: Streamlines within the drop A) at the wall, B) halfway between the wall and the droplet center C) near the droplet center. Color indicates the velocity of the streamline in the x direction. Streamlines are drawn with respect to the reference of the drop center in the xy plane. Drops are 0.6 mm in diameter with h/d=0.6.

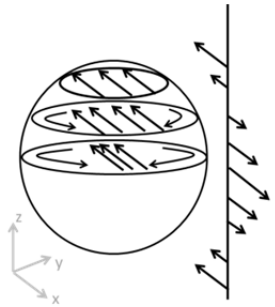

Figure 43: Three dimensional schematic of observed flow in large droplets and in the continuous fluid, drawn in reference plane of drop

The strength of the xy circulation can be described by the mean centerline velocity (V_c) in a plane near the droplet center. The centerline velocity is plotted with respect to the maximum velocity of the continuous fluid in Figure 44. Both velocities are measured with respect to the drop. There is a linear relationship between these two quantities, confirming that the horizontal vortex pattern is driven by shear from the faster moving continuous fluid. Scatter in the data is

due to inaccuracies in locating the exact center of the drop, as well as from capturing particles throughout the entire thickness of the finite focal plane.

Circulation patterns were measured for aqueous droplets in dodecane and also aqueous droplets in dodecane containing 0.1 M TBP and 0.2 M HTTA. The droplet size was approximately 0.8 mm, and the continuous fluid was 2 and 4 mL/hr. The observed circulation velocities for the two cases are shown in Figure 44. No noticeable difference was seen in the droplet flow or droplet velocities, indicating that within the ability of the technique to measure their effects, TBP and HTTA are not substantially influencing the interface.

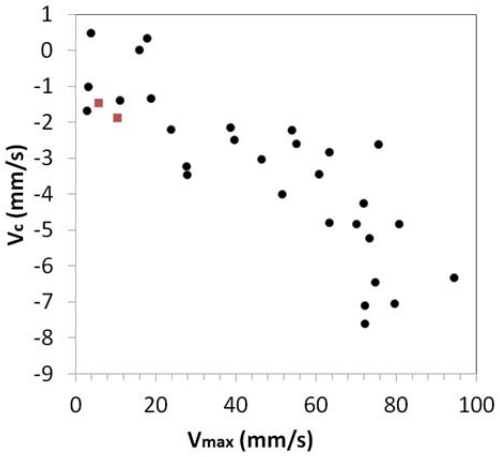

Figure 44: Observed X-Y circulation strength versus the relative velocity of the drop with respect to the maximum velocity in the channel. Cases containing 0.1 M TBP and 0.2 M HTTA are shown in red.

The presence of circulation will affect the relevant length scales for mass transfer. For mass transfer experiments, a drop diameter/channel depth ratio of 0.8 was targeted. Drops of this size are approximately spherical in the channel and possess strong x-y and z-x vortexes. This is an advantage, since in the presence of circulation, diffusion must occur across streamlines to the center of the vortex, whereas without circulation the relevant diffusion length is the longer drop radius. A larger droplet also moves slowly with respect to the continuous fluid, which suggests that the concentration of the continuous fluid is continuously renewed and will be approximately constant.

4.3 Liquid-Liquid Extraction in Microfluidic Devices

4.3.1 Background

Centrifugal contactors are used for specialized liquid-liquid extraction processes in the chemical, nuclear, and biotechnology industries. In nuclear waste reprocessing, they are uniquely suited for liquid-liquid extraction of uranium and plutonium isotopes from other rare earth elements using the TRUEX process. For example, because centrifugal contactors are comparatively small

relative to other liquid-liquid extraction unit operations there is less of a chance to achieve critical mass of radioactive material.

In a centrifugal contactor, two immiscible fluids are mixed at high speeds using a rotor, which creates a fine dispersion of droplets of one fluid in the other. High shear rates and large interfacial area between the two liquids creates an efficient environment for mass transfer of species from one fluid to another. The rotor also acts as a centrifuge, so that the oil and aqueous phases are separated from each other into two outlet streams.

Significant progress has been made to understand the centrifugal contactor through modeling Vedantam et al. 2012; Deshpande and Zimmerman 2006; Wardle and Lee, 2011] and laboratory scale experiments [Kadam et al. 2009; Calabrese, Wang, and Bryner 1986; C. Y. Wang and Calabrese 1986; Leonard et al. 1993; Cauwenberg, Degrève, and Slater 1997]. In order to fully understand such studies, however, fundamental parameters are necessary such as the droplet size and distribution, mass transfer coefficients, diffusion coefficients, and partition coefficients. Established methods exist for obtaining diffusion coefficients, for example by using a side-by-side diffusion cell [Sanni and Hutchison 1973; Chang and Wilke 1954]. Partition coefficients can also be measured with accuracy [Farbu, Alstad, and Augustson, 1974]. However, mass transfer greatly depends on mixing speeds, interfacial area, and the existence of boundary layers, making its measurement nontrivial. To obtain mass transfer coefficients that are relevant for the centrifugal contactor, it is best to use a model environment that also experiences high shear.

Microfluidic devices have proved useful for observing mass transfer quantitatively on a single drop basis [Nichols et al., 2011; Mary, Studer, and Tabeling, 2008; Xu et al. 2008; Kumemura and Korenaga, 2006]. Microfluidic devices are ideal model environments since they can produce high mixing speeds with known interfacial areas [Nichols et al., 2011]. Reliable production of monodisperse oil in water and water in oil droplets has been well documented for a variety of channel geometries [Cristini and Tan, 2004; Gunther and Jensen, 2006; Teh et al., 2008]. Unlike falling droplet experiments where motion is driven by gravity [Kronig and Brink, 1951; Johns and Beckmann, 1966], residence and reaction times for droplets in microfluidic channels are on the order of those observed for centrifugal contactors.

Here, a system that mimics the TRUEX liquid-liquid extraction process is studied for a laboratory scale contactor. Parameters including diffusion and distribution coefficients are obtained to better understand the contactor behavior. A flow focusing microfluidic channel is used to observe mass transfer and measure mass transfer coefficients on a single drop basis. Droplet size distributions have also been collected experimentally and are discussed elsewhere [Wyatt et al., 2012]. The effects of these parameters on the contactor experiments are discussed.

4.3.2 Experimental Methods

4.3.2.1 Diffusion Coefficients

Diffusion constants were measured in the aqueous and organic phases using a side-by-side diffusion cell (PermeGear, Hellertown, PA, model #5G-00-00-15-07) [(Sanni and Hutchison, 1973, Chang and Wilke, 1954]. In this technique, a membrane is placed between two 7mL glass cells. With both cells filled with solvent, a small volume of solvent is removed from one of the cells, which is then replaced with the same volume of a dilute solution of the solute of interest. The concentration in one of the cells (usually the unadulterated cell) is then monitored by continuous UV-VIS spectroscopy using an Ocean Optics spectrometer (QE6000) and a light source (Halogen Dolan Jenner, LED Dolan Jenner LMI-6000). Flow through the membrane is sensitive to pressure differences in the cells, thus the cells are left open for approximately an hour to equalize pressure and then gently taped closed with a piece of scotch tape to prevent evaporation. The membrane is calibrated by performing the measurement using a compound with a well-known diffusion constant. A calibration run was performed prior to and at the end of our measurement sequence to ensure that the membrane constant remained the same over time.

In the aqueous diffusion experiments an acrylic-nylon membrane (Gelman Pall Versapor-800, 0.8 μm, 47 mm diameter, PN 66401) was used to separate the two half cells. Rhodamine B (Sigma-Aldrich), 500μL of 13.4 μM was added to the 7mL half-cell as the membrane-calibration solute, as it has a strong absorption in the visible range at very low concentrations and its diffusion constant has been determined to be $4.2 \pm 0.3 \times 10^{-10}$ m^2/sec at pH 2 to 9.5, I < 0.1 M, and C < 10 μM (Gendron, et al. 2008). The solvent for the membrane-calibration was 0.008 M KHP buffer set to a pH of 5.75; the absorbance, diffusion, and complexation of Rhodamine B, Fluorescein and xylenol orange are sensitive to pH. As a calibration check we performed diffusion experiments using Fluorescein (Fluka), 500 μL of 400 μM added to the 7mL half-cell, in 0.008 M KHP buffer which gave results $3.9 \pm 0.6 \times 10^{-10}$ m^2/sec consistent with experiments by Perale et al. (2011) but below other literature values $4.2 – 6.4 \times 10^{-10}$ m^2/sec [Casalini, et al.,2011; Galambos, 1998]. With nearly all of the compounds of interest we observed anomalous absorbance trends over long periods of time (weeks), which we attribute to slow degradation of the organic dyes, and/or aggregation [Casalini, et al., 2011].

For the organic diffusion experiments, a Polytetrafluoroethylene (PFTE) membrane (Pall Zelfluor, 0.5 μm, 47 mm diameter, PN P5PQ047) with the cellulose backing material removed was used to separate the two half cells. Dimethyl yellow was used as the membrane-calibration solute [Yoo, et al., 2008; Park and Chang, 2000]. A 1500 μL aliquot of 100 μM dimethyl yellow was added to the high side cell, absorbance was taken at 416.91 nm.

4.3.2.2 Partition Coefficients

Partition coefficients were determined by placing volumes of the organic and aqueous phase in contact in bottles that were gently shaken on a shaker table for at least one hour. The aqueous phase was then separated and sampled by inductively coupled plasma atomic emission spectroscopy (ICP-OES) analysis. In the organic phase we combined dodecane (Sigma-Aldrich), HTTA (Sigma-Aldrich, St. Louis, MO), and TBP (Sigma-Aldrich). In the aqueous phase, we used two recipes corresponding to the chip experiments and the contactor experiments respectively.

4.3.2.3 Mass Transfer to Droplets

The extraction of neodymium (Nd^{3+}) from aqueous droplets to dodecane using the complexant thenoyltrifluoroacetone (HTTA, Sigma-Aldrich, St. Louis, MO) and ligand tri-n-butyl phosphate (TBP, Sigma-Aldrich, St. Louis, MO) was chosen as a model mass transfer system. This is a nonradioactive system that has behavior similar to uranium or plutonium extraction. The aqueous phase also included xylenol orange (XO, Sigma-Aldrich, St. Louis, MO) as an indicator for Nd^{3+}. The reaction was found for an analogous system using carbon tetrachloride as the organic phase to be as follows [Farbu, Alstad, and Augustson, 1974]:

$$Nd(XO)_{(aq)} + 3\ HTTA_{(o)} + 2\ TBP_{(o)} \leftrightarrow Nd(TTA)_3(TBP)_{2(o)} + 3\ H^+_{(aq)} + XO_{(aq)}$$

In all cases, the aqueous droplet fluid is 3.2 mM $NdNO_3$ (Sigma Aldrich, St. Louis, MO), 0.01 M xylenol orange, and is buffered at pH = 5.5 using 0.2M potassium hydrogen phthalate (KHP, Acros Organics, NJ). The continuous oil phase has varying concentrations of TBP and HTTA as specified. Solution concentrations are verified using inductively coupled plasma mass spectrometry.

Uncomplexed xylenol orange absorbs light at 430 nm, whereas the XO-Nd complex absorbs at 590 nm (Figure 45). Therefore, by illuminating the microfluidic chip only at 590 nm using a 70 mW LED (M590L2, Thor Labs, Newton, NJ), the intensity of the resulting image can be correlated with the XO-Nd concentration. Light intensity is captured using the Phantom camera at 2000 fps as well as a photodiode (APD110A, Thor Labs, Newton, NJ). The photodiode signal is recorded with a National Instruments multifunctional data acquisition device (NI-USB-6366) and LabVIEW Signal Express software at 10^{-6} Hz (National Instruments, Austin, TX). Calibration curves relating the light intensity to the XO-Nd complex concentration are created by imaging droplets of six different concentrations ranging from 0 – 3.2 mM Nd-XO through pure dodecane. Calibration curves are linear, with R^2 values of 0.986 (photodiode) and 0.995 (camera).

To obtain the change of concentration in a drop with time, images are taken throughout the length of the microfluidic chip. Image locations are known through use of a motorized stage (ProScan, Prior Scientific, Cambridge, UK). Droplet velocities and sizes are measured from the images obtained through the Phantom camera. The average concentration in the drops is reported using more than $2x10^6$ measurements using the photodiode (Figure 45). Figure 46 shows an example of mass transport in the flow-focusing device demonstrating the color change in the droplet as they move towards the exit.

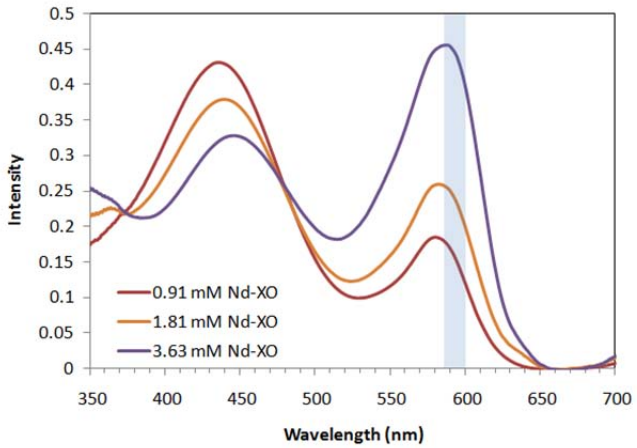

Figure 45: Light absorption by aqueous solutions of Nd^{3+}. Various amounts of Nd^{3+} have been complexed with xylenol orange. The microfluidic chip was illuminated with 590 nm light so that the intensity of the light passing through the channel was correlated with the Nd-XO concentration

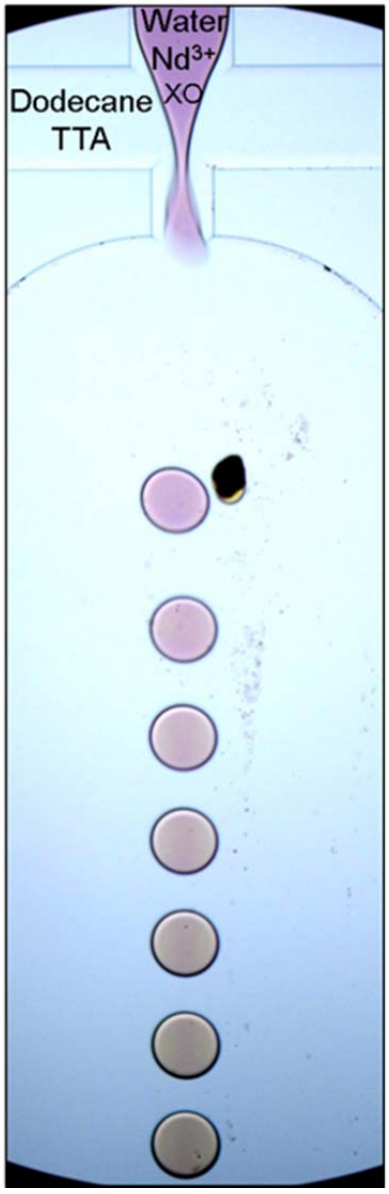

Figure 46. An example of droplet formation and mass transport in the microfocusing device showing the color change as the droplets move downstream.

4.3.3 Results and Discussion

4.3.3.1 Diffusion Coefficients

The diffusion coefficients in the aqueous phase are given below in Table 1. The diffusion constants for $Nd(XO)_{aq}$ and the H_3XO_{aq} were determined in 0.2 M KHP buffer. For the bare Nd^{3+} ion, this was not possible as Nd^{3+} tends to form a solid phase with KHP in the absence of

the XO complexant, hence a lower-concentration sodium-acetate buffer was used. The pH in these measurements matches the pH used in the mass-transport experiments.

Table 1: Aqueous Diffusion coefficients

Species	Medium	Diffusion Coefficient (m^2/s)
$Nd(XO)_{aq}$	0.2 M KHP Buffer at pH 5.5	$2.3 \pm 0.2 \times 10^{-10}$
H_3XO	0.2 M KHP Buffer at pH 5.5	$3.0 \pm 0.2 \times 10^{-10}$
Nd^{3+}	0.01M NaAc Buffer at pH 5.5	$7.0 \pm 0.7 \times 10^{-10}$

4.3.3.2 Partition Coefficients

Partition data is shown below in Table 2 for the microfluidic chip experimental concentrations. We also calculate a distribution value D as the total concentration of neodymium in the organic phase divided by the total concentration of neodymium in the aqueous phase. Note that this is not a true thermodynamic value, since most of the Nd remaining in the aqueous phase is complexed with xylenol orange.

Table 2. Partition data for the microfluidic-chip relevant experiments. Here the initial [Nd(XO)]aq = 3.2 mM, the xylenol orange concentration was 0.01 M and the matrix solution was 0.2 M KHP buffer pH = 5.45.

$[HTTA]_O$ initial (M)	$[TBP]_o$ initial (M)	$[Nd_T]_{aq}$ final (M)	$D = [Nd]o/[Nd_T]aq$
0.2	0.3	6.5×10^{-7}	4.8×10^{3}
0.2	0.3	5.7×10^{-7}	5.6×10^{3}
0.2	0.01	1.9×10^{-5}	1.7×10^{2}
0.2	0.01	1.9×10^{-5}	1.7×10^{2}
0.2	0.1	1.0×10^{-5}	3.0×10^{2}
0.004	0.0025	4.4×10^{-4}	6.2×10^{-1}
0.002	0.0025	1.4×10^{-3}	1.3×10^{-1}
0.002	0.01	7.1×10^{-4}	3.5×10^{-1}
0.002	0.005	8.6×10^{-4}	2.7×10^{-1}

4.3.3.3 Droplet Concentration and Mass Transfer Coefficients

The concentration of Nd-XO complex in the droplets was recorded as the droplets traveled down the chip outlet channel for various continuous fluid flow rates and TBP and HTTA concentration. All mass transfer experiments were performed for a droplet size/channel height ratio of 0.8 – 0.85.

When the HTTA concentration in the continuous phase was less than 0.004 M, the mass transfer at the droplet surface was slow compared to the diffusion of the species in the droplet. Assuming that the droplet is well mixed and the concentration of Nd^{3+} is constant in the outer fluid, a

simple mass transfer balance for the concentration of Nd^{3+}, *C*, at time *t* can be written for a droplet of surface area, *A*, and volume, *V*:

$$k_{eff} A(C - HC_{cont}) = -V \frac{dC}{dt} \tag{23}$$

Since the flow rate of continuous fluid is always greater than 100 times that of the droplet fluid, the quantity HC_{cont}, the partition coefficient times the Nd^{3+} concentration in the dodecane, is approximated to be zero. Upon integrating this equation and simplifying the area to volume ratio of a sphere, an expression for the effective mass transfer coefficient k_{eff} can be found:

$$k_{eff} = -\frac{3}{2} \ln(\frac{C}{C_i}) \frac{d}{t} \tag{23}$$

Here, C_i is the initial concentration of Nd^{3+} in a drop with diameter *d*. The effective mass transfer coefficient combines the mass transfer rate at the liquid-liquid interface as well as the mass transfer rate across any concentration gradients in the fluid.

Using this simplified model, k_{eff} was found for a range of TBP and HTTA concentrations. Figure 47 displays representative data for four separate cases. In all cases, a plot of $\ln(C/C_i)$ versus t/d was linear. Values of R^2 corresponding to the linear fit used to find k_{eff} are reported. The continuous fluid flow rate (Q_c) also did not impact the mass transfer rate. Both of these observations are consistent with a kinetically limited process. It was found that the mass transfer rate was first order with HTTA concentration and was only weakly dependent on the TBP concentration.

Also reported in Table 3 is the Reynolds number defined for the continuous fluid flow through the outlet channel with width *w*, $Re = \rho_c Q_c / w\mu_c$, showing that the flow is always laminar. The drop velocity V_d, and the relative velocity of the drop with respect to the maximum velocity of the fluid V_{rel} are also cited. The Peclet number, Pe, is defined for the drop as $Pe = V_{rel}\, d/(4D)$, where the diffusion coefficient for Nd-XO in the aqueous buffer solution, *D*, is that found previously using the Taylor diffusion cell. Here the length scale for diffusive transport is assumed to be ¼ of the drop diameter, *d*, or approximately the distance to the center of the vortex observed in Figure 42. The Peclet number is always on the order of 100, confirming that convection in the droplet is much faster than diffusion across streamlines.

The assumption that the droplets are well-mixed can be tested by calculating the mass transfer Biot number, defined as $Bi = k_{eff} d/4D$. The value of *Bi* for all cases is greater than one, indicating that the kinetic transport to the drop is slightly faster than the diffusive transport within the drop. The Biot number does not take into account effects of Taylor dispersion, which would increase the diffusion rate within the drop due to shear. Regardless, for rigorous determination of the mass transfer coefficient a mixed kinetic-diffusion model may be more appropriate.

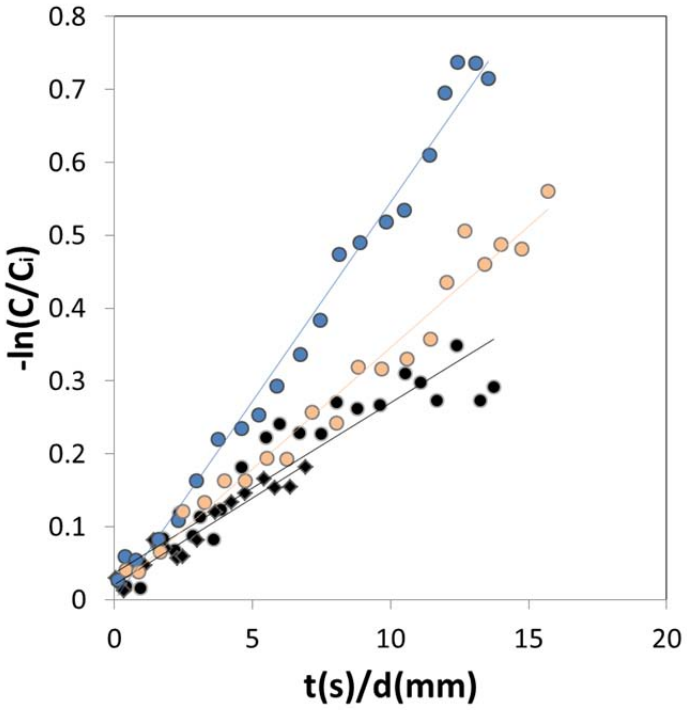

Figure 47: Concentration as a function of time for (●) 0.0025 M TBP, 0.002 M HTTA, Qc = 2 mL/hr; (♦) 0.0025 M TBP, 0.002 M HTTA, Qc = 2 mL/hr; (●) 0.0025 M TBP, 0.004 M HTTA, Qc = 2 mL/hr, (●) 0.005 M TBP, 0.002 M HTTA, Qc = 2 mL/hr.

Table 3: Parameters obtained for reaction limited mass transfer experiments

Continuous Fluid									
M TBP	M HTTA	Q_c (mL/hr)	V_d (mm/s)	V_{rel} (mm/s)	k_{eff} (mm/s)	R^2	Re	Pe	Bi
0.0025	0.002	2	15	-4.3	0.035	0.88	0.62	392	3.19
0.0025	0.002	4	33	-5.7	0.036	0.93	1.24	514	3.22
0.0025	0.004	2	16	-3.1	0.082	0.99	0.62	283	7.48
0.0025	0.004	4	34	-4.4	0.066	0.97	1.24	382	5.77
0.005	0.002	2	14	-5.1	0.050	0.97	0.62	465	4.56
0.005	0.002	4	31	-7.7	0.053	0.95	1.24	694	4.80
0.01	0.002	4	33	-5.6	0.048	0.93	1.24	505	4.29
0.01	0.002	2	15	-4.5	0.048	0.99	0.62	415	4.41

When the HTTA concentration is increased to 0.2 M in the dodecane, the kinetics at the drop interface become faster and the mass transfer clearly becomes diffusion limited. Figure 48 shows the fraction of Nd^{3+} extracted from a drop versus time, nondimensionalized by a characteristic time for diffusion, $\tau = 4Dt/d^2$. The mass transfer of all cases is equivalent, irrespective of the HTTA and TBP concentrations in the dodecane. For comparison, the Kronig-Brink solution for mass transfer from a perfectly circulating sphere translating through a

quiescent fluid is also included [Clift, Grace, and Weber, 1978; Kronig and Brink, 1951]. The Kronig-Brink solution assumes a perfectly symmetrical flow pattern within the drop, much like the square channel flow pattern described earlier. Since the Kronig-Brink solution contains more circulation than the observed flow, the observed mass transfer is slower.

The observation that the TBP concentration did not influence the mass transfer in the diffusion limited regime is more evidence that TBP does not affect the mobility of the liquid-liquid interface significantly. If TBP caused slip at the dodecane-water interface, the circulation pattern within the droplet would have been altered and the relevant diffusion length would have changed [Schwalbe et al., 2011]. Within the experimental capabilities, this was not observed.

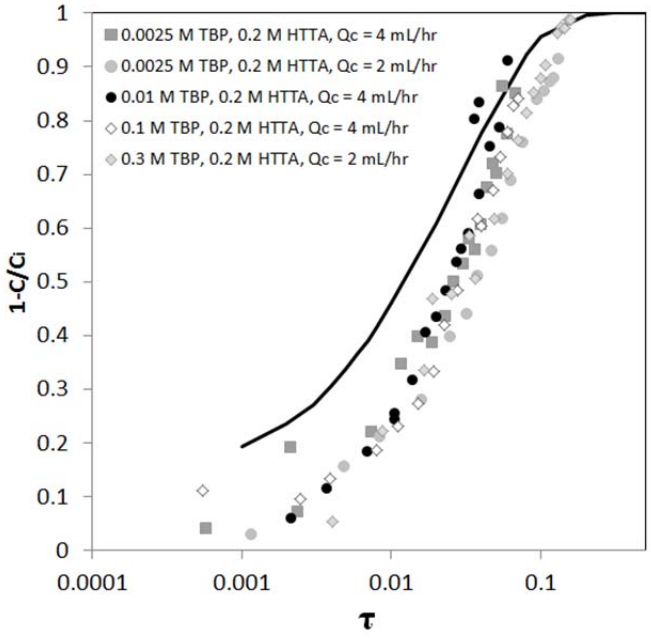

Figure 48: Fraction of Nd^{3+} transferred versus dimensionless time for diffusion limited experimental cases (symbols). The Kronig-Brink solution for a perfectly circulating sphere in plug flow is shown for comparison (--).

4.3.3.4 Coalescence and Mass Transport

Because of the versatility of our microfluidic chip, we are able to examine a number of flow regimes from single separate drops to drops that are formed close enough together to coalesce. In Figure 49, we show false color plots of mass transport in the thin (25 μm channel) microfocusing device.

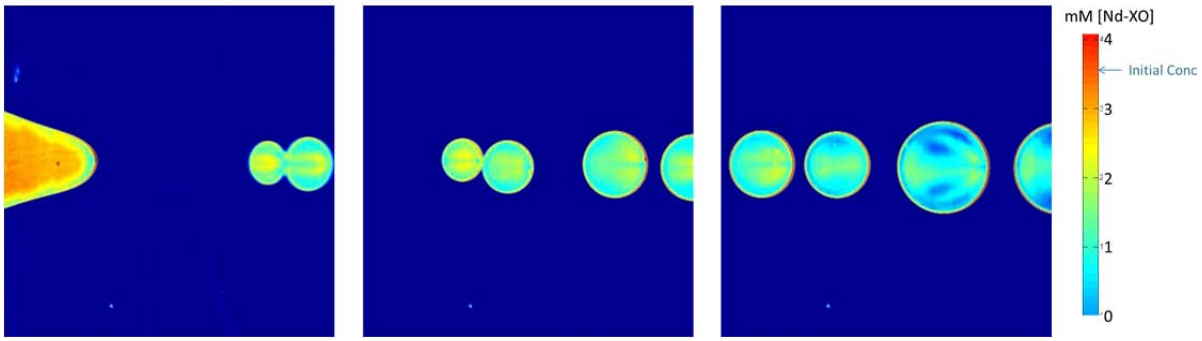

Figure 49. Mass transport in the thin microfocusing device shows high concentrations of Nd in the inflow stream, that leaches out as the droplet moves down the chip. Droplet coalescence occurs directly out of the generator and a second time downstream. Drops are approximately 100 µm in diameter. The continuous flow is 1.5 mL/hr of 0.2 M HTTA, 10^{-2} M TBP in dodecane, and the droplet fluid is 3.62 mM Nd^{3+}, 0.01 M Xylenol orange, and 0.2 M KHP in water.

Figure 49 shows that the highest concentration of Nd occurs in the inflow stream as demonstrated by the orange colors. As the drops move down the channel, the Nd leaches from the drop into the continuous phase, losing intensity. The effect of the circulation pattern, discussed in Section 4.2.4, can be seen in the image. In the first frame, two pockets of high concentration (yellow) can be seen in the drop. These areas are the center of the horizontal vortex that was imaged using particle tracking. The centerline of the drop is nearly the same concentration as close to the interface. Thus, the circulation decreases the distance that diffusion must occur over to only ¼ of the drop diameter. Since this circulation pattern can be seen clearly, the diffusion speed of Nd is much slower than the reaction speed at the interface. This confirms the classification of a similar case (0.2 M HTTA, 10^{-2} M TBP in dodecane, 100 µm deep channel) as diffusion limited, losing intensity.

For this system, two droplets are formed close together and coalesce almost immediately. Once these larger drops move down the chip, a second coalescence event occurs. These coalescence events lead to larger drops, which decreases mass transport rates by decreasing surface area, while also increases mixing, which could lead to enhanced mass transport. Quantitatively, we see that coalescence decreases mass transport and leads to lower separation rates [Figure 50]. Here, the error bars represent the standard deviation of the concentration values that are found in the 2D representation of the drop. In the case of no coalescence, the drops become homogeneous more quickly as compared to the case of coalescence, where the drops retain more of a concentration variation for a greater period of time. The variation in the average concentration in the drop also increases as the drops move down the channel.

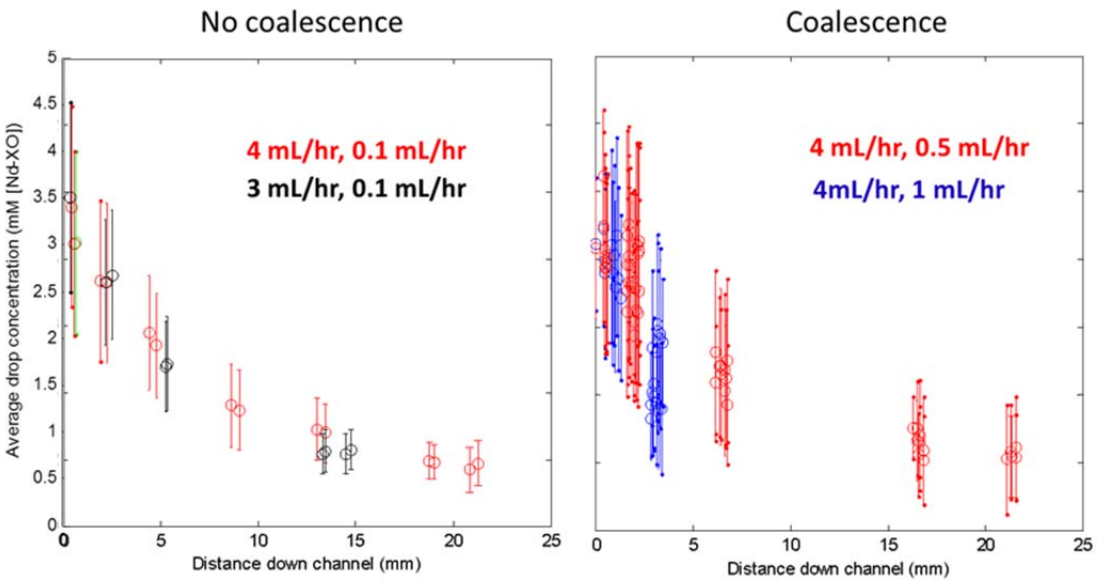

Figure 50.The left plot shows a system without coalescence while the right plot shows a system with coalescence. The flow rates for the outer and inner fluids are defined on the figure.

Knowing the effect of coalescence on mass transport could help us optimize the choice of rotation rates for the centrifugal contactors, since coalescence increases at the highest RPMs.

4.3.4 Conclusions

The flow-focusing microfluidic channel is a unique, controlled environment that allows many of the phenomena observed in centrifugal contactors to be explored. Flow-focusing channels produce monodisperse oil-in-water or water-in-oil emulsions with drop sizes that are on the order of those that are produced in contactors. Large droplets, with diameters approaching the channel depth, move in Poiseuille flow and experience a large amount of shear. This shear drives a circulation pattern in the droplet that increases the rate of mass transfer to the droplet. The circulation speed largely depends on the relative velocity of the drop with the channel wall and also with the continuous fluid. This shear is highly dependent on drop size, which is shown both experimentally and with an ALE FEM model. Unexpectedly, the concentrations of the surface active species HTTA and TBP do not affect the circulation pattern within the droplet in a measurable way.

Mass transfer coefficients were measured in the microfluidic chip for various concentrations of TBP and HTTA. The mass transfer was found to be first order in HTTA concentration, with only a weak dependence on TBP. Very similar results were also observed in the centrifugal contactor, as will be discussed in the next section. A diffusion limited regime was also observed, where the kinetics of the mass transfer were so fast at the droplet interface that the concentration of species in dodecane did not affect the rate constant significantly. This regime was also observed in the contactor experiments.

5 CONTACTOR MODELS

The annular centrifugal contactor is a unit operation designed to maximize mass transfer between two immiscible liquids. The contactor (cross section illustrated in Figure 51) consists of internal rotor that turns at a high velocity producing a mixing region of high shear and a separation region. In the mixing region, the shear breaks up both liquids to maximize the contact area and the flow is turbulent in nature. In the separation region, a centrifugal force causes the two liquids to then separate via buoyancy into two distinct phases.

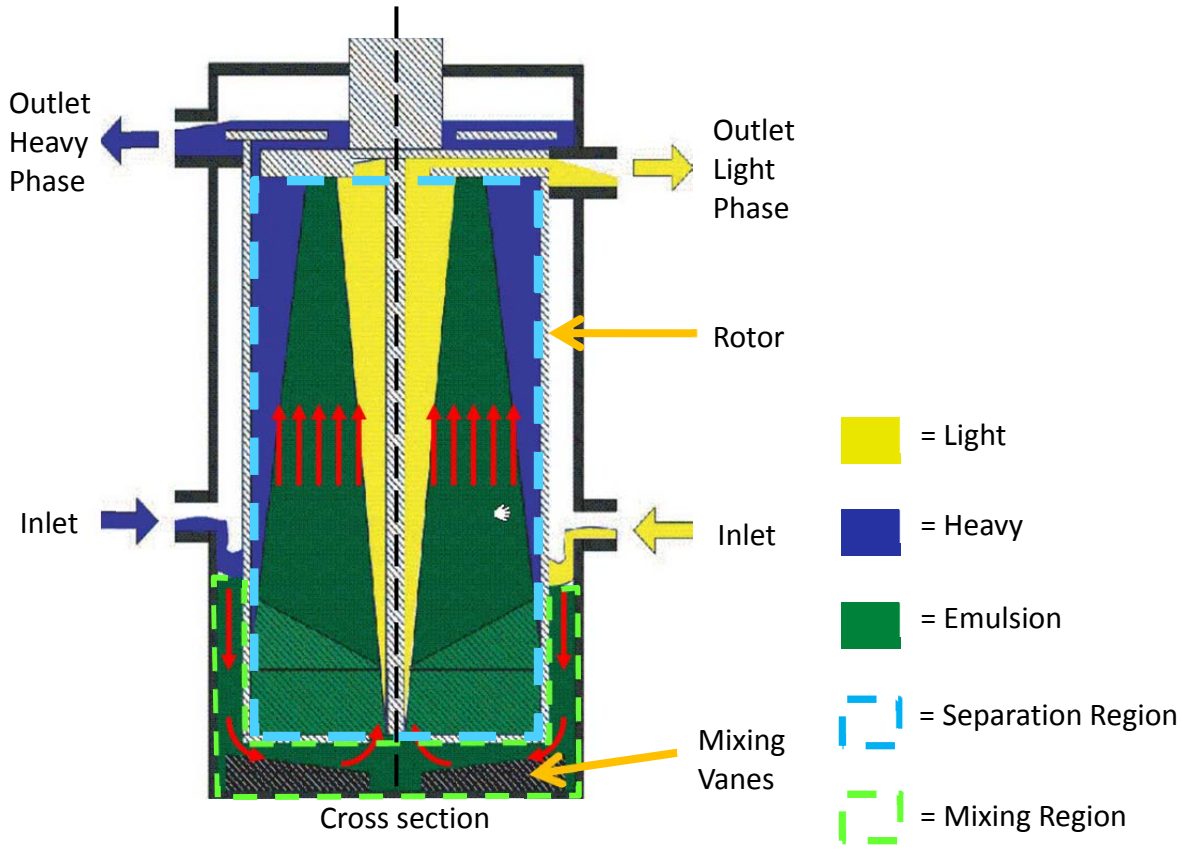

Figure 51: Cross-sectional view of an annular centrifugal contactor. The movement of the liquids through the device is illustrated by the red arrows. Within the mixing region, the liquids exist as an emulsion. The rotor rotates about the dashed black line.

5.1 Single Phase Models

As a first approximation to the flow within the mixing region, a single liquid (water) is considered and modeled using a Large Eddy Simulation (LES) using Sierra/Aria [Notz *et al.*, 2007]. The mesh of the geometry of interest is illustrated in Figure 52.

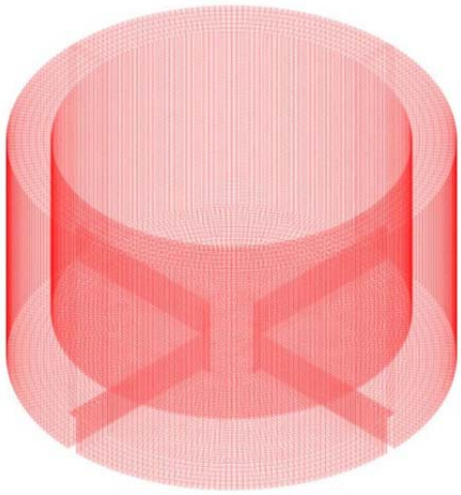

Figure 52: Mesh used for simulating the mixing region within the annular centrifugal contactor.

Figure 53 illustrates the cross section of the mixing region where the color represents the magnitude of the liquid. Initially, the liquid is stationary everywhere except near the rotor. As time progresses, eddies begin to form in the vertical sections where large shear exist. In the real system, the large shear regions help break up the two liquids to form an emulsion with small droplets. Over long times, eddies within the high shear region fluctuate in vertical position, but these fluctuations have a small influence on the overall flow profile.

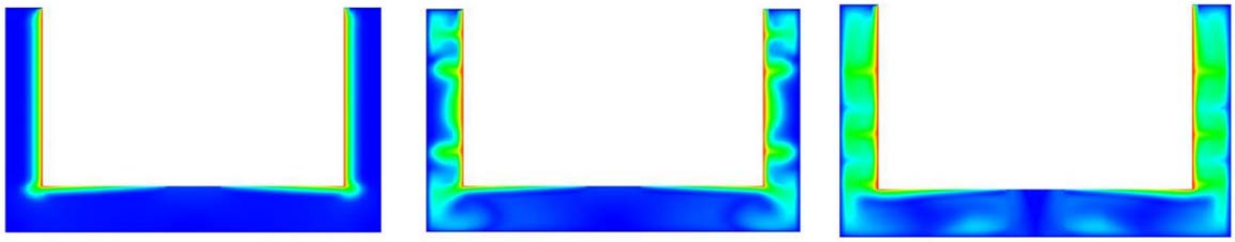

Figure 53: Cross section of the mixing region over time. The colors represent the magnitude of the velocity within the region

Figure 54 illustrates a plane within the lower portion of the mixing region. In this image, the colors represent the magnitude of the velocity, the lines represent the velocity vectors and the location of the mixing vanes is apparent. This image visualizes the influence the mixing vanes have on the flow profile. Between the mixing vanes, large eddies form to better enhance the mixing of the liquid in the region.

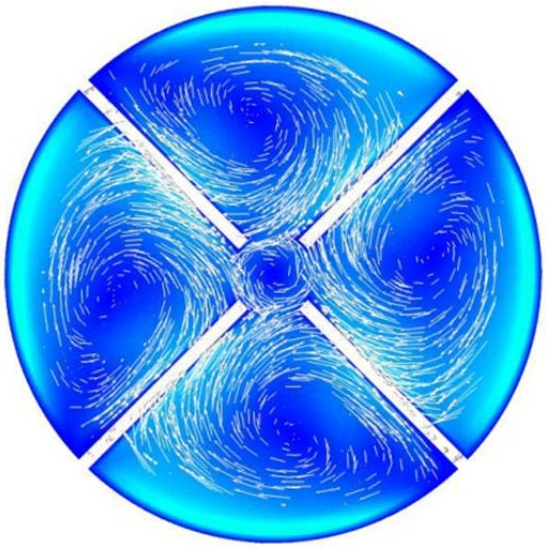

Figure 54: Bottom of the mixing region. Color represents the magnitude of the velocity and the lines represent the velocity vectors

Overall, this simulation illustrates the complex flow profile within the mixing region of the annular contactor. This region exhibits turbulence with regions of high shear. The purpose of this simulation was twofold. The first goal was to determine the capabilities of Aria on a complex geometry with a challenging turbulent flow profile. This goal was successfully met and is the largest turbulent flow simulation Aria has performed to date (>1 million unknowns). The second goal was to learn about the behavior of the flow within the contactor unit operation and how it changes over time. Future work will be able to build off these results by incorporating more sophisticated liquids that are more representative of the liquid used in the process. Additionally, the flow profile results can be used to help predict the amount of mass transfer that occurs with the end goal of helping design future annular contactors.

5.2 Multiphase Models

We have run the CVFEM/diffuse interface level set model on the centrifugal contactor in the previous section. (We were not yet able to get the CVFEM/CDFEM implementation to work for this complex of a flow.) Results from this two-phase flow, with properties for dodecane and water, are given in Figure 55. This is a result without surface tension but with density and viscosity differences between the aqueous and organic phases.

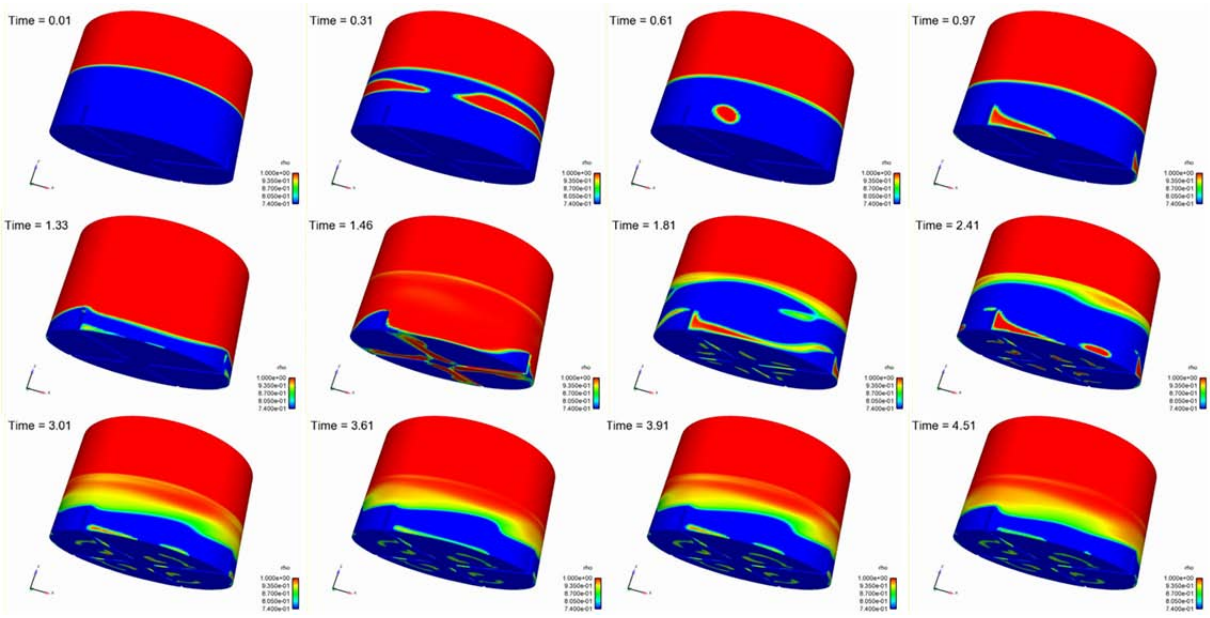

Figure 55. Two-phase simulations of flow in the centrifugal contactor using the CVFEM algorithm coupled to a diffuse interface level set method. The color bar shows the density of the fluids.

We start the simulation with an unfavorable stratification of the heavier fluid over the lighter fluid. As the simulation runs, heavy fluid drops into the mixing zone near the vanes. At long time, an oscillatory flow field is achieved that looks periodic in time. This is somewhat similar to what is seen in the real system, where the fluid-gas interface moves in a sinusoidal fashion with time.

5.2.1 Conclusions

Simplified models of centrifugal contactors were investigated in Sierra Mechanics. Here we have completed single phase models of flow in the contactor with turbulence, but without an inflow or outflow. We have also carried out two-phase flows in this contactor, again without an inflow or outflow. For future work, we would like to run a more refined version of this problem including surface tension and turbulence and eventually allowing for a full CVFEM/CDFEM coupling.

6 CONTACTOR EXPERIMENTS

6.1 Droplet Size Distribution and Spatial Distributions in Annular Centrifugal Contactors

Below find a summary of the paper to be submitted to AIChE Journal [Wyatt, O'Hern, Shelden, 2012]. For a copy of the full paper you can contact the PI.

6.1.1 Introduction

Annular centrifugal contactors have been developed as a single, compact unit utilized to transfer a desired species between two immiscible fluid phases. Critical to understanding the mass transfer characteristics associated with the complex flows in the annular mixing region is a clear picture of the distribution of droplet sizes of the various phases involved. To date, very little experimental data appears in the literature. We begin to fill that void by using laser fluorescence and optical methods to directly observe and measure drop size distributions for a silicone oil/water system in a centrifugal contactor. The shape and characteristics of the lognormal distributions, including the Sauter mean diameter and distribution means, are elucidated in terms of rotor speed (power consumption) and organic phase fraction. Further, the size distribution of entrained air bubbles is also examined. The results presented here will be invaluable in validating and expanding the predictive capacity of the many models that have been developed to describe the flow within these devices.

Accurately measuring the drop sizes in a centrifugal contactor is not trivial. The turbulent flow and entrained air bubbles make direct imaging using conventional techniques difficult. Further, the high rotor speeds at which contactors are often operated (> 3000 rpm) add to the difficulty of obtaining clear images of the multi-phase flow. Recently, several studies have been published in which researchers have successfully measured the characteristics of the multi-phase flow using various methods. Using a chemical method suggested by Doraiswami and Sharma [1984], Kadam et al. [2009] measured the effective interfacial area in three centrifugal contactors of varying diameter and levels of power consumption. From the measured power consumption and interfacial area, they were able to estimate Sauter mean diameters of 10 – 50 μm for various aqueous/organic systems. Later, Tamhane *et al.* [2011] used a phase Doppler particle analyzer to measure drop sizes in the mixing zone for three different organic phases with water and report average drop sizes in the range of 30 – 200 μm depending on power consumption. Most recently Schuur et al. [2012] used focused beam reflectance measurements to measure drop size distributions based on measurement of reflectance which is converted to chord size distributions using a correction factor. Using this technique, they report Sauter mean diameters that range from 150 m to over 600 m based on varying organic flow rates for a 1,2-dichloroethane/water system.

Here we present a more direct approach at experimental drop size distributions in an annular centrifugal contactor. Using laser-based fluorescence, clear optical images of the flow are attainable that can then be analyzed to directly determine sizes and distributions of droplets in the mixing zone. We examine the effect of rotor speed (power consumption) on the

distributions, average drop sizes, and Sauter mean diameter for a system of polydimethylsiloxane and water.

6.1.2 Materials and Methods

All of the experiments described here were performed using a CINC-V2 annular centrifugal available from CINC Industries, Inc. (Carson City, NV). The stainless steel contactor housing was replaced with a clear acrylic housing available from the manufacturer to enable optical measurements to be made with the contactor running (Figure 56).

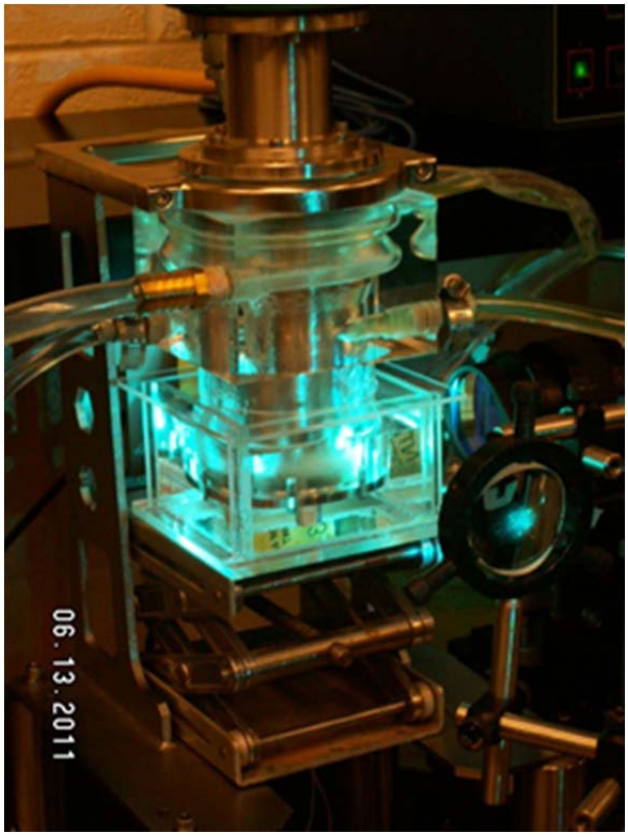

Figure 56: An image of the apparatus including the index-matched fluid bath needed to decrease distortion from the clear walls of the contactor

The inner diameter of the housing is 2.5 inches and the rotor has a diameter of 2 inches leaving a 0.25 inch gap in the annular region. The bottom vane plate used consists of 8 curved vanes having a tip-to-tip diameter of 2 3/16 inches. As such, the mixing vanes extend into the annular gap, but do not extend all the way to the housing wall. Tap water with no further purification was used for the aqueous phase while polydimethylsiloxane (PDMS) with a viscosity of 5 cSt (Clearco Products Co., Inc., Bensalem, PA) was used as the organic phase. For visualization, Nile red dye (Sigma-Aldrich, St. Louis, MO) was dissolved into the PDMS. The Nile red dye absorbs light in the range of 532 nm and fluoresces in the range near 600 nm. Images of the flow

in the contactor were obtained using a Phantom v9.1 high speed camera (Vision Research, Wayne, NJ) using a 10X magnification microscope objective (Figure 57). The lens was focused approximately 1mm away from the inner wall of the housing. Illumination was provided by shaping a Continuum Minilite PIV Nd:YAG laser beam (Continuum, Santa Clara, CA) into a light sheet with a 5 nanosecond pulse width. The camera was synchronized with the laser so that one laser pulse was emitted during each image acquired. The synchronization of the laser and camera provides crisp images by effectively freezing the droplet motion with the 5 ns pulse. Using this setup, we are able to visualize droplets ranging in size from 40 microns to 1 mm in diameter.

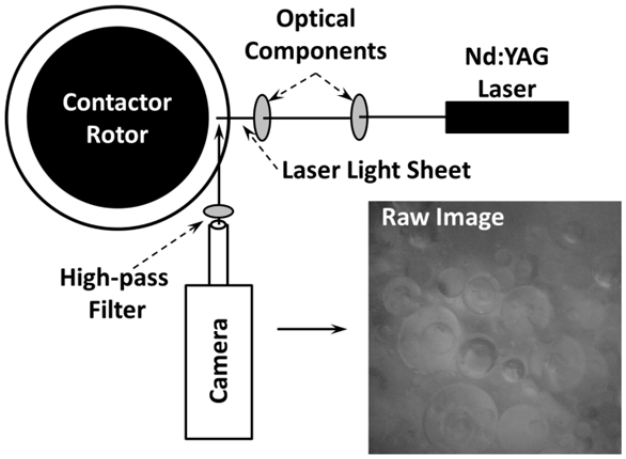

Figure 57. Schematic representation of the experimental apparatus (top view).

Three-phase flow in the contactor is shown in Figure 58, where a large head space exists filled with air. The liquid region is actually an emulsion of water and oil, with a large volume fraction of air bubbles.

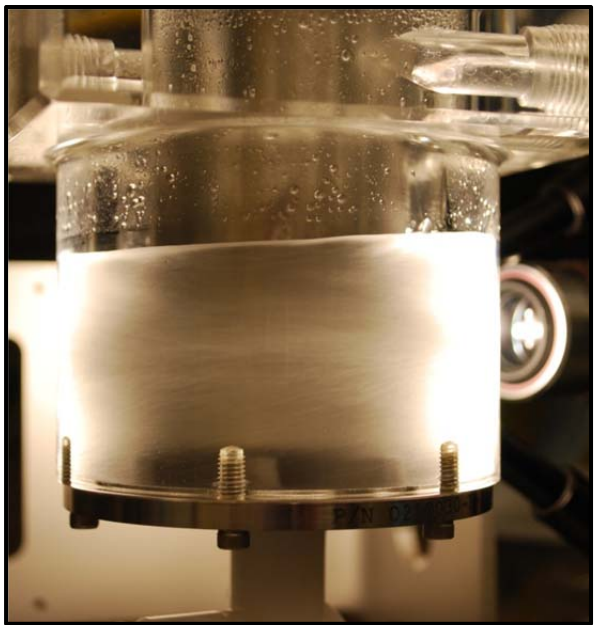

Figure 58. An image of the centrifugal contactor filled with water, oil and air.

Images were analyzed using the public domain image processing software ImageJ. Droplets were fit with circles whose diameters were then calculated. All but the largest droplets were spherical in shape. The diameters of droplets that were deformed in the flow were approximated by a circle having an area equal to the distorted droplet. An image of an object of known dimensions enabled scaling to real dimensions. For each distribution, at least 1000 droplets were used in the analysis.

6.1.3 Results and Discussion

6.1.3.1 Effect of Rotor Speed

The organic phase droplet size distribution was measured over a range of rotor speeds spanning from 1100 rpm to 3000 rpm (Figure 59). Each droplet size distribution was fit with a lognormal distribution function with good results. The lognormal shape of the distribution is consistent with what is expected for scenarios in which droplet breakup is important [Siegel and Sugihara, 1983]. At the lowest rotor speed, the distribution of drop sizes is very broad. As the rotor speed (or power consumption) increases, the peak of the distribution shifts to lower values and the distribution narrows meaning that the droplets in the contactor achieve a more uniform size than at low rotor speeds. Physically, as the rotor speed increases, the additional shear stress encountered by the fluid in the mixing zone is sufficient to break up the largest droplets in the two phase mixture which causes the distribution to both shift to lower droplet diameters, and to become narrower around the mean.

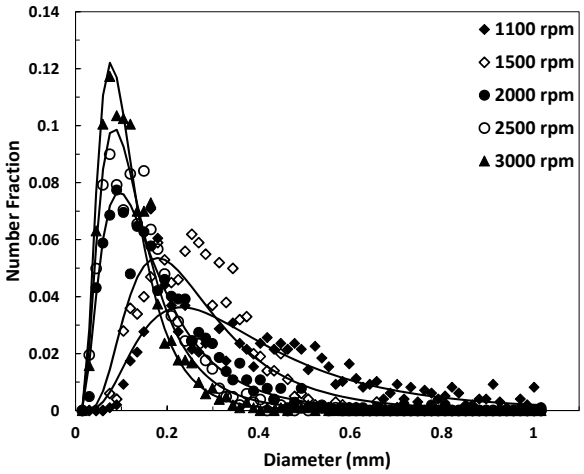

Figure 59. Organic phase droplet size distributions for several rotor speeds. Points indicate the experimental data while the solids lines show fits of the lognormal distribution function to the experimental data. Aqueous to organic feed ratio is 3:1 and total flow rate through the contactor is 5 mL/s.

The Sauter mean diameter and the mean of the distribution decrease in a power law fashion with increasing rotor speed (Figure 60). Further, the effective interfacial area increases logarithmically with increasing rotor speed. These results are both quantitatively and qualitatively similar to those reported for mixtures of 1,2-dichloroethane and water [Schurr *et al.*, 2012] and roughly one order of magnitude larger than those reported for silicone oil and glycerine [Kadam *et al.*, 2009]. The discrepancy between the results presented here and those obtained by Kadam et al. is likely due to the differences in physical properties of the aqueous phase chosen and, more importantly, the higher power consumptions studied, which would produce smaller droplets. At high rotor speeds, the average drop diameter and Sauter mean diameter become less dependent on the rotor speed. The decrease in dependence on the rotor speed is due to a developing dynamic equilibrium between the processes of drop coalescence and drop breakup.

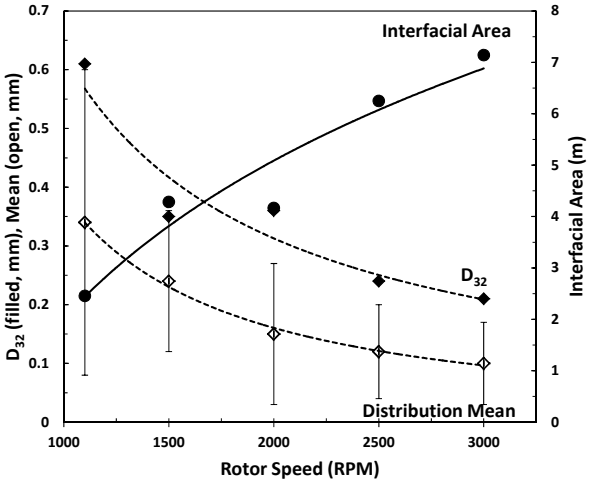

Figure 60. Effect of rotor speed on average droplet diameter, Sauter mean diameter, and interfacial area. Lines are guides to the eye. Error bars represent the standard deviation of the distribution. Aqueous to organic feed ratio is 3:1.

6.1.3.2 Spatial Evolution of Drop Size Distribution

The evolution of the organic phase drop size distribution as the mixture proceeds through the mixing zone was measured. Measurements were taken at three vertical locations in the mixing zone corresponding to normalized heights of 0.07, 0.30, and 0.65. The total liquid height in the mixing zone varies with rotor speed and total flow rate so the locations of the measurements are reported as normalized distances based on the total liquid height. In all cases, the drop size distributions are lognormal. Near the surface of the mixing zone, the drop size distribution is very broad indicating the presence of a significant number of large droplets (Figure 61). In this location, the aqueous and organic phases are just beginning to mix and there is a significant amount of air entrainment. As the mixture proceeds down through the mixing zone, the distribution becomes much narrower as the largest droplets break up under the stresses of the turbulent flow (Figure 61).

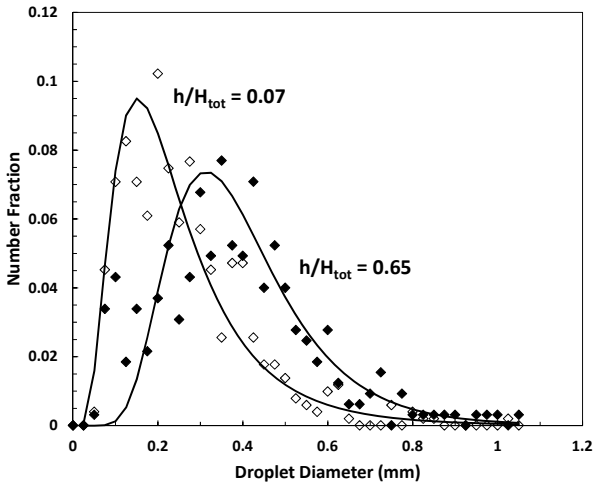

Figure 61. Drop size distributions as a function of vertical distance in the mixing zone for a rotor speed of 1300 rpm. For clarity, data at an intermediate vertical location was omitted from the figure.

The Sauter mean diameter, distribution mean, and effective interfacial area exhibit linear relationships with normalized height in the mixing zone (Figure 62). The Sauter mean diameter and distribution mean decrease linearly as the mixture moves from the entrance of the mixing zone to the vane region while the associated effective interfacial area increases linearly over the same distance. Further, the width of the distribution (shown here by the error bars representing the standard deviation of the distribution) decreases as the mixture approaches the vane region indicating that the distribution becomes more uniform as more and more of the largest droplets are broken up under the stresses of the turbulent annular flow.

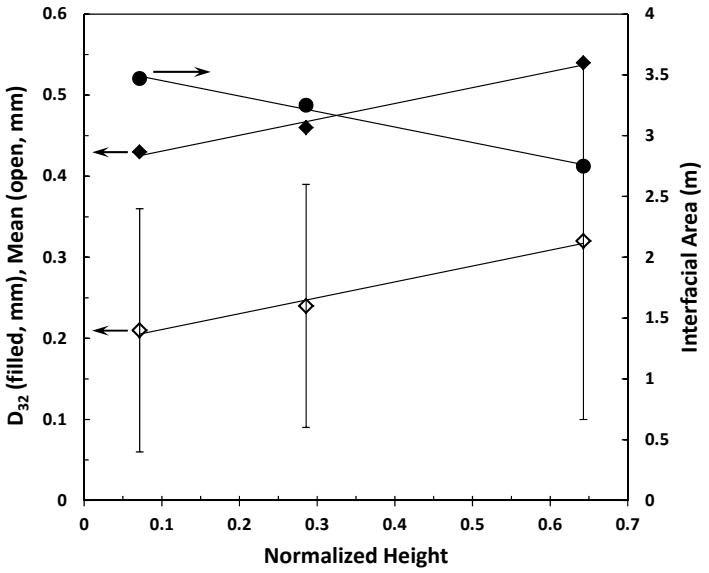

Figure 62. Average droplet diameter, Sauter mean diameter, and interfacial area as a function of the normalized vertical distance in the mixing zone for a rotor speed of 1300 rpm. Error bars represent one standard deviation of the data.

6.1.4 Conclusions

Effective liquid-liquid extraction is highly dependent on the surface area between the liquids involved in the mass transfer. To this end, we have characterized the drop size distributions obtained under various conditions of rotor speed, phase ratio, and vertical location in the mixing zone of an annular centrifugal contactor. The data presented here will be invaluable for validation of models developed to describe both the flow and mass transfer characteristics in centrifugal contactors as well as increasing the fundamental understanding of these systems.

The drop size distribution is well described by the lognormal distribution function. The distribution narrows and shifts to lower droplet diameters with increasing rotor speed as the largest droplets break up under the increased shear stresses in the turbulent flow. The aqueous to organic flow phase ratio has a weak effect on the Sauter mean diameter, distribution mean, and effective interfacial area for a constant flow rate. In the mixing zone, the distribution begins as a normal distribution near the free surface and evolves to be a relatively narrow lognormal distribution in the vane region.

6.2 Mass transport

Mass transport experiments were conducted in a CINC V2 contactor, operated at 3200 rpm, using a diluted version of the recipe used for the microfluidic experiments. The aqueous phase

consisted of 1.8 x 10^{-4} M Nd + 3.6 x 10^{-4} M xylenol orange in 0.1 M KHP buffer set to pH = 5.5. The organic phase consisted of 0.1 M HTTA + 0.1 M HTBP in dodecane (anhydrous 99%, Sigma Aldrich) diluted with various amounts of dodecane. The flow rates of the aqueous and organic phases through the contactor were 3 ml/min and 1 ml/min respectively. Flow rates were verified using a stop watch and a graduated cylinder. The aqueous outlet of the contactor was sampled periodically for later analysis by ICP-OES. The aqueous inlet of the contactor was continuously monitored spectrophotometrically using an Ocean Optics UV-VIS spectrometer which collected 400-700 nm spectra at 1 second intervals. The aqueous phase was recycled through the contactor to obtain kinetic data, while the organic phase was discarded after one pass through the contactor.

We used the same contactor set-up to examine mass transport in the contactor as we did to determine droplet-size distribution in the previous section. To avoid crazing the acrylic housing, we used the stainless-steel contactor since visual inspection on the system was unnecessary (Figure 63).

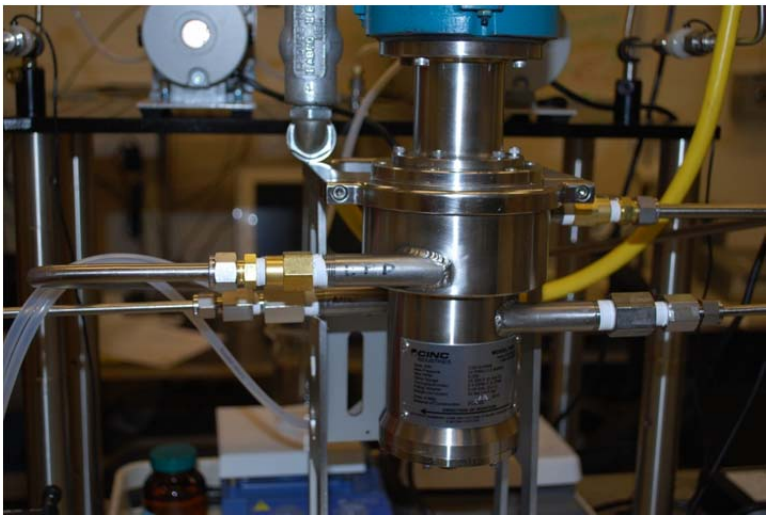

Figure 63. Stainless steel housing used for mass transport experiments.

Here we use the same Nd/TTA/TBP system as we used for the microfluidic mass transport experiments (see section 4.3).

We measure concentration in real-time using an ultraviolet visualization (UV-Vis) spectrometer as seen in Figure 64. We also periodically sampling effluent and analyze it using inductively coupled plasma mass spectrometry (ICP-MS).

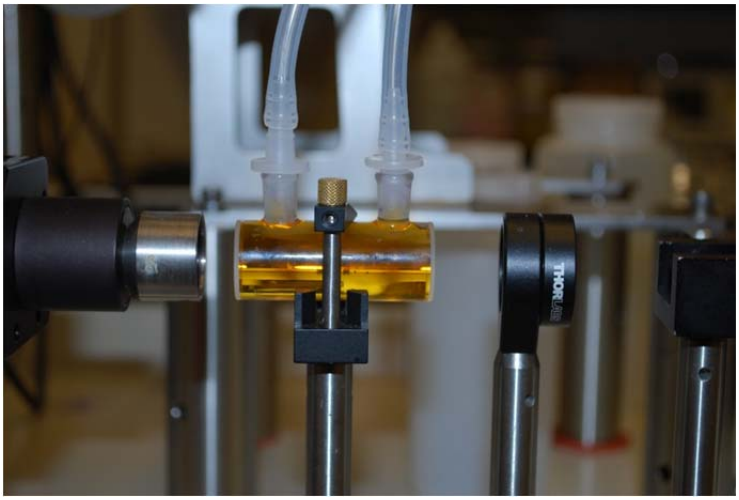

Figure 64. Real-time UV-Vis sampling of the effluent

Table 4. Partition data for the contactor relevant experiments. Here the initial $[Nd(XO)]_{aq}$ = 1.8 x 10^{-4} M, the xylenol orange concentration was 3.6 x 10^{-4} M, and the matrix solution was 0.1M KHP buffer pH = 5.45.

$[HTTA]_O$ initial (M)	$[TBP]_o$ initial (M)	$[Nd_T]_{aq}$ final (M)	D = $[Nd]o/[Nd_T]aq$
0.1	0.1	1.5 x 10^{-6}	1.2 x 10^{2}
0.1	0.1	1.3 x 10^{-6}	1.4 x 10^{2}
0.02	0.02	2.1 x 10^{-6}	8.3 x 10^{1}
0.02	0.02	2.0 x 10^{-6}	8.9 x 10^{1}
0.01	0.01	8.7 x 10^{-6}	2.0 x 10^{1}
0.01	0.01	8.7 x 10^{-6}	2.0 x 10^{1}
0.009	0.009	1.3 x 10^{-5}	1.3 x 10^{1}
0.009	0.009	1.3 x 10^{-5}	1.3 x 10^{1}
0.009	0.009	4.5 x 10^{-5}	3.0 x 10^{0}
0.005	0.005	1.0 x 10^{-4}	6.9 x 10^{-1}
0.003	0.003	1.2 x 10^{-4}	5.7 x 10^{-1}

The concentration of $[Nd]_{aq}$ at the exit of the contactor is shown in Figure 65 for two different concentrations of HTTA and TBP. The outlet Nd concentration is linear with time when plotted in the form of equation (23). At concentrations of 0.003 M HTTA and TBP and above, the curves collapse, which may indicate diffusion control dominates chemical kinetics.

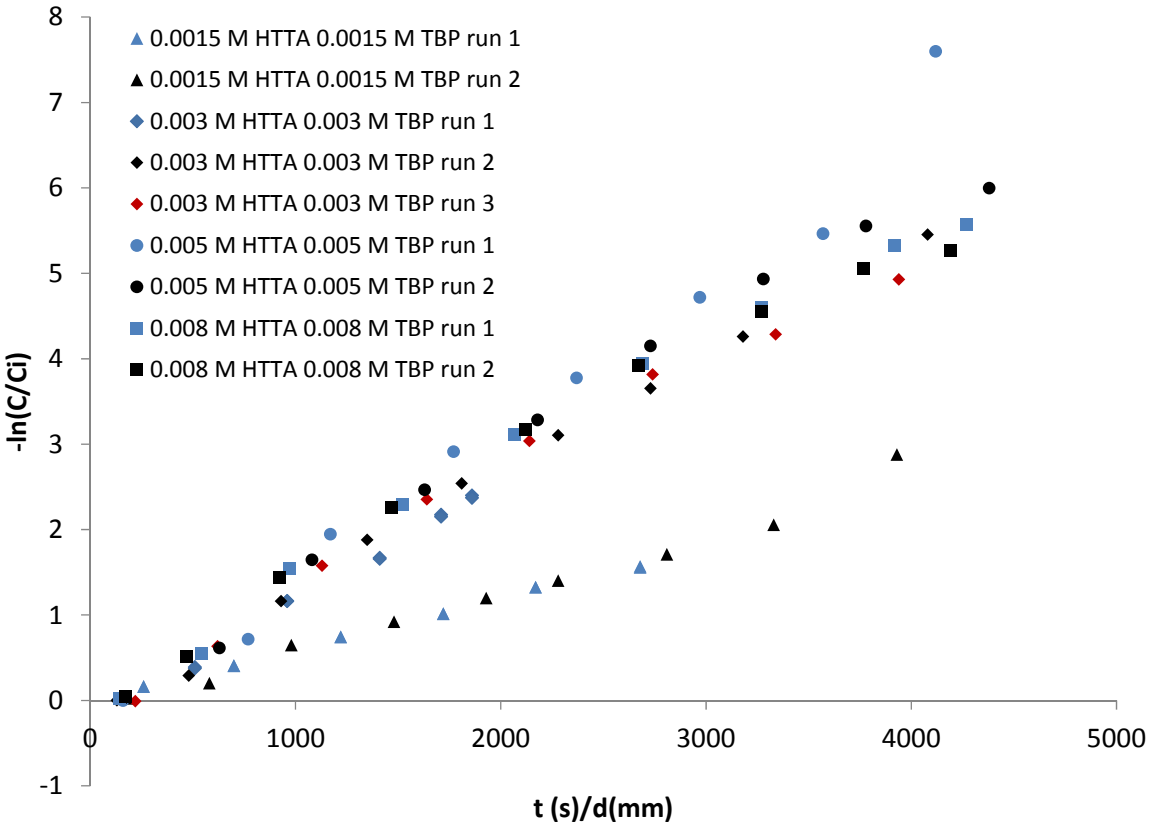

Figure 65. Aqueous Nd concentration versus time on the outlet of the contactor for various concentrations of HTTA and TBP

Table 5 gives the slopes of the curves from Figure 65 providing effective mass transfer rates from the contactor experiments. The mass transfer coefficients are not constant, but show dependence on the concentrations of HTTA and TBP.

Table 5. Effective mass transfer rate from the contactor experiments

HTTA (M)	TBP (M)	k_{eff} (mm/s)	Standard Deviation (mm/s)	Standard Error (mm/s)
0.008	0.008	1.3×10^{-3}	2×10^{-5}	2×10^{-5}
0.005	0.005	1.64×10^{-3}	2×10^{-4}	2×10^{-4}
0.003	0.003	1.48×10^{-3}	2×10^{-4}	9×10^{-5}
0.0015	0.0015	6.50×10^{-4}	9×10^{-5}	6×10^{-5}

7 THERMODYNAMIC MODELING

Below we have included an excerpt from the paper submitted to the journal *Solvent Extraction and Ion Exchange* [Jove-Colon *et al.*, 2012A]. A preprint of the journal article is available from the PI along with a short proceedings paper [Jove-Colon *et al.*, 2011]. In addition, many of the implementation details are available from a SAND report that will be published simultaneously to this one [Jove-Colon, et al, 2012B]. Both these documents include extensive literature reviews of some of the data available for uranium separations from fission products. The current approach makes use of a Gibbs energy minimization (GEM) method to compute chemical equilibria for a multiphase multicomponent system using the open-source object-oriented Cantera* (http://code.google.com/p/cantera/) code suite for constitutive modeling [Moffat and Jove-Colon, 2009].

7.1 Cantera Models of Uranium Extraction

Liquid-liquid extraction (LLE) is a widely used separation method for an extensive range of metals including actinides. The Gibbs energy minimization (GEM) method was used to compute the complex chemical equilibria for the LLE system HNO_3-H_2O-$UO_2(NO_3)_2$-TBP plus diluent at 25°C. The nonelectrolyte phase is treated as an ideal mixture defined by eight TBP complexes plus the inert diluent. The reactions included in the analysis are given in Figure 66.

$$TBP \bullet HNO_{3(org)} \rightleftarrows H^+ + NO_3^- + TBP_{org}$$

$$(TBP)_2 \bullet HNO_{3(org)} \rightleftarrows H^+ + NO_3^- + 2TBP_{org}$$

$$TBP_{aq} \rightleftarrows TBP_{org}$$

$$TBP \bullet H_2O_{(org)} \rightleftarrows TBP_{org} + H_2O$$

$$(TBP)_{2org} \rightleftarrows 2TBP_{org}$$

$$(TBP)_2 \bullet UO_2(NO_3)_{2(org)} \rightleftarrows UO_2^{++} + 2NO_3^- + 2TBP_{org}$$

$$(TBP)_2 \bullet Pu(NO_3)_{4(org)} \rightleftarrows Pu^{++++} + 4NO_3^- + 2TBP_{org}$$

Figure 66. Reactions included in this study

The chemical equilibria model developed in this study using the Cantera code suite is used to evaluate LLE for TBP metal extraction data in the system TBP-HNO_3-$UO_2(NO_3)_2$-H_2O-diluent. This compositional system was selected given the relatively large amount of extraction data available for a radionuclide LLE process such as PUREX. Our approach is somewhat similar in concept to others in treating the equilibria based on chemical reactions between electrolyte and nonelectrolyte phases as presented by Chaiko and Vandegrift [1988], and Moyer et al. [2001].

The Pitzer method is used to capture non-idealities in the concentrated electrolyte phase. The generated extraction isotherms are in very good agreement with reported experimental data for various TBP loadings and electrolyte concentrations demonstrating the adequacy of this approach to analyze complex multiphase multicomponent systems. The model is robust and yet flexible allowing for expansion to other LLE systems and coupling with computational tools for parameter analysis and optimization. Figure 67 shows the results from the analysis. From the two-phase Cantera model we were above to predict the distribution of uranyl nitrate from the aqueous to the organic phase for various concentrations of TBP. The data of Davis et al. [1970] are shown for comparison.

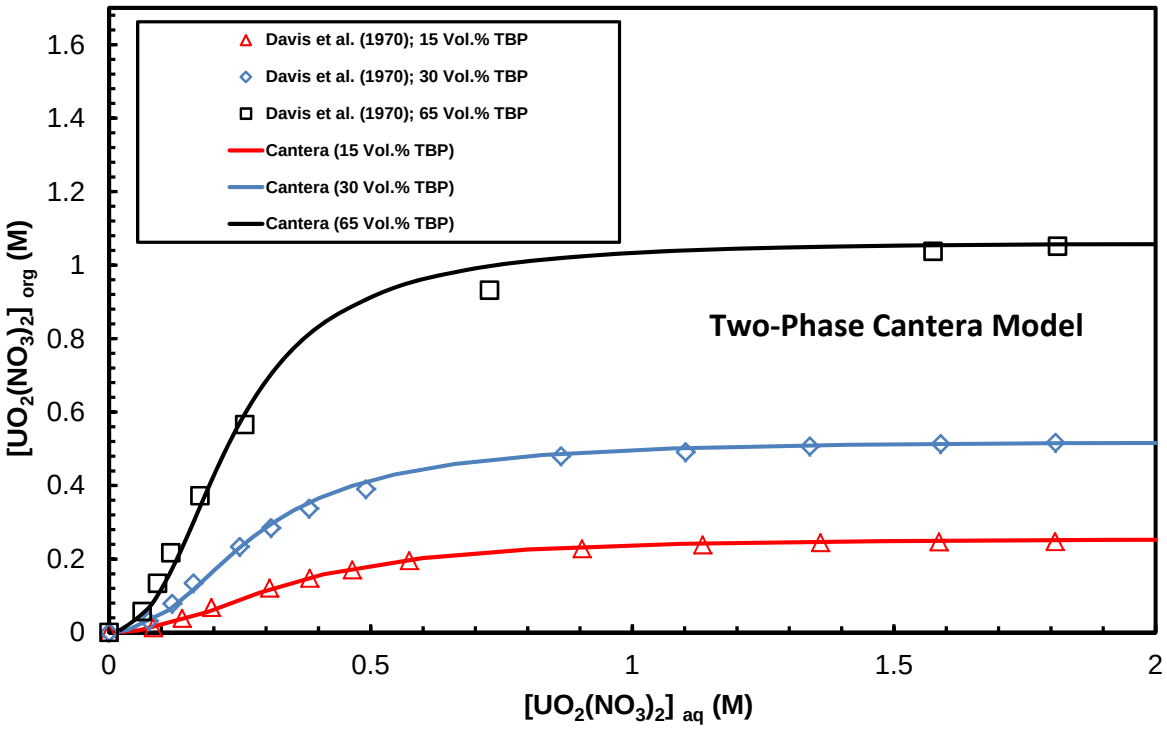

Figure 67. Comparison of calculated extractions isotherms (this study) using Cantera and reported data for $UO_2(NO_3)_2$ extraction by TBP – AMSCO diluent mixture [Davis et al, 1970].

7.2 Implementation plan for Thermodynamics into ARIA

7.2.1 Introduction

This note will describe the implementation of interfacial transport formulations within aqueous and organic liquids.

There are existing treatments for the interface mass transfer between aqueous and organic liquids

across an interface. For example, Danesi and Chiarizia (1980), Nitsch and Schuster (1983), and Nitsch and Van Schoor (1983) describe a treatment that involves the specification of boundary layer thicknesses on both the brine liquid and the organic side of the interfaces. See section 7.2.5.1 (model 1) for a test case of this implementation to the system TBP-NO_3-UO_2-H_2O and hexane diluent. The following sections will describe an implementation of these thin film treatments within an application environment based on Cantera that has been used previously to build subgrid Electrode Models for battery simulations (Muller et al, 2012). The method involves a subgrid model that incorporates its own state variables. This means that complexities with the interface can be confined to the subgrid model. It also means that time constants associated with those interfacial degrees of freedom may become rate limiting in the problem. Unless added to the global state variable, there is no other way to do this.

7.2.2 Implementation of Boundary Conditions on Discontinuous Variable Interfaces

Let's understand how the boundary conditions at a discontinuous variables interface are currently constructed in a detailed manner. The treatment will be taken from Goma. Then in the next section we will describe an alternative treatment.

7.2.2.1 Fluid Motion

We will assume that the densities may not be constant within each domain and also that the densities may have a jump discontinuity at the interface. We will derive two example cases: the momentum continuity equations and the species continuity equations. We will consider an interface between two materials, named "A" and "B". At that interface, we will assume that all variables are discontinuous unless stated otherwise. Thus, the velocity will have a different value on the "A" side of the interface versus the "B" side of the interface. These different values will be denoted by $\boldsymbol{u}^A$ and $\boldsymbol{u}^B$, respectively. The outward facing normal on the "A" side of the interface will be denoted by $\boldsymbol{n}^A$, while the outward facing normal on the "B" side of the interface will be denoted by $\boldsymbol{n}^B$. Note, $\boldsymbol{n}^A = -\boldsymbol{n}^B$. Interfacial mass transfer is occurring across the interface. However we will assume no net accumulation of mass at the interface here, but add in the capability later.

First, we will assume that the pressure fields are discontinuous across the interface. This has very important implications and is a prerequisite to the phase conservation property. The first is that the total continuity equation for phase A and phase B must be applied separately, Eqn. (24), and that means that phase continuity may be assured as well given suitable properties for the discretization method. In Eqn. (24) P_A is determined from the first equation, while P_B is determined from the second equation. The connection between P_A and P_B is determined from the traction condition on the momentum equation.

$$R_i^{C-A} = \int_{\Omega_A} \left[\left(\frac{d\rho^A}{dt} + \nabla \bullet \rho^A \boldsymbol{u}^A \right) \right] \phi_P^i d\Omega = 0 \tag{24}$$

$$R_i^{C-B} = \int_{\Omega_B} \left[\left(\frac{d\rho^B}{dt} + \nabla \bullet \rho^B \boldsymbol{u}^B \right) \right] \phi_P^i d\Omega = 0$$

The weighted residuals of the momentum equations on the "A" side of the interface, representing a continuity equation for the momentum in the "B" material domain, are given in Eqn. (25).

$$R_i^{M-A} = \int_\Omega \left[\rho^A \left(\frac{d\boldsymbol{u}^A}{dt} + \boldsymbol{u}^A \bullet \nabla \boldsymbol{u}^A \right) - f \right] \phi^i d\Omega + \int_\Omega \boldsymbol{T}^A \bullet \nabla \phi^i \, d\Omega - \int_\Gamma \left(\boldsymbol{n}^A \bullet \boldsymbol{T}^A \right) \phi^i \, d\Gamma = 0 \qquad (25)$$

The stress tensor may be quite complicated. However, for a Newtonian stress tensor assumption, the following holds.

$$\boldsymbol{T}^A = -\nabla P^A + \mu \left(\nabla \boldsymbol{u} + \left(\nabla \boldsymbol{u} \right)^T \right) - \left(\tfrac{2}{3} \mu - \kappa \right) \left(\nabla \bullet \boldsymbol{u} \right) \boldsymbol{\delta} \qquad (26)$$

On the "B" side of the interface the momentum boundary condition is represented by the condition in Eqn. (27).

$$R_i^{M-B} = \int_\Omega \left[\rho^B \left(\frac{d\boldsymbol{u}^B}{dt} + \boldsymbol{u}^B \bullet \nabla \boldsymbol{u}^B \right) - f \right] \phi^i d\Omega + \int_\Omega \boldsymbol{T}^B \bullet \nabla \phi^i \, d\Omega - \int_\Gamma \left(\boldsymbol{n}^B \bullet \boldsymbol{T}^B \right) \phi^i \, d\Gamma = 0 \qquad (27)$$

Note, in order to obtain Eqn.'s (25) and (27), we have subtracted out the total continuity equations for the two materials, Eqn.'s (28) and (29).

$$R_i^{C-A} = \int_{\Omega^A} \left[\frac{d\rho^A}{dt} + \boldsymbol{u}^A \bullet \nabla \rho^A + \rho^A \left(\nabla \bullet \boldsymbol{u}^A \right) \right] \psi^i d\Omega = 0 \qquad (28)$$

$$R_i^{C-B} = \int_{\Omega^-} \left[\frac{d\rho^B}{dt} + \boldsymbol{u}^B \bullet \nabla \rho^B + \rho^B \left(\nabla \bullet \boldsymbol{u}^B \right) \right] \psi^i d\Omega = 0 \qquad (29)$$

We write the total continuity equations separately for the "A" and the "B" side of the interfaces to reflect the fact that the two material balances are truly separate. We also use a separate symbol for the pressure basis function than for the velocity basis function. The pressure, on each side of the interface, which is the unknown corresponding to each of the continuity equations, Eqn. (28) and Eqn. (29), will exhibit a discontinuity at the boundary. There will be multiple pressure unknowns at boundary nodes, if the pressure unknowns are located at nodes. Indeed, there must be if Eqn's (28) and (29) are to be separate residuals. If they are not separate residuals, i.e., the pressure residual at node i is created from a sum of Eqns. (28) and (29), then each phase would forego having a separate total mass balance.

A common boundary condition applied at the interface is to apply the capillary boundary condition to the normal component of the normal stress. This provides a relationship between the normal stresses on either side of the interface:

$$\boldsymbol{n}^B \bullet \boldsymbol{T}^B = \boldsymbol{n}^A \bullet \boldsymbol{T}^A + 2H\sigma\boldsymbol{n}^B + \nabla_s \sigma \tag{30}$$

This capillary boundary condition may be applied at the interface between two materials as one of the boundary conditions. Note, however, that more boundary conditions are needed to specify the relationship between the velocities and pressures at the interface. For example, there are 6 velocity unknowns at the interface in a three dimensional problem. The capillarity condition only supplies three boundary conditions, due to the fact that it is a "vector" boundary condition. The other three boundary conditions for the velocities typically come from a strongly integrated boundary condition directly relating the total mass fluxes on either side of the interface, combined with closure for the interfacial mass flux of the last species in a multicomponent species mechanism.

Applying the capillary boundary condition with another set of boundary conditions would seem to be a hard task. However, a natural answer to this problem is to apply the capillary boundary condition by combining the momentum residuals for both sides of the interface, Eqns. (25) and (27), by summing them together. Then, the capillary boundary condition, Eqn. (30), can be applied directly to eliminate the two surface integral terms. The strongly integrated boundary condition gets applied to the other velocity residual equation.

$$-\int_\Gamma \left(\boldsymbol{n}^B \bullet \boldsymbol{T}^B\right)\phi^i d\Gamma = -\int \left(\boldsymbol{n}^A \bullet \boldsymbol{T}^A\right)\phi^i d\Gamma - \int \left(2H\sigma\boldsymbol{n}^B\right)\phi^i d\Gamma - \int \left(\nabla_s \sigma\right)\phi^i d\Gamma \tag{31}$$

Using the fact that $R_i^{M-A} = 0$ should be true, we can formulate an expression that completely eliminates the surface integral of the stress at the interface, Eqn. (32) below.

$$\begin{aligned} -\int_\Gamma \left(\boldsymbol{n}^B \bullet \boldsymbol{T}^B\right)\phi^i \, d\Gamma = \int_\Omega \left[\rho^A\left(\frac{d\boldsymbol{u}^A}{dt} + \boldsymbol{u}^A \bullet \nabla \boldsymbol{u}^A\right) - f\right]\phi^i d\Omega + \int_\Omega \boldsymbol{T}^A \bullet \nabla\phi^i \, d\Omega \\ -\int \left(2H\sigma\boldsymbol{n}^B\right)\phi^i d\Gamma - \int \left(\nabla_s \sigma\right)\phi^i d\Gamma \end{aligned} \tag{32}$$

Plugging this back in yields Eqn. (33) for the residual for the velocity unknowns corresponding to the "B" side of the interface.

$$\begin{aligned} R_i^{M-B} = &\int_\Omega \left[\rho^B\left(\frac{d\boldsymbol{u}^B}{dt} + \boldsymbol{u}^B \bullet \nabla \boldsymbol{u}^B\right) - f\right]\phi^i d\Omega + \int_\Omega \boldsymbol{T}^B \bullet \nabla\phi^i \, d\Omega \\ &+\int_\Omega \left[\rho^A\left(\frac{d\boldsymbol{u}^A}{dt} + \boldsymbol{u}^A \bullet \nabla \boldsymbol{u}^A\right) - f\right]\phi^i d\Omega + \int_\Omega \boldsymbol{T}^A \bullet \nabla\phi^i \, d\Omega \\ &-\int \left(2H\sigma\boldsymbol{n}^B\right)\phi^i d\Gamma - \int \left(\nabla_s \sigma\right)\phi^i d\Gamma \end{aligned} \tag{33}$$

What this means in practice for discontinuous variable interpolations is that the volumetric contributions for the momentum continuity equation for the "A" side of the interface are added

to the equation for the "B" side of the interface. This is quite a complication in terms of doing the indexing.

The capillary boundary condition that is described above should have a special boundary condition label attached to it. Let's call these types of boundary conditions Discontinuous-Variable Volumetric-Surface Integral Galerkin (**DVVSIG**) boundary conditions. These boundary conditions are ones in which a surface integral along one side of a boundary is replaced by a volumetric integral on the other side of the integral as well as possibly another surface integral along the boundary. This is accomplished by formulating the residual equation for a conserved quantity on the other side of interface (e.g., Eqn. (25)), plugging in the defining boundary condition into that residual equation (e.g., Eqn. (32)), and then substituting the resulting expression into the residual equation for the first side of the boundary (e.g., Eqn. (27)). The final result (e.g., Eqn. (33)) is a residual expression that includes volumetric integral contributions from both sides of the interface, combined with an additional surface integral representing the difference in the original integrated-by-parts surface integrals of the interfacial fluxes of the conserved quantities.

Note that these boundary conditions may be applied equally as well at interfaces at which there is not a discontinuity in the dependent variable. In other words, if $\boldsymbol{u}^A = \boldsymbol{u}^B$ in the case above. Let us call these cases as Volumetric-Surface Integral Galerkin (i.e., `VSIG`) boundary conditions to distinguish these cases from their discontinuous variables counterparts. In this case, no further boundary conditions on the velocities are needed to specify the velocity at the interface. Also, there would be no confusion concerning which equation number to apply the residual equation to, as there is only one set of velocity unknowns. However, in the discontinuous variables case, there are two or more sets of velocities at the interface. Though it makes no difference in the actual solution up to round off error, a convention as to which equation to apply the **`DVVSIG`** bc to must be adopted. Also, an additional boundary condition must be supplied to account for the additional degrees of freedom. This boundary condition is described in the next paragraph.

At discontinuous variable interfaces, these `DVSIG` boundary conditions must be combined with boundary conditions prescribing the discontinuity in value of the variables on either side of the interface. Currently the boundary conditions so described are these Tie boundary conditions. Typically, these boundary conditions would come from thermodynamics and kinetics. Within the code they are applied mainly as strongly integrated Dirichlet conditions. Therefore, let's give these boundary conditions the acronym `SIDTIE` boundary conditions, i.e., strongly integrated Dirichlet boundary conditions. An example of this type of condition is the `VELO_NORMAL_DISC` boundary condition, Eqn. (34). This boundary condition is a statement of conservation of mass from reactions on the "A" side of the interface. $\boldsymbol{u}^S$ is the interfacial velocity of the interface. S_A^S is the molar source rate for production of phase A from interfacial reactions, while $\tilde{M}_A$ is the average molecular weight of phase A. This equation is a specification of the Stefan-flux at the interface, which may be moving and should be applied on the A side.

$$\left[\int_{\Gamma}\left(\boldsymbol{n}^{A}\bullet\rho^{A}\left(\boldsymbol{u}^{A}-\boldsymbol{u}^{S}\right)\right)-\tilde{M}_{A}S_{A}^{S}\right]\phi_{u}^{i}\,d\Gamma \tag{34}$$

In the above treatment, we have introduced the interfacial velocity $\boldsymbol{u}^{S}$. Therefore, one additional equation is needed to close the equation description. This is the KINEMATIC_DISC boundary condition, which establishes mass continuity at an interface between two phases which exchange mass. It is applied on the mesh displacement equations at an interface between two phases as a strongly integrated Dirichlet condition. The interfacial velocity may be expressed in terms of the motion of the mesh, which deforms according to the movement of the interface. The mesh displacement is continuous across the interface. I believe the boundary condition, Eqn. (35), is evaluated by collecting each integral from their respective sides of the boundary. Thus, an integral contribution is needed from both sides of the boundary. When doing the element contributions for elements on the A side of the interface the first integral in Eqn. (35) is evaluated. Then, the second integral is evaluated when in elements corresponding to the "B" side of the interface. In The boundary condition may be applied on interfaces which have either one or two solved-for materials on them (i.e., either an internal or an external side set).

$$\int_{\Gamma}\left(\boldsymbol{n}^{B}\bullet\rho^{B}\left(\boldsymbol{u}^{B}-\boldsymbol{u}^{S}\right)\right)\phi_{u}^{i}\,d\Gamma+\left[\int_{\Gamma}\left(\boldsymbol{n}^{A}\bullet\rho^{A}\left(\boldsymbol{u}^{A}-\boldsymbol{u}^{S}\right)\right)-\frac{d\Theta^{s}}{dt}\right]\phi_{u}^{i}\,d\Gamma=0 \tag{35}$$

The VELO_NORMAL_DISC boundary condition employs Eqn. (35) as well, but then is applied to the velocity boundary conditions. It is a SIDTIE condition, so it is applied on the second degree of freedom of the normal velocity at each applicable node, say for example the "B" side of the interface. Thus, when in elements corresponding to the "A" side of the interface, the boundary condition gets applied onto the residual for a degree of freedom, $\boldsymbol{u}^{B}$, which isn't the interpolating degree of freedom, but involves integration of the interpolating degree of freedom, $\boldsymbol{u}^{A}$, across the element boundary. In elements on the "B" side of the interface, the residual is applied to the interpolating degree of freedom, $\boldsymbol{u}^{B}$.

7.2.3 Boundary Conditions for Mass Transfer in Non-Dilute Systems

In the previous section, we described the boundary conditions necessary for two single-species phases which can interchange mass. An example of this of course would be melting or sublimation problems. In this section, we now add multiple species to the mix. We retain all of the equations described so far and then add an additional set. For non-dilute mass transfer, additional boundary conditions must be specified, and the linkage with boundary conditions for momentum and the total mass flux must be understood.

The interface velocity equation, i.e., the time derivative of the mesh displacement unknown when the mesh follows the interface, is specified by the interfacial total mass conservation equation repeated here with additional terms, Eqn. (36). This boundary condition is frequently

called a `KINEMATIC_DISC` boundary condition within Goma, when the surface phase is trivialized.

$$\boldsymbol{n}^B \bullet \rho^B \left(\boldsymbol{u}^B - \boldsymbol{u}^S \right) + \boldsymbol{n}^A \bullet \rho^A \left(\boldsymbol{u}^A - \boldsymbol{u}^S \right) = \frac{d\Theta^S}{dt} \tag{36}$$

Here Θ is the density of the surface phase per area, having units of kg m^{-2}. Because we will be accounting for mass at the interface, Θ cannot be ignored.

The fundamental equation for the boundary condition at a moving interface for species *k* in phase A is given by Eqn. (37), which is a statement of conservation of species *k*.

$$\boldsymbol{n}^A \bullet \left[\rho^A Y_k^A \left(\boldsymbol{u}^A - \boldsymbol{u}^S \right) + \boldsymbol{j}_{A,k}^S \right] + M_A S_{A,k}^S = 0 \tag{37}$$

In this equation $\boldsymbol{n}^A$ is the outward facing normal to phase A, Y_k^A is the mass fraction of species *k* in phase A at the interface, $\boldsymbol{u}^A$ is the mass-averaged velocity of phase A at the interface. $\boldsymbol{u}^S$ is the interfacial velocity. $\boldsymbol{j}_k^A$ is the diffusional flux of species *k* on a mass-averaged basis. $S_{A,k}^S$ is the molar source rate of species *k* at the interface due to interfacial reactions. There are only *N-1* independent mass fraction unknowns. The solvent mass fraction unknown is usually dropped in lieu of the sum of mass fractions condition.

$$\sum_{k=1} Y_k^A = 0 \tag{38}$$

Equation (38) may be replaced with equivalent closure relations when alternative independent variables, such as the species concentration, c_k^A , are used such as the following condition, Eqn. (39), based on the equation of state for phase A.

$$\sum_{k=1}^{N} c_k^A = \overline{c}^A \left(T, P, X_k^A \right) \tag{39}$$

At the interface the Stefan-flux condition, Eqn. (40), specifies the interfacial velocity of phase A relative to the interfacial velocity.

$$\boldsymbol{n}^A \bullet \left[\rho^A \left(\boldsymbol{u}^A - \boldsymbol{u}^S \right) \right] + \sum_{k=1}^{N_A} M_A S_{A,k}^S = 0 \tag{40}$$

Inclusion of *N* species equations along with the total continuity equation leads to a degeneracy in the equation system. Therefore, one of the species equations must be discarded in the implementation. Care must always be taken in ensuring that the discarded species equation may be reproduced in the discrete equation system (by addition and subtraction of the other equation systems) to be identical to the species equations that are included in the system.

To add the species equation, we may start with the residual equation, Eqn. (41), where $M_A S_{A,k}^A$ is the homogeneous source term and $\boldsymbol{j}_k^A$ is the diffusive mass flux term for species A with respect

to the mass averaged velocity. Then, we plug Eqn. (37) into Eqn. (41) to generate a balance for species k in phase A. Balances for species *k* in phase B, Eqn. (42), follow analogously.

$$R_{Y_k}^A = \int_{\Omega a}\left[\rho^A\left(\frac{dY^A}{dt}+\boldsymbol{u}^A\bullet\nabla Y^A\right)-S_k^A\right]\phi^i d\Omega-\int_{\Omega a}\boldsymbol{j}_k^A\bullet\nabla\phi^i\,d\Omega+\int_\Gamma\left(\boldsymbol{n}^A\bullet\boldsymbol{j}_k^A\right)\phi^i\,d\Gamma=0 \qquad (41)$$

$$R_{Y_k}^B = \int_{\Omega b}\left[\rho^B\left(\frac{dY^B}{dt}+\boldsymbol{u}^B\bullet\nabla Y^B\right)-S_k^B\right]\phi^i d\Omega-\int_{\Omega a}\boldsymbol{j}_k^B\bullet\nabla\phi^i\,d\Omega+\int_\Gamma\left(\boldsymbol{n}^B\bullet\boldsymbol{j}_k^B\right)\phi^i\,d\Gamma=0 \qquad (42)$$

Note, that there are only N_A-1 linearly independent equations for Eqn. (41). A closure equation of the type Eqn. (38) must be used for the last species equation in each phase. It can be shown that an equivalent residual equation for the last species to Eqn. (41) may be formulated by linear combinations of other residual equations.

7.2.4 Alternative Approach

Frequently, resolution of the boundary layer within a flow simulation isn't a productive pursuit due to length scale issues. This is especially the case for turbulent liquid systems where the diffusion rate constants are small and where turbulent diffusive transport is used to intermix the bulk regions leaving small laminar boundary layer regions near interfaces. In that case it would be better to have an alternative code solve for the laminar boundary layer. Then, we may use the sub-problem to supply the flux conditions specified in the previous section.

Phase A and phase B have momentum conservation equations and total conservation equations associated with them that are valid through the boundary layers on either side. The total continuity equation for phase A is given by Eqn. (43).

$$\frac{d\rho^A}{dt}+\nabla\bullet\left(\rho^A\boldsymbol{u}^A\right)=0 \qquad (43)$$

The momentum equation for phase A is

$$\frac{d\rho^A\boldsymbol{u}^A}{dt}+\nabla\bullet\left(\rho^A\boldsymbol{u}^A\right)+\nabla P^A+\nabla\bullet\underline{\underline{\boldsymbol{T}}}^A=0 \qquad (44)$$

We will be assuming that the flow parallel to the boundary may be decoupled from solution of interfacial mass transport perpendicular to the boundary. Therefore, these equations may be solved only in the direction aligned with the boundary (which we take as the *x* direction) and velocities in the *y* and *z* direction are taken as solenoidal. Note the solenoidal assumption doesn't hold for some important cases such as an expanding bubble, and the equation would have to be modified. However, assuming solenoidal, the total continuity equation reduces to Eqn. (45).

$$\frac{d\rho^A}{dt} + \frac{d}{dx}\left(\rho^A u_x^A\right) = 0 \tag{45}$$

The total momentum equation becomes Eqn. (46).

$$\frac{d\rho^A u_x^A}{dt} + \frac{d}{dx}\left(\rho^A u_x^A u_x^A\right) + \frac{dP^A}{dx} - \frac{4}{3}\frac{d}{dx}\left(\mu \frac{du_x^A}{dx}\right) = 0 \tag{46}$$

We may implement an interfacial kinetics object at the interface. It has internal variables consisting of the species defined at the interface (and perhaps other variables such as residual stresses), which are expressed in terms of site fractions. The conservation equation for surface species *k* is given by Eqn. (47).

$$C^S \frac{d\theta_k^S}{dt} + S_{S,k}^S = 0 \tag{47}$$

Putting these equations into a discretization scheme involves adding diffusion through a laminar boundary layer on both sides of the interface. We will attempt to do this in a one cell distance.

Additionally, a velocity reference frame must be chosen to solve the equation system in. The simplest method to solve these equations is by using the interfacial velocity reference frame. In this reference frame the domain is convected with a velocity equal to the interfacial velocity. Other choices can be made, however, such as setting the velocity at the edge of the A boundary layer to zero.

We will discretize the equations using a two control volume cell approximation over each of the A and B domains. Below the subscript *s* will refer to quantities defined at the interface. * will refer to quantities defined at the middle of the boundary layer. Figure 68 provides a depiction of the model. This is a general object that is derived from work on electrode objects. They are meant to be used as detailed subgrid models within a larger code. They are meant to be used for processes which have piecewise continuous source terms within them. Therefore, they are able to handle discontinuous time events by solving for the time at which discontinuities occur. Note, this may occur for interfacial mass transport systems when interfacial layers are birthed or deathed. This occurs frequently in mass transport systems such as passive layers in corrosion systems or for interfacial transport across cell membranes. These surface films are frequently the dominant rate limiting steps for mass transport at room temperature. But, their proper treatment has lagged due to lack of the software infrastructure. These objects have state variables associated with them. The state variables are not part of the global solution vector.

7.2.5 Interfacial Mass Transport Models

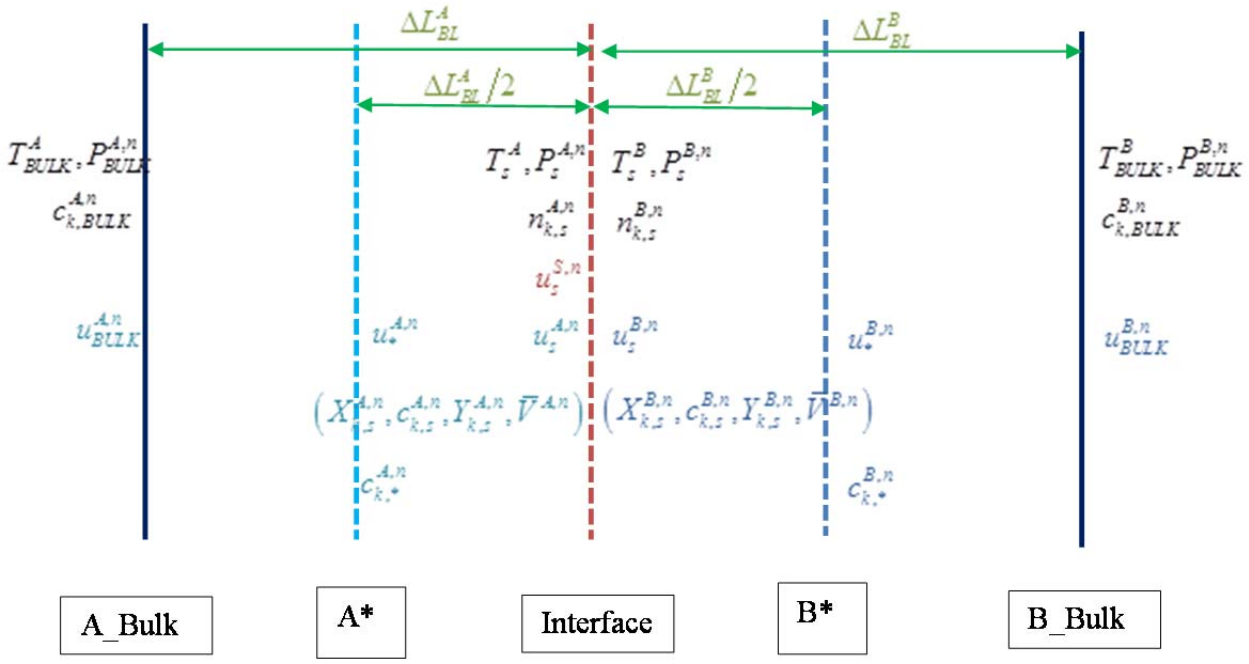

Figure 68. A schematic depiction of Boundary Layer Approximation. This picture is used for Model 2 and additional models beyond that model.

7.2.5.1 Model 1

In this model we assume that the mass transfer to the surface is fast, or that mass transport to the surface is handled by the enclosing application. Therefore, the boundary layer for phase A and B are considered to be infinitely thin, and the interfacial mole fractions of species in phases A and B are the same as those in the bulk. Note, in practical terms for liquid systems this is frequently not the case that mass transport is fast, and under current experimental conditions this is apparently not the case either.

We will also assume that the interface is in a pseudo-steady-state approximation. However, for future work this doesn't necessarily have to be the case and the software is constructed, i.e., the have state variables associated with them, so that it doesn't have to be the case. If it were not the case, then the extra degrees of freedom for interfacial quantities such as surface species concentrations could be hidden from the surrounding application, and could be at the same time rate limiting within the application. This concept is exercised more fully for electrode objects which use the same structure as the `InterfacialMassTransport` object, is explained more fully in Muller et al., [2012].

The object is called `imtPSS_NoSurf()`. It inherits from `InterfacialMassTransfer_PseudoSS`, which in turn inherits from from `InterfacialMassTransfer_interface()` and then the base class from `InterfacialMassTransfer()`.

Using these approximations, the actual residual calculations used within the object become trivial. They consist of the following trivial equation, Eqn. (48), for the single unknown Δt^n_{calc}.

$$\Delta t^n_{calc} \ : \ \Delta t^n_{calc} - \Delta t^n = 0 \tag{48}$$

However, behind the scenes a pseudo steady-state approximation for the interfacial site fractions is being solved for at every time step.

$$C^S \frac{d\theta^S_k}{dt} = -S^S_{S,k} = 0 \tag{49}$$

Within the pseudo steady-state calculation, just about all terms are boundary conditions. $T^A_s, P^{A,n}_s$ and $X^{A,n}_{k,s}$ are considered boundary conditions and specified by their values at $T^A_{BULK}, P^{A,n}_{BULK}$, and $X^{A,n}_{k,BULK}$. Then, the object will calculates the surface creation rates of all species in phases A and B. From the Stefan flux relations the interfacial Stefan velocities of phase A and B are then calculated.

An aspect of this model can be envisioned by specifying thickness to the boundary layers for phases A and B and assigning reaction rates to a set of interfacial reactions. The system TBP-NO_3-UO_2-H_2O and hexane diluent has been chose as a test case of this implementation based on the uranium coextraction study by Nitsch and Van Schoor (1983). The selected reaction set with species in phases A and B is given in Table 6. Note that a thermodynamic description of this system has been assessed in previous sections of this report. That is, the bulk thermodynamic properties of species in phases A and B in the model are represented by those assessed in this report to describe liquid-liquid extraction equilibria for this system. This reaction set composed of seven reactions between electrolyte and nonelectrolyte phase components accounts for the transfer of $UO_2(NO_3)_2$, HNO_3, and H_2O as well as TBP solubility into the aqueous phase. The forward reaction rates for TBP complexation with H_2O and that for the TBP(aq) were set arbitrarily. It should be noted that forward rates for these TBP- H_2O and TBP(aq) reactions do not significantly affect the mass transfer kinetics but were included for completeness. On the other hand, TBP•HNO_3 and $(TBP)_2$•$UO_2(NO_3)_2$ reaction rates strongly affect the resulting mass transfer rate profile. These reactions rates were adjusted to fit the coextraction rate data given by Nitsch and Van Schoor (1983). The boundary layer thickness for both phase A and B is equally set arbitrarily to 0.001 meters for the base case; this case refers to the one with the lowest transport coefficient for uranium as given by the authors. Initial uranium and nitric acid concentrations are 0.5 and 1.1 moles/L, respectively. Figure 69 shows the $UO_2(NO_3)_2$ and HNO_3 extraction data and predictions from the models given by Nitsch and Van Schoor (1983) and that described in this section. Notice the "spike" in HNO_3 concentration at early times and subsequent attenuation to an apparent steady state value. The model given by Nitsch and Van Schoor (1983) provides a reasonable prediction of the observed trend for HNO_3 extraction

whereas the current model deviates at early times but it is reasonable agreement at later times. The fact that such a "spike" is not reflected in the $UO_2(NO_3)_2$ concentration is a bit contradictory to the expected mass transfer behavior from NO_3 speciation in the organic phase. The current model predictions for uranium are in good agreement with the experimental data. To test the effect of boundary layer thickness, experimental extraction data, also from Nitsch and Van Schoor (1983), was used to fit thicknesses at various stirring speeds. The boundary layer thickness values that closely represent the experimental data are 0.00020, 0.00010, 0.000065, and 0.000050 meters for stirring speeds of 150, 200, 250, and 300 min^{-1}. The results are depicted in Figure 70 showing overall agreement between model predictions and experimental data. It should be recognized that the boundary layer thicknesses were obtained only by adjusting the thickness values to the experimental rate data and without any changes to base case reaction rate parameter data. The model provides good conformance to existing extraction data capturing the dependence on boundary layer thickness.

Table 6. Effective reaction set and forward rates used in the model test case

Reaction	Forward Rate (k_f) (1/seconds)
$TBP{\bullet}H_2O(org)$ [=] H_2O + TBP(org)	1.00E-03
$(TBP)_2{\bullet}$ $(H_2O)_2(org)$ [=] $2H_2O$ + 2TBP(org)	1.00E-03
$(TBP)_3{\bullet}$ $(H2O)_6(org)$ [=] 3TBP(org) + $6H_2O$	1.00E-03
TBP(org) [=] TBP(aq)	1.00E+02
$TBP{\bullet}HNO_3(org)$ [=] NO_3^- + H^+ + TBP(org)	1.00E+02
$(TBP)_2{\bullet}HNO_3(org)$ [=] NO_3^- + H^+ + 2TBP(org)	1.00E-01
$(TBP)_2{\bullet}UO_2(NO_3)_2(org)$ [=] UO_2^{++} + $2NO_3^-$ + 2TBP(org)	1.00E-01

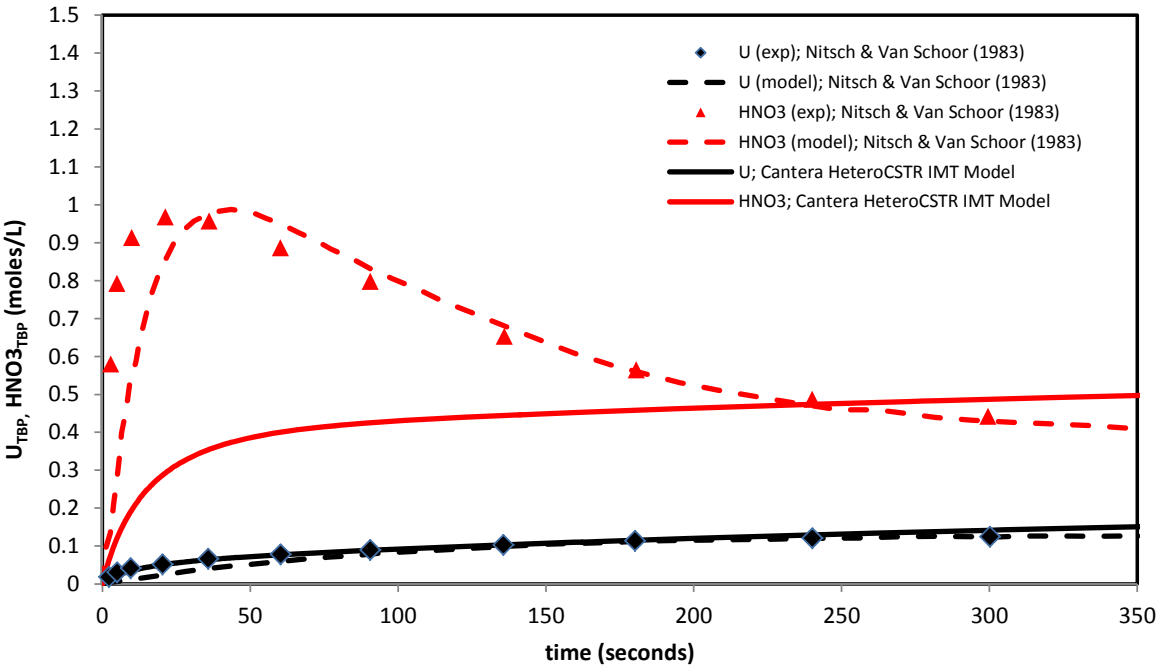

Figure 69. Cantera interfacial mass transfer model predictions and coextraction experimental data for uranium and nitric acid (see text).

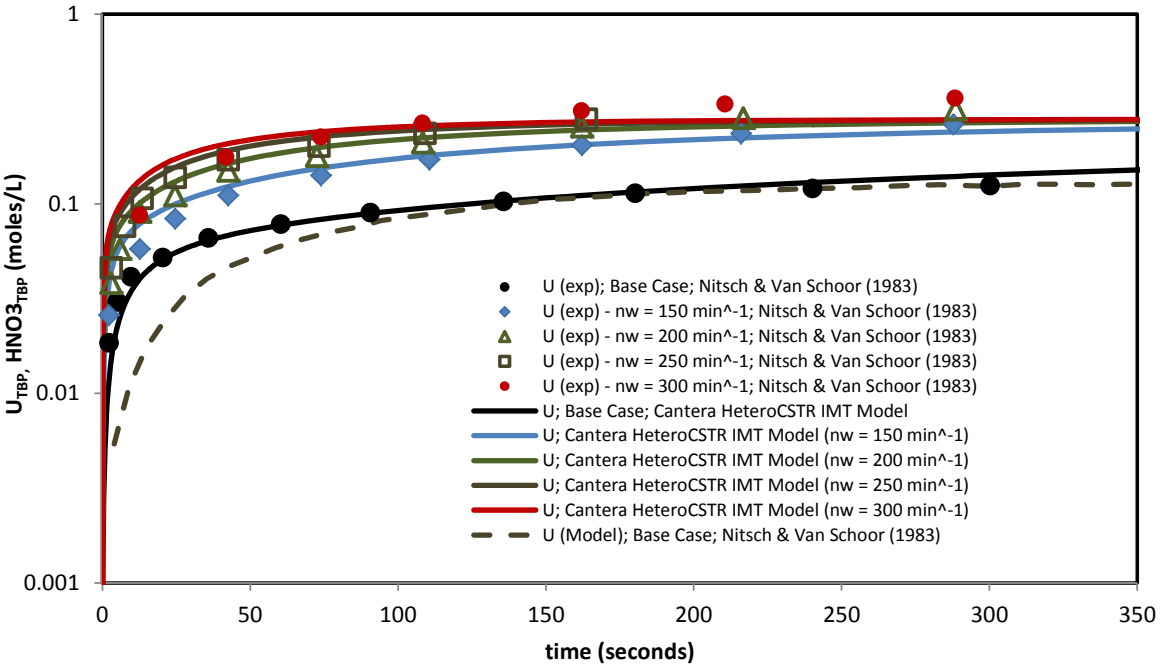

Figure 70. Cantera interfacial mass transfer model predictions and coextraction experimental data for uranium as a function of stirring speed (see text). The fitted boundary layer thickness values are 0.00020, 0.00010, 0.000065, and 0.000050 meters corresponding to stirring speeds of 150, 200, 250, and 300 min-1

7.2.5.2 Model 2

Model 2 doesn't employ a pressure unknown. Therefore, the axial momentum equation is not used. Instead the axial velocity unknowns are associated with the total continuity equation. In this model we calculate everything relative to the mass averaged velocity at the edge of the Phase A control volume, $u_*^{A,n} = 0$. Then the total continuity equation for the phase A control volume is used as the equation for the interfacial velocity, $u_s^{s,n}$. Also, the total continuity equation for the phase B control volume is used as the equation for the velocity at the edge of the phase B control volume, $u_*^{B,n}$.

All control volumes are convected relative to the interface velocity. Therefore, all boundary layer thicknesses are constant through the time step n. This means that there is a Lagrangian velocity component for unknowns identified with the * boundaries; these terms are identified by the u^{ref} term.

We use the species mole numbers as the independent unknowns. The closure relation is handled by a variation of Eqn. (39). We use the following equation set with associated independent variables defined to the left of the equation. Eqns. (51) to (54) refer to the control volume over the A phase.

$$\Delta t_{calc}^n \ : \ \Delta t_{calc}^n - \Delta t^n = 0 \tag{50}$$

$$u_s^{s,n} \ : \ \frac{\rho_s^{A,n} - \rho_s^{A,n-1}}{\Delta t^n}\frac{\Delta L_{bl}^A}{2} - \left(\left(-i\right) \bullet \rho_*^{A,n} u_*^{A,n}\right) - \rho_*^{A,n} u^{ref} - i \bullet \rho_s^A \left(u_s^{A,n} - u_s^{s,n}\right) = 0 \tag{51}$$

$$u_*^{A,n} \ : \ u_*^{A,n} = 0 \tag{52}$$

$$n_{k,s}^{A,n} \ : \ \begin{aligned} &\frac{\Delta L_{BL}^n}{2}\left(\frac{Y_{k,s}^{A,n}\rho_s^A - Y_{k,s}^{A,n-1}\rho_s^{A,n-1}}{\Delta t^n}\right) \\ &-\left(\left(-i\right) \bullet \rho_*^A u_*^A Y_{k,*}^{A,n}\right) - \rho_*^A u^{ref} Y_{k,*}^{A,n} - \boldsymbol{i} \bullet \boldsymbol{j}_{x,k,*}^{A,n} - i \bullet \rho_s^A \left(u_s^A - u_s^s\right) Y_{k,s}^{A,n}\right) = 0 \end{aligned} \tag{53}$$

$$n_{0,s}^{A,n} \ : \ \sum n_{k,s}^{A,n} = \frac{\Delta L_{BL}^n}{2} A \bar{V}_s^{A,n} \tag{54}$$

The B phase control volumes are represented by Eqns. (55) to (57).

$$u_*^{B,n} \ : \ \frac{\rho_s^{B,n} - \rho_s^{B,n-1}}{\Delta t^n}\frac{\Delta L_{bl}^B}{2} - \left(\left(-i\right) \bullet \rho_*^{B,n} u_*^{B,n}\right) - \rho_*^{B,n} u^{ref} - i \bullet \rho_s^B \left(u_s^{B,n} - u_s^{s,n}\right) = 0 \tag{55}$$

$$n_{k,s}^{B,n} \;:\; \frac{\Delta L_{BL}^{n}}{2}\left(\frac{Y_{k,s}^{B,n}\rho_s^B - Y_{k,s}^{B,n-1}\rho_s^{B,n-1}}{\Delta t^n}\right) - \left(\left(-i\right)\bullet \rho_*^B u_*^B Y_{k,*}^{B,n}\right) - \rho_*^A u^{ref} Y_{k,*}^{B,n} \textbf{ - } \boldsymbol{i}\bullet\boldsymbol{j}_{x,k,*}^{B,n} - i\bullet\rho_s^B\left(u_s^B - u_s^s\right)Y_{k,s}^{B,n}\right) = 0 \tag{56}$$

$$n_{0,s}^{B,n} \;:\; \sum n_{k,s}^{B,n} = \frac{\Delta L_{BL}^{n}}{2} A\bar{V}_s^{B,n} \tag{57}$$

Note this is a DAE system, as the velocities don't have time derivatives. A compressible formulation would have to be introduced to alleviate this potential problem. This is outlined in Model 3 in the next section.

We then set $u^{ref} = u_s$. In other words we make sure that the control volumes stay tracked with the interface velocity. We also note that:

$$\rho_s^A\left(u_s^{A,n} - u_s^{s,n}\right) = \sum M_k S_k^{A,n} \qquad Y_k^{A,n}\rho_s^{A,n}\left(u_s^{A,n} - u_s^{s,n}\right) = M_k S_k^{A,n}$$

$$\rho_s^{B,n}\left(u_s^{B,n} - u_s^{s,n}\right) = \sum M_k S_k^{B,n} \qquad Y_k^{B,n}\rho_s^{B,n}\left(u_s^{B,n} - u_s^{s,n}\right) = M_k S_k^{B,n}$$

With this in mind the full equation set becomes Eqns. (58) to (65).

$$\Delta t_{calc}^{n} \;:\; \Delta t_{calc}^{n} - \Delta t^n = 0 \tag{58}$$

$$u_s \;:\; \frac{\rho_s^{A,n} - \rho_s^{A,n-1}}{\Delta t^n}\frac{A\Delta X_{bl}^{A}}{2} + A\rho_*^{A,n}\left(u_s^{S,n} - u_*^{A,n}\right) - A\sum_k M_k S_k^{A,n} = 0 \tag{59}$$

$$u_*^{A,n} \;:\; u_*^{A,n} = 0 \tag{60}$$

$$n_{k,s}^{A,n} \;:\; \left(\frac{n_{k,s}^{A,n} - n_{k,s}^{A,n-1}}{1}\right) + \left(u_*^S - u_*^A\right)c_{k,*}^{A,n}\Delta t^n \textbf{ - } \boldsymbol{i}\bullet\boldsymbol{J}_{x,k,*}^{A,n} A\Delta t^n - S_{A,k}^{S}\Delta t^n A = 0 \tag{61}$$

$$n_{o,s}^{A,n} \;:\; \sum n_{k,s}^{A,n} = \frac{\Delta L_{BL}^{n}}{2} A\bar{V}_s^{A,n} \tag{62}$$

The B phase control volumes are represented by Eqns. (63) to (65).

$$u_*^{B,n} \;:\; \frac{\rho_s^{B,n} - \rho_s^{B,n-1}}{\Delta t^n}\frac{A\Delta L_{bl}^{B}}{2} - A\rho_*^{B,n}\left(u_s^{S,n} - u_*^{B,n}\right) - A\sum_k M_k S_k^{B,n} = 0 \tag{63}$$

$$n_{k,s}^{B,n}: \quad \left(\frac{n_{k,s}^{B,n}-n_{k,s}^{B,n-1}}{1}\right)-\left(u_*^S-u_*^B\right)c_{k,*}^{B,n}\Delta t^n \text{ - } \boldsymbol{i}\bullet\boldsymbol{J}_{x,k,*}^{B,n}A\Delta t^n - S_{A,k}^S\Delta t^n A = 0 \tag{64}$$

$$n_{o,s}^{B,n}: \quad \sum n_{k,s}^{B,n} = \frac{\Delta L_{BL}^B}{2}A\bar{V}_s^{B,n} \tag{65}$$

We have assigned the relative velocity of zero to the left of the A control volume.

Let us take a look at Eqn. (59). ΔL_{bl}^A is the boundary layer thickness on the A side of the interface. ΔL_{bl}^A is assumed to be constant. The Eqn. (59) is an expression of the mass balance in the ½ of that adjacent to the interface. $\rho_s^{A,n}$ is the density of phase A at the interface. $\rho_*^{A,n}$ is the density of phase A ½ through the boundary layer. $u_{x,s}^A$ is the velocity of phase A at the interface. We apply a first order upwinding scheme for the value of $\rho_s^{A,n}$ and all other variables of that kind at the control volume interfaces:

$$\rho_*^{A,n} = \begin{cases} \rho_s^{A,n} & ; u_s^{S,n}-u_*^{A,n} > 0 \\ \rho_{BULK}^{A,n} & ; u_s^{S,n}-u_*^{A,n} < 0 \end{cases} \tag{66}$$

A similar expression is done for phase B control volume quantities

$$\rho_*^{B,n} = \begin{cases} \rho_s^{B,n} & ; u_s^{S,n}-u_*^{B,n} < 0 \\ \rho_{BULK}^{B,n} & ; u_s^{S,n}-u_*^{B,n} > 0 \end{cases} \tag{67}$$

Model 2 has been used to create simulations of the kinetic relaxation of the organic TBP and aqueous brine system as a function of pH using a continuous stirred tank reactor (CSTR) approximation for the bulk constituents.

7.2.5.3 Model 3

In Model 3, we add back the axial momentum equation. Doing this, we add in the pressure unknowns and change the associations of independent variables with conservation equations. With this in mind the full equation set becomes Eqns. (68) to (79). This model has not been implemented yet, as there doesn't seem to be a programmatic driver yet; Model 2 is sufficient and robust for the cases that we have carried out on the aqueous brine, TBP system.

$$P_s^A: \quad \frac{\rho_s^{A,n}-\rho_s^{A,n-1}}{\Delta t^n}\frac{\Delta L_{bl}^A}{2} - \left(\left(-i\right)\bullet\rho_*^{A,n}u_*^{A,n}\right) - \rho_*^{A,n}u^{ref} - i\bullet\rho_s^A\left(u_s^{A,n}-u_s^{s,n}\right) = 0 \tag{68}$$

$$u_s^{S,n}\ :\ \rho_*^A\left(\frac{u_*^{A,n}-u_*^{A,n-1}}{\Delta t^n}\right)-\rho_*^A\left(\frac{u^{ref,n}-u^{ref,n-1}}{\Delta t^n}\right)+\rho_*^A u_*^{A,n}\frac{u_s^{A,n}-u_{BULK}^{A,n}}{\Delta L_{BL}^{A,n}}+\frac{1}{\Delta L_{BL}^{A,n}}\left(\boldsymbol{n}_A\bullet\underline{\underline{\boldsymbol{T}}}^{A,S}\bullet\boldsymbol{n}_A-\boldsymbol{n}_A\bullet\underline{\underline{\boldsymbol{T}}}^{B,BULK}\bullet\boldsymbol{n}_A\right)=0 \tag{69}$$

$$u_*^{A,n}\ :\ u_*^{A,n}=0 \tag{70}$$

$$n_{k,s}^{A,n}\ :\ \frac{\Delta L_{BL}^n}{2}\left(\frac{Y_{k,s}^{A,n}\rho_s^A-Y_{k,s}^{A,n-1}\rho_s^{A,n-1}}{\Delta t^n}\right)-\left(\left(-i\right)\bullet\rho_*^A u_*^A Y_{k,*}^{A,n}\right)-\rho_*^A u^{ref}Y_{k,*}^{A,n}-\boldsymbol{i}\bullet\boldsymbol{j}_{x,k,*}^{A,n}-i\bullet\rho_s^A\left(u_s^A-u_s^s\right)Y_{k,s}^{A,n})=0 \tag{71}$$

$$n_{0,s}^{A,n}\ :\ \sum n_{k,s}^{A,n}=\frac{\Delta L_{BL}^n}{2}A\bar{V}_s^{A,n} \tag{72}$$

$$u_{BULK}^{A,n}\ :\ \frac{\rho_{BULK}^{A,n}-\rho_{BULK}^{A,n-1}}{\Delta t^n}\frac{\Delta L_{bl}^A}{2}+\left(\rho_*^{A,n}u_*^{A,n}-\rho_{BULK}^{A,n}u_{x,BULK}^A\right)+\rho_{BULK}^{A,n}u^{ref,n}=0 \tag{73}$$

$$P_s^B\ :\ \frac{\rho_s^{B,n}-\rho_s^{B,n-1}}{\Delta t^n}\frac{A\Delta L_{bl}^B}{2}-A\rho_*^{B,n}\left(u_s^{S,n}-u_*^{B,n}\right)-A\sum_k M_k S_k^{B,n}=0 \tag{74}$$

$$u_*^{B,n}\ :\ \rho^B\left(\frac{u_*^{B,n}-u_*^{B,n-1}}{\Delta t^n}\right)-\rho_*^B\left(\frac{u^{ref,n}-u^{ref,n-1}}{\Delta t^n}\right)+\rho^B u_x^B\frac{u_s^{B,n}-u_o^{B,n}}{\Delta L_{BL}^n}+\boldsymbol{n}_B\bullet\underline{\underline{\boldsymbol{T}}}^{B,S}\bullet\boldsymbol{n}_B-\boldsymbol{n}_B\bullet\underline{\underline{\boldsymbol{T}}}^{B,0}\bullet\boldsymbol{n}_B=0 \tag{75}$$

$$u_{BULK}^{B,n}\ :\ \frac{\rho_{BULK}^{B,n}-\rho_{BULK}^{B,n-1}}{\Delta t^n}\frac{\Delta L_{bl}^B}{2}+\left(\rho_*^{B,n}u_*^{B,n}-\rho_{BULK}^{B,n}u_{BULK}^{B,n}\right)+\rho_{BULK}^{B,n}u^{ref,n}=0 \tag{76}$$

$$n_{k,s}^{B,n}\ :\ \frac{\Delta L_{BL}^n}{2}\left(\frac{Y_{k,s}^{B,n}\rho_s^B-Y_{k,s}^{B,n-1}\rho_s^{B,n-1}}{\Delta t^n}\right)-\left(\left(-i\right)\bullet\rho_*^B u_*^B Y_{k,*}^{B,n}\right)-\rho_*^A u^{ref}Y_{k,*}^{B,n}-\boldsymbol{i}\bullet\boldsymbol{j}_{x,k,*}^{B,n}-i\bullet\rho_s^B\left(u_s^B-u_s^s\right)Y_{k,s}^{B,n})=0 \tag{77}$$

$$n_{0,s}^{B,n}\ :\ \sum n_{k,s}^{B,n}=\frac{\Delta L_{BL}^n}{2}A\bar{V}_s^{B,n} \tag{78}$$

We also have the following tie condition, which associates the pressures on each side of the interface; they are not independent.

$$P_s^B\qquad \boldsymbol{n}_A\bullet\underline{\underline{\boldsymbol{T}}}^{A,S}\bullet\boldsymbol{n}_A=\boldsymbol{n}_A\bullet\underline{\underline{\boldsymbol{T}}}^{B,S}\bullet\boldsymbol{n}_A+2H\sigma \tag{79}$$

7.2.6 Conclusions

Several models have been presented for incorporating thermodynamic models from Cantera into a computational fluid dynamics framework.

8 POPULATION BALANCE MODELING OF DROPLET SIZE DISTRIBUTION IN A CENTRIFUGAL CONTACTOR

A theoretical study was developed for the evolution of a drop size distribution in an emulsion under conditions where drop breakup dominates drop coalescence. Previous experiments and numerical simulations demonstrate that the size of daughter drops produced by breakup in a particular fluctuation, scale with the critical size drop for the fluctuation. The volume of the parent drop only determines the number of daughter drops produced by the breakup event. A simplified population balance model predicated on this observation was developed. The essential simplification involves the replacement of the usual two-variable daughter-drop distribution function by a single-variable distribution that describes the volume of daughter drop relative to the critical size drop. The resulting model equations were analyzed and a long-time similarity formulation was derived. Analytical formulas were derived for certain limiting cases and a complete set of numerical results were obtained for a wide range of parameter values. Experiments in the literature strongly support our new drop breakup model. In our first section, we only summarize this work as a proceedings paper was published [Loewenberg and Rao, 2011] and a journal article has been submitted to Chemical Engineering Science [Loewenberg and Rao, 2012].

In the next section, we discuss how knowledge of droplet-size distribution can be used to predict separation efficiencies in a centrifugal contactor.

8.1 Droplet size distributions

8.1.1 Introduction

Population balance modeling is used to describe the evolution of dispersed-phase particles in a wide range of engineering applications including liquid-liquid extraction, emulsification, polymer blending, emulsion polymerization, grinding and pulverizing operations, crystallization, and aerosols. Typically, particles of the dispersed phase grow by coalescence or flocculation or diminish in size by breakup.

In some situations, such as in grinding operations, particle breakage inherently dominates particle aggregation regardless of the dispersed-phase volume fraction. In other situations, particle growth dominates breakage, such as the growth of Brownian particles by flocculation under quiescent conditions.

In fluid-fluid systems, weak flows favor drop coalescence, whereas strong flows favor breakup. This is because drop deformation is necessary for breakup but deformation strongly hinders drop coalescence. Some processes involve both weak and strong flow regions that are physically separated with drop growth by coalescence occurring in the weak-flow region and breakup occurring in the strong-flow region. For example, in liquid-liquid extraction two fluid phases are emulsified together in a strong flow to enhance mass transport, and then subjected to a gentle flow that promotes drop coalescence and thus phase separation [Mohanty, 2000]. Centrifugal contactors have a high-shear “mixing zone” in the gap formed between the rotor and the housing

where drop breakup dominates and a “separation zone” inside of the rotor where rigid-body rotation drives buoyancy-driven drop coalescence [Leonard, 1988; Wardle et al., 2006].

In our study, we considered the evolution of a drop size distribution by breakup under strong-flow conditions (e.g. mixing zone of a centrifugal contactor) where drop coalescence has a negligible impact on the evolution. Under these conditions, the drop size distribution evolves according to the Smoluchowski-type population balance equation,

$$\frac{\delta}{\delta x} n(v,t) = p(v,t) - r(v)n(v,t) \tag{80}$$

where terms describing drop coalescence have been omitted. Here, n(v, t) is the number density of drops with volume v at time t, r(v) is the breakup rate, and p(v, t) is the drop production rate defined by

$$p(v,t) = \int_{v}^{\infty} G(v,v_1) r(v_1) n(v_1,t) dv_1 \tag{81}$$

The daughter-drop distribution function $G(v, v_1)$ gives the number of daughter drops with volume v produced by the breakup of a parent drop with volume v_1. An initial drop size distribution is needed to fully specify the problem.

Equations (75-76) define a well-posed (linear) initial value problem for $n(v, t)$ that relies on models on models for the drop breakup rate, $r(v)$, and daughter drop distribution function. A power-law is commonly used to describe the breakup rate under the assumption of scale invariance. This is a reasonable assumption in the absence of an intrinsic length scale that sets the minimum attainable drop size.

However, a much more significant challenge lies in the determination of reliable models for the daughter drop distribution function. The development of models to describe the daughter drop distribution function is intrinsically challenging because of its dependence on both the parent and daughter drop volumes. Various coarse-grain models have been formulated based on a simplified picture of the drop breakup microphysics [Vankova et al., 2007; Raikar et al., 2007], and various procedures have been proposed for solving the inverse problem of deriving the daughter drop distribution from experimental data [Kostoglou and Karabelas, 2005; Raikar et al., 2006, Sathyagal et al.,1995]. However, the coarse-grain models are inevitably over-simplified and ad hoc assumptions are required to regularize the otherwise, ill-posed inverse problem. Despite considerable effort, reliable models for the daughter drop distribution function are unavailable.

A persistent feature of the previously proposed models for the daughter drop distribution function is the assumption that the volume of daughter drops produced by a breakup event scale with the volume of the parent drop, as illustrated by the sketch in Figure 71b. In our study, we developed a new model for the drop production rate, $p(v, t)$, based on the observation that the size of daughter drops produced by breakup in a given fluctuation scale with the “critical-size” drop– the largest drop that can survive the fluctuation without breaking. The sketch in Figure 71b

illustrates the idea. Accordingly, the volume of a parent drop determines the number of daughter drops but not their volumes (or distribution of their volumes). This scaling is supported by classical experimental studies on drop breakup in turbulent flows [Pilch and Edrman, 1978], and by more recent experiments and simulations on drop breakup [Cristini *et al.*, 2003].

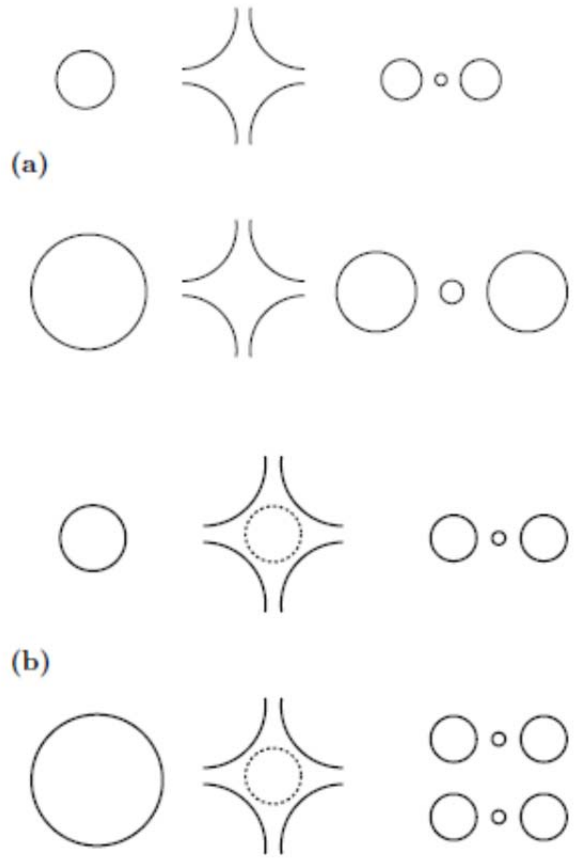

Figure 71. Scaling of daughter drops; (a) proportional to the parent drop: larger parent drop produces the same number of proportionally larger daughters; (b) proportional to the critical size drop (dashed curve): larger parent drop produces proportionally more daughters with the same size.

8.1.2 Simplified Formulation

In our analysis, we showed that the proposed daughter drop scaling described above and illustrated in Figure 71b leads to the new daughter drop production term,

$$p(v,t) = v^{-1}\int_0^1 g(s)\frac{dr(v/s)}{dv}M_1(v/s,t)ds \ , \tag{82}$$

in the original population balance equation (80). Here, g(s) is the rescaled daughter drop distribution function that describes the distribution of daughter drops with volume sv_* ($0 < s \leq 1$), where v_* is the critical drop volume for a given fluctuation.

The derivative of the breakup rate in equation (82), $dr(v/s)/dv$, is the frequency of fluctuations corresponding to a critical drop volume v/s, and the quantity $M_1(v/s, t)$ represents the dispersed-phase volume associated with drops that have volume $v' \geq v/s$. A fluctuation corresponding to a critical size v/s will break any drop with volume $v' \geq v/s$ to produce daughters with volume v.

The simplified drop production term (82) involves a much simpler one-variable daughter drop distribution function in place of the two-variable distribution function that enters the usual drop production term (81).

8.1.3 Evolution of the Drop Size Distribution

According to the simplified model described above, the evolution of the drop size distribution is described by equations (80) and (82), and an initial drop size distribution.

We consider the case of a power-law breakup rate,

$$r(v) = k_0 v^a \tag{83}$$

where the pre-factor k_o and exponent $a > 0$ are arbitrary constants. The existence of a minimum attainable drop size is ignored, at least on the time scale of interest [Lam, 1996].

Numerical results were obtained by discretizing equations (1) and (3) using logarithmically spaced points v_i ($i = 1, 2, \ldots, N$) to yield a system of ordinary differential equations for $n_i(t) = n(v_i, t)$ ($i = 1, 2, \ldots, N$) that were integrated in time starting from a prescribed initial distribution. A piecewise linear representation of n(v, t) was used to evaluate the volume integral in equation (83). An example from our numerical results is presented below.

8.1.4 Long-time similarity formulation

At long times compared to the time required for decay of the initial drop size distribution, we show that the drop size distribution attains a universal self-similar form (i.e., independent of the initial conditions) in terms of the variables,

$$\begin{aligned} n(v,t) &= aV_o v^{-2} h(\eta) \\ \eta &= k_o v^a t \end{aligned} \tag{84}$$

where V_0 is the volume of the dispersed phase fluid

The universal distribution is governed by an integral equation that is derived by recasting equations (80) and (82) in terms of the similarity variables (84). Numerical results were obtained

by solving the resulting integral equation using a piecewise linear representation of h(η) and solving the discretized linear equations.

8.1.5 Analytical results for a monodisperse daughter drop distribution

We obtained analytical results for the case of a monodisperse daughter drop distribution,

$$g(s) = \delta(s - b), \quad 0<b \leq 1. \tag{85}$$

Under these conditions, the daughter drops produced by a breakup event are a fixed fraction b of the critical size drop for a given fluctuation.

We obtained a complete, exact solution for the special case where the daughter drops are exactly equal to the critical size drop, i.e., b = 1. The resulting formula demonstrates that the exact solution relaxes to a long-time, self-similar distribution on the time scale required for decay of the initial drop size distribution.

We showed that the long-time drop size distribution depends only on the combined parameter, $c = b^{-a}$, and we obtained an asymptotic solution of the long-time self-similar distribution for $c \gg 1$.

8.1.6 Numerical results

The predictions of our new model were parametrically explored. An example of our numerical simulations is presented in Figure 72. The figures show the cumulative fraction of the dispersed phase fluid. This shows that the long-time regime is quickly attained on the time scale for the decay of the initial drop size distribution, i.e., the long-time similarity solution accurately describes the drop size distribution when the similarity variable is greater than 4.

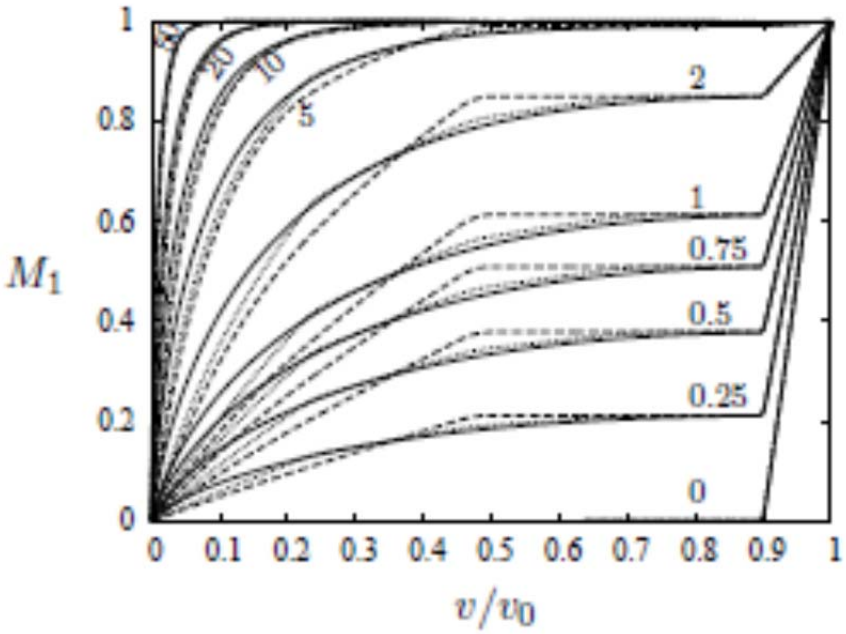

Figure 72. Evolution of drop size distributions for monodisperse (dashed line), trimodal (dotted line), and uniform daughter distribution (solid line).

Figure 73 shows a rescaled version of Figure 72 that shows how the solution collapses to one curve when plotted with respect to the similarity variable, η.

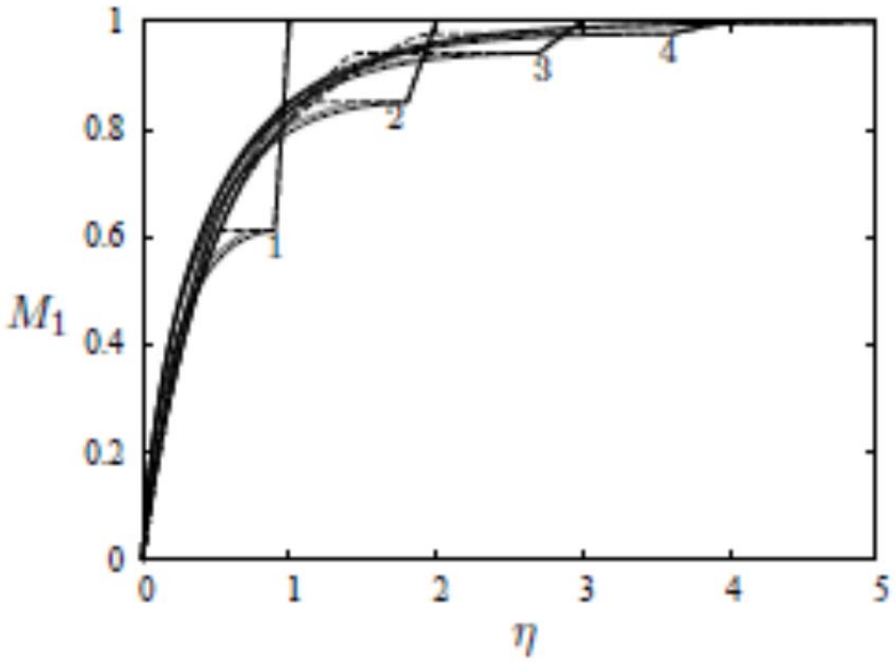

Figure 73. Same as previous figure but rescaled in terms of similarity variables; similarity solution corresponding to each daughter drop distribution function (thick curves).

8.1.7 Comparison to experimental measurements

The experiments of Lam *et. al.* [1996] provide an ideal test of the simplified model that we propose. Their experiments were performed under conditions where drop breakup dominates coalescence and the system was observed for very long times, as seen in Figure 74a.
Their results attain the predicted self-similar form. Solutions of the long-time formulation, agree closely with the experimental results, supporting the simplified model. However, the results are insensitive to the detailed daughter drop distribution function, g(s), as demonstrated by the results depicted in parts (b) and (c) of Figure 74, where monodisperse and bidisperse daughter drop distributions are seen to describe the data equally well. This finding suggests that the inverse problem of determining the daughter drop distribution function from experimental data on drop-size distribution is badly posed and must be determined some other way.

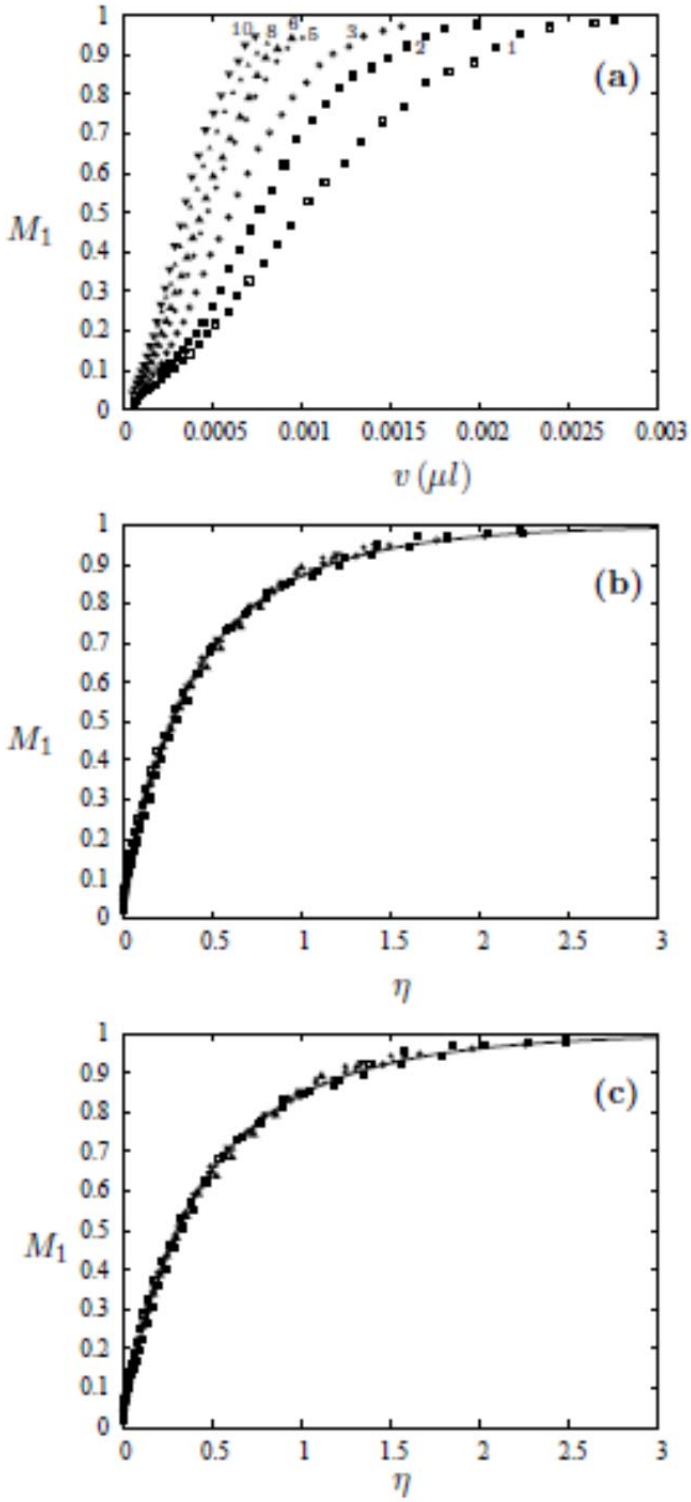

Figure 74. Experimental drop size distributions for 0.6% benzene-carbontetrachloride in water emulsion from Lam et. al. [1996] in unscaled variables corresponding to time as indicated in hours (a) and in similarity variables using power-law exponent a = 2.1 (b) and

(c); similarity solutions (solid curves) for monodisperse daughter drop distribution and bidisperse drop size distribution, respectively.

8.1.8 Conclusions

A simplified population balance model has been developed for the evolution of the drop size distribution in a liquid-liquid system by drop breakup. The new model is based on the observation that the size of daughter drops produced during a breakup event depends primarily on the strength of the fluctuation in the flow that causes the event. Daughter drops thus scale with the critical size drop for the fluctuation. Ultimately, this observation allows the two-variable daughter drop size distribution in the classical formulation of the problem to be approximately replaced by a one-variable distribution function that relates the size of daughter drops produced by a breakup event to the critical size drop for that fluctuation. Given the difficulty of developing reliable models for the two-variable distribution function, this simplification should advance efforts to model the evolution of the drop size distribution in liquid-liquid systems.

The resulting model equations were analyzed and a long-time similarity formulation was derived. Analytical formulas were derived for the case where the daughter drops produced by breakup are a fixed fraction of the critical size drop for a particular fluctuation and numerical results were obtained for a wide range of parameter values. Experiments in the literature strongly support our new drop breakup model. Good agreement between the model predictions and experiments is obtained but the predictions are insensitive to the details of the daughter drop distribution function. Therefore, the inverse problem of using experiments to determine the daughter drop distribution function is badly posed.

8.2 Mass transport

In the previous section, we developed a new population balance model for the evolution of a drop size distribution by breakup under strong-flow conditions, i.e., in the mixing zone of a centrifugal contactor, where drop coalescence has a negligible impact on the evolution. Our new model for the drop production rate is based on the observation that the size of daughter drops produced by breakup in a given fluctuation scale with the “critical-size” drop– the largest drop that can survive the fluctuation without breaking, rather than the size of the breaking parent drop as assumed in all previously proposed models. Accordingly, the volume of a parent drop determines the number of daughter drops but not their volumes. This scaling is supported by experimental studies and numerical simulations. Here, we describe a new population balance model to describe mass transport in the mixing zone of a liquid-liquid contactor.

8.2.1 Evolution of solute distribution

We propose a one-way coupling whereby solute transport is affected by the evolution of the drop size distribution but solute transport does not affect the evolution of the drop size distribution which is governed by the equations presented in the previous section. Accordingly, the population balance equation for the evolution of solute among the dispersed phase drops at steady-state is given by

$$\langle u_z \rangle [\frac{\partial}{\partial z} n(v,c,t) + A(v)\, j(c,C) \frac{\partial}{\partial c} n(v,c,t)] = p(v,c,t) - r(v) n(v,c,t) \ , \qquad (86)$$

where $n(v, c, z)$ is the number density of drops with volume v and volume averaged solute concentration c at position z in the mixing zone. Here, $z = 0$ corresponds to the inlet of the mixing zone, $z = L$ is the end of the mixing zone, and $\langle u_z \rangle$ is the mean velocity of the two-phase mixture in the z-direction. The mean velocity is related the total volume flow through the contactor divided by the cross-sectional area of the mixing zone, $\pi(R_o^2 - R_i^2)$, where R_o and R_i are, respectively, the outer and inner radii of the device.

Mass transport in the coalescence-dominated separation zone of the contactor is neglected. The drop production term $p(v, c, t)$ in equation (80) is given by the quantity $M_1(v/s, c, t)$, which represents the dispersed-phase volume associated with drops that have volume $v' \geq v/s$ and average solute concentration c.

The term $j(c,C)$ in equation (86) represents the solute flux from the bulk phase to a drop with solute concentration c. The quantity $A(v) = d_0\, v^{-1/3}$ is the area/volume for a drop of volume v where d_0 is a constant which we shall take as $d_0 = (36\pi)^{1/3}$ by considering spherical drops. A reasonable constitutive model for the flux is given by:

$$j(c,C) = k(HC - c) \qquad (87)$$

where $C(z)$ is the average solute concentration in the bulk phase, H is the equilibrium partition coefficient for the solute between the two phases, and k is the effective mass transport coefficient.

The average bulk-phase solute concentration that enters the drop flux model (87) is obtained by the conservation constraint

$$(1-\phi) C(z) + \phi \langle c \rangle (z) = (1-\phi) C_o + \phi c_o \qquad (88)$$

where ϕ is the dispersed-phase volume fraction, C_0 and c_0 are, respectively, the solute concentrations in the bulk and dispersed phases entering the contactor, and $\langle c \rangle (z)$ is the average solute concentration in the dispersed phase at a location z in the mixing zone of the contactor,

$$\phi \langle c \rangle (z) = \int_0^\infty [\int_0^\infty n(v,c,z) c\, dc] v\, dv \ . \qquad (89)$$

8.2.2 Contactor performance

The total mass transfer, J, in the contactor is given by

$$J = \phi(\langle c \rangle (L) - c_o) \ , \qquad (90)$$

where $\langle c \rangle(L)$ is the average solute concentration in the dispersed phase at the exit of the mixing zone of the contactor. Under the assumption that negligible mass transfer occurs in the separation zone of the contactor, $\langle c \rangle(L)$ is approximately equal to the solute concentration in the dispersed phase fluid flowing out of the contactor.

The maximum possible mass transfer, J_0, in a contactor is associated with thermodynamic equilibrium, i.e., $\langle c \rangle(L) = HC(L)$. When inserted into equation (90), we obtain

$$J_o = \frac{\phi(1-\phi)}{1+\phi(H-1)}(HC_o - c_o) \tag{91}$$

We thus define the stage efficiency of a centrifugal contactor as

$$e = \frac{J}{J_o} = \frac{1+\phi(H-1)}{1-\phi}\frac{\langle c \rangle(L) - c_o}{HC_o - c_o} \tag{92}$$

8.2.3 Approximate Model

Here we present an approximate model that accounts for the evolution of interfacial area in the system but neglects the solute concentration history resulting from formation of drops with volume v and solute concentration c by the breakup of larger drops with volume v′ > v and c′ = c. Accordingly, we write the approximate macroscopic equation describing interphase mass transport in the system

$$\langle u \rangle \frac{d}{dx}\langle c \rangle(z) = kA'(z)(C(z) - \langle c \rangle(z)) \tag{93}$$

where A’ is the specific interfacial area (area per unit volume) in the system.

In the simplest case, we estimate the average interfacial area in the mixing zone as a constant value,

$$A'(z) \approx A_o' = d_o \phi v_o^{-1/3} \tag{94}$$

where v_0 is a characteristic drop volume, *e.g.*, average size in the mixing zone of the contactor. A more detailed model that takes account of the evolving interfacial area is given by

$$A'(z) = A_o' \, f[h] \frac{3a}{1+3a}\left(\frac{k_o v_o^a z}{\langle u_z \rangle}\right)^{1/3a} \tag{95}$$

where k_0 and a are the rate parameters Here, f [h] is an integral of the long-time self-similar drop size distribution, which depends on the rescaled daughter drop distribution and the power-law a; *e.g.*, for critical size daughter drops, f [h] = Γ(1 − 1/3a).

Integrating equation (93) with the constraint (88), we obtain

$$e = 1 - \exp(-d_o \phi \frac{1+\phi(H-1)}{1-\phi} \frac{kLv_o^{-1/3}}{\langle u_z \rangle}) \tag{96}$$

using the constant interfacial area estimate (94). The result predicts exponential efficiency with respect to the length of the mixing zone, L. Using the evolving interfacial area (95), we find

$$e = 1 - \exp(-d_o \phi \frac{1+\phi(H-1)}{1-\phi} \frac{kLv_o^{-1/3}}{\langle u_z \rangle} (\frac{k_o v_o^a L}{\langle u_z \rangle})^{1/3a}) \tag{97}$$

which indicates a stronger, super-exponential dependence of the contactor efficiency on the length of the mixing zone.

9 ANALYSIS OF A CASCADE OF CENTRIFUGAL CONTACTORS

Banks of centrifugal contactors are used for nuclear waste reprocessing, with each contactor representing a “stage” in the separation. Contact times are short and contactor sizes are small to keep the material from going critical. Here, the performance of a cascade of centrifugal contactors is analyzed. It is shown that the evolving interfacial area developed in the previous chapter can be incorporated by using an appropriate average. The unrecovered solute diminishes exponentially with the number of stages used in the cascade with an exponent that depends on the residence time of the contactors.

Here, we analyze the performance of a cascade of centrifugal contactors using our predictions for the evolution of the drop size distribution in the mixing zone of a contactor.

9.1 Formulation

The mass flows of the aqueous and solvent phases are denoted ***F*** and ***S*** respectively. In our analysis, these two fluids are assumed to be immiscible. Solute concentrations are given in terms of mass ratios, i.e., mass of solute per mass of solute-free aqueous phase, ***X,*** and mass of solute per mass of solute-free solvent, ***S***. Accordingly, the solute balance on the nth contactor in a cascade of contactors (n = 1, 2, … , N) is given by:

$$FX^{(n-1)} + SY^{(n+1)} = FX^{(n)} + SY^{(n)} \tag{98}$$

The flows into and out of a single contactor are shown schematically in Figure 75.

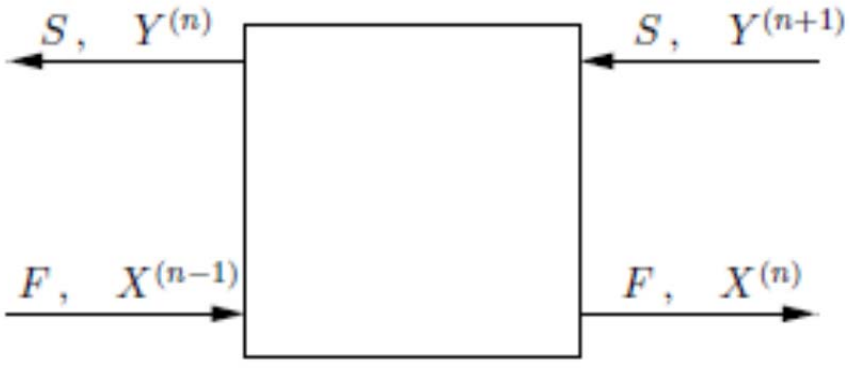

Figure 75. 1. The nth stage (n = 1, 2, · · · ,N) of an N-contactor cascade showing the aqueous *F* and solvent *S* flows into and out of the stage and solute mass ratios in each of the streams.

9.1.1 Stage-wise calculations: Interphase mass transport

We consider the mass transport within a contactor for two limiting cases of the conditions in the mixing zone of the contactor:(1) well mixed conditions where the elapsed time spent by a differential volume of the two-phase mixture in the mixing zone is uncorrelated with its position (i.e., stirred tank conditions), and (2) the case where the elapsed time spent by a differential volume of the two-phase mixture in the mixing zone is determined by its position. (i.e., plug flow conditions). Case (1) describes the conditions in a well stirred vessel whereas case (2) may be is a reasonable description for a narrow-gap centrifugal contactor because mixing along the length of the narrow annular region is suppressed.

As shown below, we obtain

$$Y^{(n)}(\overline{T}) = \frac{1}{1+E}(E+1-\eta(\overline{T}))Y^{(n+1)} + \frac{H'}{1+E}(\eta(\overline{T}))X^{(n-1)} \ , \tag{99}$$

$$X^{(n)}(\overline{T}) = \frac{1}{H'}\frac{E}{1+E}(\eta(\overline{T}))Y^{(n+1)} + \frac{1}{1+E}(1+E-E\eta(\overline{T}))X^{(n-1)} \ , \tag{100}$$

where $\eta(\overline{T})$ is the regime-dependent stage efficiency function:

$$\eta(\overline{T}) = \frac{\overline{T}}{1+\overline{T}}, \text{ stirred tank regime} \tag{101}$$

and

$$\eta(\overline{T}) = 1-e^{-\overline{T}}, \text{ plug flow regime.} \tag{102}$$

The extraction factor, E, is defined as

$$E = H'S/F \ , \tag{103}$$

where H′ is the equilibrium partition coefficient for the solute defined in terms of mass ratios. $\overline{T}$ is the dimensionless residence time of the mixing zone in each contactor,

$$\overline{T} = (1+E)kA_0T \ , \tag{104}$$

Where k is the interphase mass transport coefficient and A_0 is the volume-averaged interfacial area between the aqueous and solvent phases per unit volume of the two-phase mixture.

The stage efficiency, η, is defined by the fractional approach to an equilibrium solute distribution between the aqueous and solvent phases at the outlet of each contactor, *i.e.*,

$$\eta = \frac{Y^{(n)} - Y^{(n+1)}}{Y_*^{(n)} - Y^{(n+1)}}, \; Y_*^{(n)} = \frac{H' X^{(n-1)} + EY^{(n+1)}}{1+E} \tag{105}$$

Where is the solute concentration in the solvent phase at the outlet of an equilibrium stage. In general, stage efficiencies lie in the range $0 \leq \eta \leq 1$ where the limiting values correspond, respectively, to short and long residence times, i.e., $\eta(0) = 0$ and $\eta(\infty) = 1$, consistent with formulas (102)-(103), for the stirred-tank and plug-flow regimes, respectively. According to equations (100)-(101), an equilibrium distribution of solute is attained for long residence times, $\lim \eta \to 1 \; Y(n)/X(n) = H'$, and no solute exchange occurs between the aqueous and solvent phases (i.e., $Y^{(n)} = Y^{(n+1)}, X^{(n)} = X^{(n-1)}$) for $\eta \to 0$.

9.1.1.1 Stirred-tank regime

In this regime, interphase mass transport is described by the stirred tank equation

$$Y^{(n)} = Y^{(n+1)} + kA_0 T[H' X^{(n)} - Y^{(n)}] \; , \tag{106}$$

Solving equations (99) and (108), we obtain the solution (100)-(101) with stage efficiency function (102).

9.1.1.2 Plug-flow regime

In the plug-flow regime, interphase mass transport is described by the evolution equation,

$$\frac{d}{dt} Y^{(n)}(t) = kA'(t)[H' X^{(n)}(t) - Y^{(n)}(t)] \; , \tag{107}$$

where k is the mass transport coefficient, H' is the equilibrium partition coefficient for the solute defined in terms of mass ratios, and $A'(t)$ is the evolving interfacial area between the aqueous and solvent phases per unit volume. Here, t is time in the mixing zone of the contactor with $t = 0$ corresponding to entry into the mixing zone of the contactor with initial conditions,

$$Y^{(n)}(0) = Y^{(n+1)}, \;\; X^{(n)}(0) = X^{(n-1)} \tag{108}$$

The quantity A(t) in equation (109) is the evolving interfacial area between the aqueous and solvent phases per unit volume.

Integrating the initial value problem (99), (109)-(110), we obtain

$$Y^{(n)}(t) = \frac{1}{1+E}[E + 1 - \eta(t)]Y^{(n+1)} + \frac{H'}{1+E}\eta(t) X^{(n-1)} \tag{109}$$

and

$$X^{(n)}(t) = \frac{1}{H'}\frac{E}{1+E}\eta(t)Y^{(n+1)} + \frac{1}{1+E}[1+E-E\eta(t)]X^{(n-1)}, \tag{110}$$

where

$$\eta(t) = 1 - \exp[-(1+E)k\int_0^t A'(t)dt'] \ . \tag{111}$$

The compositions at the outlet of the contactor, corresponding to $X^{(n)}(T)$ and $Y^{(n)}(T)$, are given by equations (100)-(101) with stage efficiency function (103). In this case, the average interfacial area A_0 used to define the mean residence time in equation (104) is given by the time-averaged quantity,

$$A_0 = \frac{1}{T}\int_0^T A'(t)dt \tag{112}$$

Given the assumption of plug flow, the time- and volume-averaged interfacial areas are equal. Thus, the outlet compositions depend only on the average interfacial area per unit volume, A0, not the details of its evolution.

The exit from the contactor corresponds to t = T where T = V/(F +S) is the residence time of the mixing zone in the contactor, and V is the volume of the mixing zone. Accordingly, the compositions of the streams leaving the contactor shown in figure 1 correspond to $X^{(n)}(T)$ and $Y^{(n)}(T)$.

9.2 Results for Cascade

Combining equations (100)-(101) provide a system of 2N difference equations for the solute concentrations in the aqueous and solvent streams in a cascade of N identical contactors. Pure solvent enters stage N, i.e., $Y^{(N+1)} = 0$, and the composition, $X^{(0)}$, of the aqueous stream entering stage 1 is prescribed.

Rearranging equations (100)-(101) we obtain a decoupled second-order difference equation for the solute concentrations, X(n), in the aqueous phase streams

$$X^{(n-2)} = (E+1)\frac{2-\eta}{1+E-E\eta}X^{(n-1)} - \frac{1+E-\eta}{1+E-E\eta}X^{(n)} \text{ for } 2 \le n \le N. \tag{113}$$

Given that $Y^{(N+1)} = 0$, we have

$$\frac{X^{(N-1)}}{X^{(N)}} = \frac{1}{E-1}\left[E\left(\frac{1+E-\eta}{1+E-E\eta}\right)-1\right] \tag{114}$$

according to equation (101). We can then solve equation (115) recursively for n = N −2,N − 3, . . . 0, obtaining

$$\frac{X^{(N-k)}}{X^{(N)}} = \frac{1}{E-1}\left[E\left(\frac{1+E-\eta}{1+E-E\eta}\right)^{k} - 1\right] \text{ for } 0 \le k \le N\,, \tag{115}$$

which we can re-express in terms of the prescribed solute concentration, $X^{(0)}$, of the aqueous stream entering the cascade,

$$\frac{X^{(n)}}{X^{(0)}} = \frac{E\left(\frac{1+E-\eta}{1+E-E\eta}\right)^{N-n} - 1}{E\left(\frac{1+E-\eta}{1+E-E\eta}\right)^{N} - 1} \quad \text{for } 0 \le n \le N\,, \tag{116}$$

From equations (100)-(101) we find

$$Y^{(n)} = \frac{H'}{E\eta}\left[(E+1)X^{(n-1)} - (1+E-E\eta)X^{(n-2)}\right], \tag{117}$$

which relates the solute concentrations in the solvent streams to the solute concentrations in the aqueous streams. Inserting equation (116) into (117), we have

$$\frac{Y^{(n)}}{X^{(0)}} = H'\frac{\left(\frac{1+E-\eta}{1+E-E\eta}\right)^{N-n+1} - 1}{E\left(\frac{1+E-\eta}{1+E-E\eta}\right)^{N} - 1} \quad \text{for } 0 \le n \le N\,, \tag{118}$$

This provides a complete solution to the system.

The fractional recovery R is defined by

$$R = \frac{S}{F}\frac{Y^{(1)}}{X^{(0)}} = 1 - \frac{X^{(N)}}{X^{(0)}} \tag{119}$$

Using equation (118), we thus obtain

$$R(E,\eta,N) = \frac{E\left(\frac{1+E-\eta}{1+E-E\eta}\right)^{N} - E}{E\left(\frac{1+E-\eta}{1+E-E\eta}\right)^{N} - 1}\,. \tag{120}$$

We note that

$$R(E^{-1},\eta,N) = E^{-1}R(E,\eta,N)\ . \tag{121}$$

For large N, equation (121) reduces to

$$1-R(E,\eta,N) = 1-E^{-1}R(E^{-1},\eta,N) = \frac{E-1}{E}\left(\frac{1+E-\eta}{1+E-E\eta}\right)^{-N}\ ,\quad \mathrm{N}\gg 1,\ \mathrm{E}>1 \tag{122}$$

indicating that for E > 1, the unrecovered solute fraction, 1−R, tends exponentially to zero with N, and that for E < 1, the recovered solute fraction tends exponentially to the limiting value R = E. For long residence times, $\eta \rightarrow 1$, formula (122) reduces to the classical result for equilibrium stages,

$$R(E,N) = \frac{E^{N+1}-E}{E^{N+1}-1}\ ,\ \eta=1. \tag{123}$$

Results for E = 2 (and for E = 1/2 by relation (123)) are shown in Figure 76 . The large N approximation (124) accurately captures the behavior for even a modest number of stages. Incomplete stage-wise solute equilibration between the aqueous and solvent phases, associated with lower stage efficiencies (i.e., shorter mixing zone residence times), are seen to reduce solute recovery. For a given residence time, $\overline{T}$, greater solute recovery is always attained under plug-flow, rather than stirred-tank conditions, according to formulas (102)-(103).

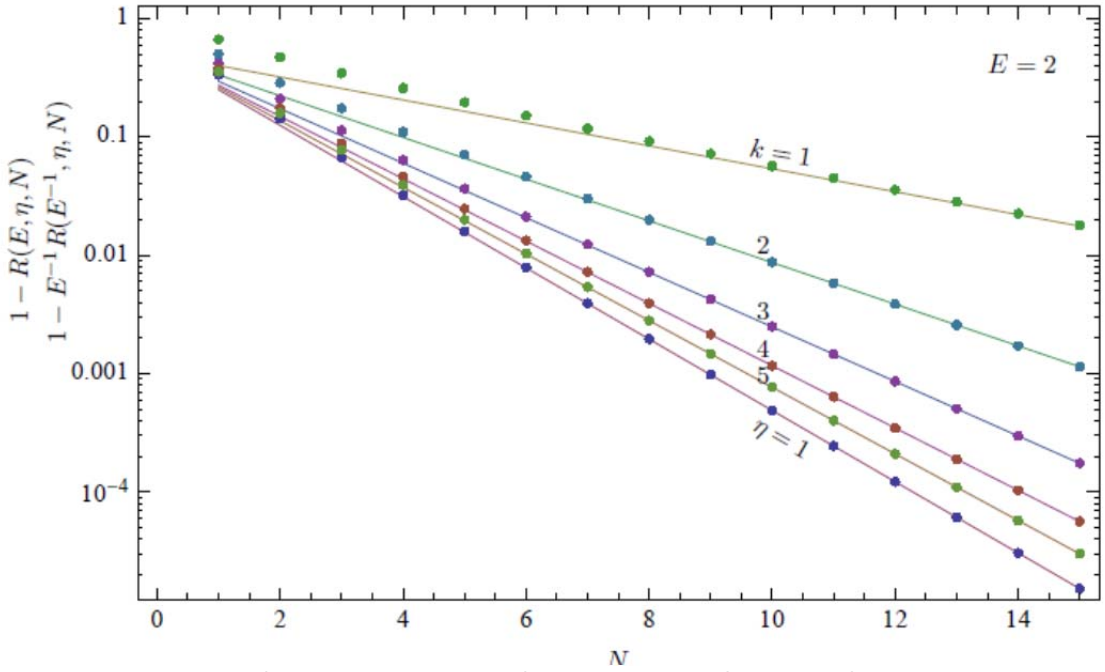

Figure 76. Decay of unrecovered solute fraction, 1−R, as function of contactor stages, N; extraction factor E = 2, residence time function $\eta = 1 - 2^{-k}$ for k as indicated in plot. Exact solution (dots), and limiting form for large N (lines).

10 CONCLUSIONS AND FUTURE WORK

10.1 Technical Accomplishments

We have made improvements to Sierra Mechanics, the engineering production code for the complex, for solid-fluid interactions and multiphase flows using our novel moving boundary algorithm termed conformal decomposition finite element method (CDFEM). One paper has been published on mesoscale particle dynamics in viscous fluids and another one is being completed on using CDFEM for capillary hydrodynamics. We have developed advanced thermodynamic methods in Cantera for uranyl transport from acid solution to the organic phase, which can predict distribution coefficients for various acid and tributyl phosphate concentrations. This work was published as a conference proceedings and SAND report and has just been accepted as a journal article. Novel centrifugal contactor experiments with quantitative measurement of three phases (water, organic drops, and air bubbles) have been developed, leading to a journal publication and collaboration with Argonne National Lab. We have developed microfluidic experiments to understand droplet-formation and internal flows for an aqueous-organic system. This resulted in one publication, and one journal article in preparation. We have developed a non-radioactive model system, based on neodymium and xylenol orange, with a new spectrophotometer to give quantitative mass transport data for the validation study. This system is used to study mass transport in both the droplet-scale microfluidic experiments and for contactor-scale experiments. Another journal article is being finalized on this work. A novel population balance kernel for drop break up has been developed and a publication is underway. Two other publications of related work were produced: one on drop coalescence and another on mold filling. Contactor models have been carried out for single phase turbulent flow and for two-phase flow without turbulence using a CVFEM/level-set. We have added experimental capabilities (high speed particle tracking in microfluidic devices, concentration determination with the spectrophotometer, high speed droplet size determination) that can be used to generate new projects.

We have produced 13 presentations, two invited posters, and seven invited seminars externally:

1. RR Rao, DR Noble et al, “Predicting Interfacial Mass Transport Using the Conformal Decomposition Finite Element Method ,” Finite Elements in Fluids, March, 2011
2. **Invited Talk** RR Rao et al, “Multiscale Models of Nuclear Waste Reprocessing,” Engineering Science External Panel Review, Sandia National Laboratories, Albuquerque, NM, April, 2011
3. RR Rao, DR Noble, MB Nemer, CR Roberts, HK Moffat, “Mass Transfer from a Buoyant Droplet Using the Conformal Decomposition Finite Element Method,” USNCCM11, July, 2011
4. DR Noble & MB Nemer, “A Dynamic Conformal Decomposition Finite Element Method (CDFEM) for Capillary Hydrodynamics,” USNCCM11, July, 2011
5. **Keynote**, M Loewenberg, RR Rao, 27th Annual Meeting of PPS, Morocco, May, 2011
6. CC Robert et al, “A microfocusing device for microscale mass transport studies,” AIChE Annual Meeting, Minneapolis MN, October, 2011

7. M Loewenberg & RR Rao, “A simplified model for the evolution of the drop size distribution and solute extraction in an emulsion under strong-flow conditions,” AIChE Annual Meeting, Minneapolis MN, October, 2011
8. TJ O’Hern, N. Wyatt, B. Shelden, “Determination of droplet and bubble size distribution in a centrifugal contactor,” AIChE Annual Meeting, Minneapolis MN, October, 2011
9. CC Robert et al, “Monodisperse droplet generation for microscale mass transport studies,” APS Division of Fluid Dynamics, Baltimore MD, November, 2011
10. SA Roberts, DR Noble, JB Lechman, “Spreading and wetting of impacting drops: Three-dimensional simulations using CDFEM,” APS Division of Fluid Dynamics, Baltimore MD, November, 2011
11. **Invited Talk**, RR Rao and DR Noble, “CDFEM modeling of microfluidic flows,” World Congress of Computational Mechanics, São Paulo, Brazil, Brazil, July 2012.
12. Wyatt et al., “Bubble and droplet size distributions in a centrifugal contactor,” AIChE Annual Meeting, Pittsburgh, PA, October 2012
13. CC Roberts et al., “Drop Circulation and Liquid-Liquid Extraction in Hele Shaw Flow,” AIChE Annual Meeting, Pittsburgh, PA, October 2012 (Poster)
14. M Loewenberg & RR Rao, “Population balance modeling of drop breakup in centrifugal contactors,” AIChE Annual Meeting, Pittsburgh, PA, October 2012

Other project metrics:

- **Invited Posters**:
  - LDRD Day, Albuquerque, NM, 2010;
  - NNSA TriLAB LDRD Symposium, Washington, DC 2011
- **Invited seminars**: Los Alamos National Laboratory (Rao, Noble); Proctor and Gamble (Rao), University of Maryland, University of New Mexico, Purdue, Tennessee Tech (Loewenberg)

Proceeding papers and journal articles that have been completed and submitted are listed below. We have two proceedings papers, two journal articles, one e-book chapter, and four papers submitted to journals.

- M Loewenberg, RR Rao, “A simplified model for the evolution of the drop size distribution in an emulsion under strong-flow conditions,” Proceedings of the 27th Annual Meeting of the PPS, Morocco, May, 2011
- CF Jove-Colon, HK Moffat, RR Rao, “Thermodynamic modeling of liquid-liquid extraction for the system TBP-HNO3-UO2(NO3)2-H2O-Diluent, Proceeding of the International High-Level Radioactive Waste Management Conference, Albuquerque, USA, April, 2011
- Featured Project, NNSA News, June 2011
- JB Lechman, MB Nemer, DR Noble, “Application of Conformal-Decomposition Finite Elements to Particle Suspensions,” *International Journal of Numerical Methods in Fluids, 2012*
- CR Roberts, RR Rao, M Loewenberg , CF Brooks, P. Galambos, AM Grillet, MB Nemer, “Comparison of monodisperse droplet generation from a flow-focusing device with hydrophilic or hydrophobic surfaces,” *Lab on a Chip*, 2012

- R.R. Rao, L.A. Mondy, T.A. Baer, D.R. Noble, C. F. Brooks, and M.M. Hopkins, "3D Numerical Modelling of Mold Filling," Invited eBook Chapter in "Numerical Modelling", InTech - Open Access Publisher, Rijeka, Croatia, 2012.
- CF Jove-Colon, HK Moffat, RR Rao, "Thermodynamic Modeling of Liquid-Liquid Extraction (LLE) Equilibria for the System TBP-HNO_3-UO_2-H_2O-Diluent: Applications of the Gibbs Energy Minimization (GEM) Approach to Complex LLE Systems," *SAND2012-9235*, Sandia National Laboratories, Albuquerque, NM, October 2012
- M. B. Nemer, P. Santoro, X. Chen, J. B Blawzdziewicz, M. Loewenberg, "Coalescence of drops with mobile interfaces in a quiescent fluid," accepted, *Journal of Fluid Mechanics*
- CF Jove-Colon, HK Moffat, RR Rao, "Thermodynamic modeling of liquid-liquid extraction," accepted, *Solvent Extraction and Ion Exchange*, 2012.
- M. Loewenberg and RR Rao, "A new breakage kernel for population balance modeling of emulsions," submitted, *Chemical Engineering Science*, 2012
- TJ O'Hern, N. Wyatt, B. Shelden, "Determination of droplet and bubble size distribution in a centrifugal contactor," submitted, *AIChE*, 2012

In addition, we are working to complete four or more manuscripts:

- CR Roberts, AM Grillet, MB Nemer, "A flow-focusing device for mass transport studies of rare earth complexes," *AIChE*, in preparation, 2012
- CR Roberts, SA Roberts, "Understanding internal flow for confined droplets: Experiments and modeling," *Physics of Fluids*, in preparation, 2012
- DR Noble, RR Rao, MB Nemer, "A dynamic conformal decomposition finite element model for capillary hydrodynamics, " *J Comp. Phys*, in preparation, 2012
- DR Noble, RR Rao, C.M. Brotherton, "Mass transport with the CDFEM method" *J Comp. Phys*, in preparation, 2012

10.2 Programmatic Accomplishment

In addition, our project sponsored two Minisymposia on CFD for Moving Boundary Problems (USNCCM11, FEF11), initiating a special issue of Computers & Fluids and finalizing a special issue of IJNMF, from a previous Minisymposium. This work supported Rekha Rao's nomination for the Asian-American Engineer of the Year Award, which she received in March, 2012. We have also established collaborations with Marianne Francois (LANL) for and Kent Wardle (ANL).

10.3 Conclusions and Future Work

We have developed and implemented novel computational methods in Sierra Mechanics our production engineering code. A new thermodynamics framework for separations was developed in Cantera. We have new experimental capabilities for microfluidics and separations. We have made scientific contributions to the literature and created environments for collaboration and advancements in CFD for moving boundary problems through our Minisymposia organization.

The nuclear weapons' program at SNL will benefit the most with new computational methods to help understand manufacturing processes, performance, and abnormal environments. Some applications that will benefit from this work include foam manufacturing, explosive property prediction, melting/decomposition in abnormal environments, and thermal batteries performance. For future work, we plan to continue our development of the CDFEM method for turbulent, two-phase flow with mass transport. Scalability is always an issue as we try to run realistic problems with millions of unknowns.

11 REFERENCES

Blair, D., and E. Dufresne. 2008. MATLAB Particle Tracking Routine. http://physics.georgetown.edu/matlab/.

R. A. Cairncross, P. R. Schunk, T. A. Baer, R. R. Rao, P. A. Sackinger, *A finite element method for free surface flows of incompressible fluids in three dimensions. Part 1. Boundary fitted mesh motion*, **International Journal for Numerical Methods in Fluids** 33 (2000) 375–403.

Calabrese, R. V, C. Y Wang, and N. P Bryner. 1986. "*Drop Breakup in Turbulent Stirred-tank Contactors. Part III: Correlations for Mean Size and Drop Size Distribution*." **AIChE Journal** 32 (4) (April 1): 677–681. doi:10.1002/aic.690320418.

Cauwenberg, Veerle, Jan Degrève, and Michael J. Slater. 1997. "*The Interaction of Solute Transfer, Contaminants and Drop Break-up in Rotating Disc Contactors: Part I. Correlation of Drop Breakage Probabilities*." **The Canadian Journal of Chemical Engineering** 75 (6): 1046–1055. doi:10.1002/cjce.5450750607.

Chan, P. C.-H., and L. G. Leal. 1979. "The Motion of a Deformable Drop in a Second-order Fluid." **Journal of Fluid Mechanics** 92 (01): 131–170. doi:10.1017/S0022112079000562.

Clift, R., J. R. Grace, and M. E. Weber. 1978. **Bubbles, Drops, and Particles**. New York, NY: Academic Press.

Cristini, Vittorio, and Yung-Chieh Tan. 2004. "*Theory and Numerical Simulation of Droplet Dynamics in Complex Flows--a Review*." **Lab on a Chip** 4 (4) (August): 257–264. doi:10.1039/b403226h.

Chaiko, D.J. and G.F. Vandegrift, A Thermodynamic Model of Nitric-Acid Extraction by Tri-Normal-Butyl Phosphate. **Nuclear Technology**, 1988. **82**(1): p. 52-59.

R. Codina, G. Houzeaux, H. Coppola-Owen, J. Baiges, *The fixed-mesh ale approach for the numerical approximation of flows in moving domains*, **Journal of Computational Physics** 228 (2009) 1591 – 1611.

V. Cristini, J. Blawzdziewicz, M. Loewenberg, S. Guido, and A. Alfani. *Drop breakup and fragment size distribution in shear flow*. **Journal of Rheology**., 47:1283–1298, 2003.

Danesi, P.R., Chirizia, R., Coleman, C.F., 1980, The Kinetics of Metal Solvent Extraction, C R C Critical Reviews in Analytical Chemistry, Vol. 10, Iss. 1, p. 1-126.

Deshpande, Kiran B., and William B. Zimmerman. 2006. "*Simulations of Mass Transfer Limited Reaction in a Moving Droplet to Study Transport Limited Characteristics*." **Chemical Engineering Science** 61 (19) (October): 6424–6441. doi:10.1016/j.ces.2006.06.013.

Doraiswami LK, Sharma MM. **Heterogeneous Reaction: Analysis, Examples and Reactor Design**, Vol. 2. New York: John Wiley & Sons, Inc., 1984.

Davis, W., J. Mrochek, and R.R. Judkins, *Thermodynamics of the Two-Phase System: Water-Uranyl Nitrate-Tributyl Phosphate-Amsco 125-82*. **Journal of Inorganic & Nuclear Chemistry**, 1970. **32**(5): p. 1689-1702.

T.-P. Fries, A. Zilian, *On time integration in the XFEM*, **International Journal for Numerical Methods in Engineering** 79 (2009) 69–93.

Farbu, L., J. Alstad, and J.H. Augustson. 1974. "*Synergistic Solvent Extraction of Rare-earth Metal Ions with Thenoyltrifluoroacetone Admixed with Tributylphosphate*." **Journal of Inorganic and Nuclear Chemistry** 36 (9) (September): 2091–2095. doi:10.1016/0022-1902(74)80730-X.

Fries, Donata M., and Philipp Rudolf von Rohr. 2009. "*Liquid Mixing in Gas–liquid Two-phase Flow by Meandering Microchannels*." **Chemical Engineering Science** 64 (6) (March 16): 1326–1335. doi:10.1016/j.ces.2008.11.019.

Guido, Stefano, and Valentina Preziosi. 2010. "*Droplet Deformation Under Confined Poiseuille Flow*." **Advances in Colloid and Interface Science** 161 (1–2) (December 15): 89–101. doi:10.1016/j.cis.2010.04.005.

Gunther, Axel, and Klavs F. Jensen. 2006. "*Multiphase Microfluidics: From Flow Characteristics to Chemical and Materials Synthesis*." **Lab on a Chip** 6: 1487. doi:10.1039/b609851g.

Harries, N., J.R. Burns, D.A. Barrow, and C. Ramshaw. 2003. "*A Numerical Model for Segmented Flow in a Microreactor*." **International Journal of Heat and Mass Transfer** 46 (17) (August): 3313–3322. doi:10.1016/S0017-9310(03)00120-0.

Hudson, Steven D. 2009. "*Poiseuille Flow and Drop Circulation in Microchannels*." **Rheologica Acta** 49 (3) (October): 237–243. doi:10.1007/s00397-009-0394-4.

Hudson, Steven D., João T. Cabral, William J. Goodrum, Kathryn L. Beers, and Eric J. Amis. 2005. "*Microfluidic Interfacial Tensiometry*." **Applied Physics Letters** 87: 081905. doi:10.1063/1.2034098.

S., Hysing, *Mixed element FEM level set method for numerical simulation of immiscible fluids*, **Journal of Computational Physics** 231 (2012) 2449 – 2465.

S. Hysing, S. Turek, D. Kuzmin, N. Parolini, E. Burman, S. Ganesan, and L. Tobiskia, *Quantitative benchmark computations of two-dimensional bubble dynamics*, **International Journal for Numerical Methods in Fluids**, 60, 1259-1288, 2009.

F. Ilinca, J.-F. Hétu, *A finite element immersed boundary method for fluid flow around rigid objects*, **International Journal for Numerical Methods in Fluids** 65 (2011A) 856–875.

F. Ilinca, J.-F. Hétu, *Solution of flow around complex-shaped surfaces by an immersed boundary-body conformal enrichment method*, **International Journal for Numerical Methods in Fluids 69** (2011B) 824-841.

Johns, L. E., and R. B. Beckmann. 1966. "*Mechanism of Dispersed-phase Mass Transfer in Viscous, Single-drop Extraction Systems*." **AIChE Journal** 12 (1): 10–16. doi:10.1002/aic.690120105.

CF Jove-Colon, HK Moffat, RR Rao, "*Thermodynamic modeling of liquid-liquid extraction for the system*," **Proceeding of the International High-Level Radioactive Waste Management Conference**, Albuquerque, April, 2011

CF Jove-Colon, HK Moffat, RR Rao, "*Modeling of Liquid-Liquid Extraction (LLE) Equilibria Using Gibbs Energy Minimization (GEM) for the System TBP-HNO_3-UO_2-H_2O-Diluent*," accepted, **Solvent Extraction and Ion Exchange**, July 2012A.

CF Jove-Colon, HK Moffat, RR Rao, "*Thermodynamic Modeling of Liquid-Liquid Extraction (LLE) Equilibria for the System TBP-HNO_3-UO_2-H_2O-Diluent: Applications of the Gibbs Energy Minimization (GEM) Approach to Complex LLE Systems*," SAND2012-9235, Sandia National Laboratories, Albuquerque, NM, October 2012B.

Kadam BD, Joshi JB, Koganti SB, Patil RN. *Dispersed phase hold-up, effective interfacial area and Sauter mean drop diameter in annular centrifugal extractors*. **Chemical Engineering Research and Design**, 2009;87:1379-1389.

M Kostoglou and AJ Karabelas. *On the self-similar solution of fragmentation equation: Numerical evaluation with implications for the inverse problem*. **Journal of Colloid and Interface Science**, 284(2):571–581, 2005.

Kashid, M. N., I. Gerlach, S. Goetz, J. Franzke, J. F. Acker, F. Platte, D. W. Agar, and S. Turek. 2011. "*Internal Circulation Within the Liquid Slugs of a Liquid−Liquid Slug-Flow Capillary Microreactor*." **Ind. Eng. Chem. Res**. 44 (14) (October 6): 5003–5010. doi: 10.1021/ie0490536.

King, Colin, Edmond Walsh, and Ronan Grimes. 2007. "*PIV Measurements of Flow Within Plugs in a Microchannel.*" **Microfluidics and Nanofluidics** 3 (4): 463–472. doi:10.1007/s10404-006-0139-y.

Kronig, R., and J. Brink. 1951. "*On the Theory of Extraction from Falling Droplets*." **Applied Scientific Research** 2 (1): 142–154. doi:10.1007/BF00411978.

Kumemura, Momoko, and Takashi Korenaga. 2006. "**Quantitative Extraction Using Flowing Nano-liter Droplet in Microfluidic System**." **Analytica Chimica Acta** 558 (1–2) (February 3): 75–79. doi:10.1016/j.aca.2005.10.086.

Lee, Sungyon, François Gallaire, and Charles N. Baroud. 2012. "*Interface-induced Recirculation within a Stationary Microfluidic Drop*." **Soft Matter**. doi:10.1039/c2sm26044a..

RA Leonard. *Recent advances in centrifugal contactor design*. **Separation Science and Technology**., 23(12-13):1473–1487, 1988.

Leonard, Ralph A., David G. Wygmans, Michael J. McElwee, Michael O. Wasserman, and George F. Vandegrift. 1993. "*The Centrifugal Contactor as A Concentrator in Solvent Extraction Processes.*" **Separation Science and Technology** 28 (1): 177. doi:10.1080/01496399308019485.

A Lam, AN Sathyagal, S Kumar, and D Ramkrishna. *Maximum stable drop diameter in stirred dispersions*. **AICHE Journal,** 42(6):1547–1552, 1996.

JB Lechman, MB Nemer, DR Noble, "*Application of Conformal-Decomposition Finite Elements to Particle Suspensions*," **International Journal for Numerical Methods in Fluids**, 2012; 68:1409–1421, DOI: 10.1002/fld

Z. Li, T. Lin, X. Wu, *New Cartesian grid methods for interface problems using the finite element formulation*, **Numerische Mathematik** 96 (2003) 61–98. 10.1007/s00211-003-0473-x.

B. Li, J. Shopple, *An interface-fitted finite element level set method with application to solidification and solvation*, **Communications in Computational Physics** 10 (2011) 32–56.

M Loewenberg, RR Rao, "*A simplified model for the evolution of the drop size distribution in an emulsion under strong-flow conditions*," **Proceedings of the 27th Annual Meeting of the PPS,** Morocco, May, 2011

Martinez, M. J., and K. S. Udell. 1990. "*Axisymmetric Creeping Motion of Drops Through Circular Tubes.*" **Journal of Fluid Mechanics** 210: 565–591.

Mary, Pascaline, Vincent Studer, and Patrick Tabeling. 2008. "*Microfluidic Droplet-Based Liquid−Liquid Extraction.*" **Analytical Chemistry** 80 (8) (April 1): 2680–2687.

Di Miceli Raimondi, Nathalie, Laurent Prat, Christophe Gourdon, and Patrick Cognet. 2008. "*Direct Numerical Simulations of Mass Transfer in Square Microchannels for Liquid–liquid Slug Flow*." **Chemical Engineering Science** 63 (22) (November): 5522–5530.

Moffat, H.K. and C.F. Jove Colon, *Implementation of Equilibrium Aqueous Speciation and Solubility (EQ3 type) Calculations into Cantera for Electrolyte Solutions,* **SAND2009-3115,** Sandia National Laboratories, Albuquerque, NM, 2009.

S Mohanty. *Modeling of liquid-liquid extraction column: A review*. **Rev. Chem. Eng**., 16(3):199–248, 2000.
Moyer, B.A., et al., *Liquid-liquid equilibrium analysis in perspective. II. Complete model of water, nitric acid, and uranyl nitrate extraction by di-2-ethylhexyl sulfoxide in dodecane.* **Solvent Extraction and Ion Exchange**, 2001. **19**(5): p. 757-790

R.P. Muller et al., "*Modeling thermal abuse in transportation batteries*," **SAND2012-7816**, Sandia National Laboratories, Albuquerque, NM, September, 2012.

Nadim, Ali, and Howard A. Stone. 1991. "*The Motion of Small Particles and Droplets in Quadratic Flows*." **Studies in Applied Mathematics** 85: 53–73.

Nichols, Kevin P., Rebecca R. Pompano, Liang Li, Artem V. Gelis, and Rustem F. Ismagilov. 2011. "*Toward Mechanistic Understanding of Nuclear Reprocessing Chemistries by Quantifying Lanthanide Solvent Extraction Kinetics via Microfluidics with Constant Interfacial Area and Rapid Mixing."* **Journal of the American Chemical Society** 133 (39): 15721–15729. doi:10.1021/ja206020u.

Nitsch, W. and Van Schoor, A., 1983, The kinetics of coextraction in the system uranylnitrate, nitric acid, tributylphosphate, Chemical Engineering Science, Vo. 38, No. 12, p. 1947-1957.

W. Nitsch and U. Schuster, "*Liquid/Liquid-Mass Transfer at Swarms of Droplets: Kinetics of Mass Transfer in the System Uranyl nitrate, Nitric Acid, Tributylphosphate*," **Separation Science and Technology**, vol. 18, pp. 1509-1533, 1983.

D. R. Noble, E. P. Newren, J. B. Lechman, *A conformal decomposition finite element method for modeling stationary fluid interface problems*, **International Journal for Numerical Methods in Fluids** 63 (2010) 725–742.

P. K. Notz, S. R. Subia, M. M. Hopkins, H. K. Moffat, D. R. Noble, *ARIA Manual Aria 1.5: User's Manual*, **SAND2007-2734**, Sandia National Laboratories, Albuquerque, NM, April, 2007.

M. Pilch and C.A. Erdman. *Use of breakup time data and velocity history data to predict the maximum size of stable fragments for acceleration-induced breakup of a liquid drop*. **International Journal Multiphase Flow**, 13:741–757, 1978.

N. B. Raikar, S. R. Bhatia, M. F. Malone, and M. A. Henson. *Self-similar inverse population balance modeling for turbulently prepared batch emulsions: Sensitivity to measurement errors.* **Chemical Engineering Science**., 61:7421–7435, 2006.

N. B. Raikar, S. R. Bhatia, M. F. Malone, D.J. McClements, C. Almeida-Rivera, P. Bongers, and M. A. Henson. *Prediction of emulsion drop size distributions with population balance equation models of multiple drop breakage*. **Colloids Surfaces A: Physicochemical & Eng**., 361:96–108, 2010.

U. Rasthofer, F. Henke, W.A. Wall, V. Gravemeier, *An extended residual-based variational multiscale method for two-phase flow including surface tension*, **Computer Methods in Applied Mechanics and Engineering,** Volume 200, Issues 21–22, Pages 1866-1876, 1 May 2011.

Roberts, Christine C., Rekha R. Rao, Michael Loewenberg, Carlton F. Brooks, Paul Galambos, Anne M. Grillet, and Martin B. Nemer, *Comparison of Monodisperse Droplet Generation in Flow-focusing Devices with Hydrophilic and Hydrophobic Surfaces*. **Lab on a Chip** 12 (8) (April 21): 1540–1547, 2012A.

CC Roberts, AM Grillet, MB Nemer, "*A flow-focusing device for mass transport studies of rare earth complexes with applications to contactors*," **Chemical Engineering Science**, in preparation, 2012B

CC Roberts, SA Roberts, "*Understanding internal flows for confined droplets: Experiments and modeling*," **Physics of Fluids**, in preparation, 2012C

P. A. Sackinger, P. R. Schunk, R. R. Rao, *A Newton-Raphson pseudo-solid domain mapping technique for free and moving boundary problems: A finite element implementation*, **Journal of Computational Physics** 125 (1996) 83 – 103.

Sarrazin, Flavie, Thomas Bonometti, Laurent Prat, Christophe Gourdon, and Jacques Magnaudet. 2008. "*Hydrodynamic Structures of Droplets Engineered in Rectangular Micro-channels.*" **Microfluidics and Nanofluidics** 5 (1): 131–137. doi:10.1007/s10404-007-0233-9.

AN Sathyagal, D Ramkrishna, and G Narsimhan. *Solution of inverse problems in population balances 2. particle break-up*. **Computers & Chemical Engineering**., 19(4):437–451, 1995.

H. Sauerland, T.-P. Fries, *The extended finite element method for two-phase and free-surface flows: A systematic study***, Journal of Computational Physics** 230 (2011) 3369 – 3390.

Schwalbe, Jonathan T., Frederick R. Phelan, Jr., Petia M. Vlahovska, and Steven D. Hudson. 2011. "*Interfacial Effects on Droplet Dynamics in Poiseuille Flow*." **Soft Matter** 7 (17): 7797. doi:10.1039/c1sm05144j.

Schuur B, Gerard KN, Winkelman JGM, Heeres HJ. *Hydrodynamic features of centrifugal contactor separators: Experimental studies on liquid hold-up, residence time distribution, phase behavior and drop size distributions.* ***Chemical Engineering and Processing: Process Intensification,*** 2012;55:8-19.

Siegel AF, Sugihara G. *Moments of particle size distributions under sequential breakage with applications to species abundance*. **Journal of Applied Probability**, 1983;20:158-164.

A. Smolianski, *Finite-element/level-set/operator-splitting (FELSOS) approach for computing two-fluid unsteady flows with free moving interfaces,* **International Journal for Numerical Methods in Fluids** 48 (2005) 231–269.

Suyitno, S. Fujine, H. Fumoto, M. Maeda, and A. Suzuki, *"Evaluation of Mass Transfer Coefficient By Single Droplet Experiment In A Water-Uranyl Nitrake-TBP Diluted In Normal Dodecane System*," Fuel Reprecessing Laboratory, Department of Fuels and Materials Research, Japan Atomic Energy Research Institute ToJ.:ai-Mura, Naka-Gun, Ibarakiken, Japan., pp. 28-42.

Tamhane TV, Joshi JB, Mudali K, Natarajan R, Patil RN. *Measurement of drop size characteristics in annular centrifugal extractors using phase Doppler particle analyzer (PDPA).* **Chemical Engineering Research and Design**, (2011).

Teh, Shia-Yen, Robert Lin, Lung-Hsin Hung, and Abraham P. Lee. 2008. "*Droplet Microfluidics*." **Lab on a Chip** 8 (2): 198. doi:10.1039/b715524g.

N. Vankova, S. Tcholakova, N. D. Denkov, V. D. Vulchev, and T. Danner. *Emulsification in turbulent flow 2. Breakage rate constants***, Journal of Colloid and Interface Science**., 313(2):612–629, 2007.

Vedantam, S., K. E. Wardle, T. V. Tamhane, V. V. Ranade, and J. B. Joshi. 2012. "*CFD Simulation of Annular Centrifugal Extractor*s." **International Journal of Chemical Engineering** 2012: 1–31. doi:10.1155/2012/759397.

Wang, C. Y, and R. V Calabrese. 1986. "*Drop Breakup in Turbulent Stirred-tank Contactors. Part II: Relative Influence of Viscosity and Interfacial Tension*." **AIChE Journal** 32 (4) (April 1): 667–676. doi:10.1002/aic.690320417.

Wang, Yechun, and Panagiotis Dimitrakopoulos. 2011. "*Low-Reynolds-number Droplet Motion in a Square Microfluidic Channel*." **Theoretical and Computational Fluid Dynamics** 26 (1-4) (July 22): 361–379. doi:10.1007/s00162-011-0238-6.

K. E. Wardle, T. R. Allen, and R. Swaney. *Computational fluid dynamics (CFD) study of the flow in an annular centrifugal contactor*. **Separation Science and Technology**, 41(10):2225–2244, 2006.

Wardle, Kent E., and Taehun Lee. "*Finite Element Lattice Boltzmann Simulations of Free Surface Flow in a Concentric Cylinder*." **Computers & Mathematics with Applications** (0). doi:10.1016/j.camwa.2011.09.020.

White, Frank. 1991. **Viscous Fluid Flow**. New York, NY: McGraw-Hill.

Xu, J.H., J. Tan, S.W. Li, and G.S. Luo. 2008. "*Enhancement of Mass Transfer Performance of Liquid-Liquid System by Droplet Flow in Microchannels.*" **Chemical Engineering Journal** 141 (1-3) (July 15): 242–249. doi:10.1016/j.cej.2007.12.030.

12 DISTRIBUTION

Dr. Marianne M. Francois (electronic copy)
Computational Physics and Methods Group, CCS-2
Los Alamos National Laboratory
PO Box 1663, MS B296
Los Alamos, NM87545, USA

Michael Loewenberg (electronic copy)
Chemical Engineering Department
Yale University
New Haven, CT 06520-8286

Kent E. Wardle (electronic copy)
Chemical Sciences and Engineering Division
Argonne National Laboratory
9700 S. Cass Ave.
Argonne, IL 60439

1	MS0346	Anne Grillet	1512 (electronic copy)
1	MS0346	Lindsey Hughes	1512 (electronic copy)
1	MS0346	Lisa Mondy	1512 (electronic copy)
1	MS0346	Christine Roberts	1512 (electronic copy)
1	MS0346	Bion Shelden	1512 (electronic copy)
1	MS0346	Nick Wyatt	1512 (electronic copy)
1	MS0380	Kim Mish	1542 (electronic copy)
1	MS0747	Veena Tikare	6223 (electronic copy)
1	MS0779	Carlos Jove-Colon	6222 (electronic copy)
1	MS0782	Chris Brotherton	6633 (electronic copy)
1	MS0828	Steve Kempka	1510 (electronic copy)
1	MS0828	Ryan Bond	1541 (electronic copy)
1	MS0836	Stefan Domino	1541 (electronic copy)
1	MS0836	Chris Bourdon	1512 (electronic copy)
1	MS0836	Jon Clausen	1514 (electronic copy)
1	MS0836	David Noble	1514 (electronic copy)
1	MS0836	Rekha Rao	1514 (electronic copy)
1	MS0836	Scott Roberts	1514 (electronic copy)
1	MS0836	Marty Pilch	1514 (electronic copy)
1	MS0836	Jeremy Lechman	1516 (electronic copy)
1	MS0836	P. Randall Schunk	1516 (electronic copy)
1	MS0840	Timothy O'Hern	1512 (electronic copy)
1	MS1318	Roger Pawlowski	1444 (electronic copy)
1	MS9409	Lindsay Erickson	8365 (electronic copy)
1	MS9409	Greg Wagner	8365 (electronic copy)
1	MS0899	Technical Library	9536 (electronic copy)
1	MS0359	D. Chavez, LDRD Office	1911 (electronic copy)


Sandia National Laboratories